DISS. ETH No. 18352

Methods and Techniques in Composite Design for Structural Vibration Suppression via Shunted Piezoelectric Elements

A dissertation submitted to
ETH ZURICH

for the degree of
Doctor of Sciences

presented by
Alberto Belloli
Dipl. Masch.-Ing. ETH
born November 29, 1976
citizen of Isorno (TI)

accepted on recommendation of
Prof. Dr. Paolo Ermanni, examiner
Prof. Dr. h.c. Urs Meier, co-examiner
Prof. Dr. Manfred Morari, co-examiner

2009

"To my Grandfathers Riccardo and Alberto,
who taught me by their example to stand up for what I believe in."

Acknowledgements

Accomplished at the Centre of Structures Technologies at ETH Zurich, the present thesis is just one among many results of Empa's research programm *Adaptive Werkstoffe* and one of two doctoral thesis resulting from the project *PiezoDamp*, a cooperation between Empa, the Automatic Control Laboratory, and the Centre of Structure Technologies, both at ETH Zurich.

Special thanks go to Prof. Dr. Paolo Ermanni, for offering me a fascinating PhD project, absolute freedom in my work and many tasks that forged my personality, both as a scientist and as a man. I'm equally much obliged to Prof. Dr. h.c. Urs Meier and Prof. Dr. Manfred Morari, for supporting this thesis as co-examiners, providing valuable advice and feedbacks, and opening access to many facilities and pieces of equipment.

Any of the results described in this thesis would have been hardly achieved without the great support by Dr. Dominik Niederberger for any question related to electronics and vibration control, the amazing competence in organic chemistry of Dr. Stephan Busato, the knowledge about piezoelectric ceramics of Dr. Juliane Heiber, the friendly support with fiber reinforced polymers provided by Dr. Niccolò Pini, the help with optics by Dr. Nicolas Goudemand, the competent supervision on evolutionary algorithms by Dr. Oliver Koenig, Dr. Nino Zehnder and Dr. Mathias Giger, as well as the cooperation with Dr. Mark Melnykowycz, Dr. Frank Clemens, Dr. Rolf Paradies, Dr. Michel Barbezat, Dr. Xavier Kornmann and Dr. Stanislaw Pietrzko at Empa Duebendorf.

Dr. Gerald Kress was the right address for any question related to optimization and structural mechanics, and a receptive listener whenever needed by a confused PhD student. Gion Barandun solved almost any IT-related problem I could possibly produce.

Tobias Lambrecht, Benedetto Castelli, Oliver Thomaschewski, Roger Zehnder, Alain Monnin and Silvio Hochreutener spent endless hours in the lab and debugging FE-codes together with the author. Their contribution to the thesis within their master and diploma theses and term projects is herein gratefully acknowledged.

The investigations on the test object were made possible by my dear friend Sébastien Mathis, Christoph Zimmermann, Thomas Knodel, Tim Camp and Willi Rampf, who gave me material and technical support.

An equally important support was assured on a daily basis by Helen Goetz, Freddy Bürki, Gerhard Kuhn and Hans-Peter Eigenmann, our guardian angels in the office and the lab.

In 2004 I had the opportunity to be a visiting scholar at DLR Braunschweig. This experience broadened up my scientific horizon and gave me additional motivation for the completion of my thesis. My gratitude therefor goes to Dr. Lucio Flavio Campanile and Prof. Dr. Elmar Breitbach.

This PhD project brought together researchers and engineers from various scientific and engineering disciplines, and encouraged the transfer of advanced scientific results from research to new and innovative applications. That’s why I thankfully look back and say: "I would do it again (maybe a bit faster)!"

Alberto Belloli

Abstract

The structural vibration suppression via shunted piezoelectric elements is studied in this work, covering the whole range from the single smart component to the finished prototype smart system.

Part I is devoted to piezoelectric ceramic fibers, the core component of Active Fiber Composites. A novel characterization procedure for the ferroelectric characterization of single piezoelectric fibers yielded butterfly and hysteresis loops and force-displacement curves for three different commercially available fibers and fibers under development at Empa Duebendorf. The observed response was correlated to the respective microstructural properties and fibers were identified for manufacturing AFC later embedded into the test object.

In Part II the micromechanical properties of so-called Active Fiber Composites were investigated both numerically and experimentally. Configurations were optimized in terms of free-strain, force and capacitance response, respectively. Even so, only marginal improvements could be achieved with respect to the requirements imposed to active components for use in structural vibration control.

Part III presents efforts towards proper integration of sensors and actuators into load-carrying composite structures. A laboratory method provides for prototyping large area circuitry with moderate resolution on electrically and thermally stable polyimide. While encapsulation of piezoelectric ce-

ramic wafers allowed for larger modules, perfect insulation and ease of handling, numerical and extensive experimental investigations quantified the impact of their inclusion onto GFRP and CFRP laminate strength.

Part IV focuses on the ultimate goal: the suppression of structural vibration. The performance of Active Fibre Composites and traditional piezoelectric ceramic elements in suppressing structural vibration was compared both experimentally and numerically. Traditional monolithic actuators offer best performance and turned out to be better suited for shunt damping, due to their larger inherent capacitance. AFC, due to their larger voltage output and anisotropic response, seem to be predestined for use as sensing elements. Both monolithic actuators and AFC sensors were successfully placed for optimum vibration suppression using *R-L* and switching *R-L* shunts. The optimization approach includes a CAD-model, an FE-model and evolutionary algorithms and proved a valuable tool in finding optimum solutions for real-world, highly constrained structures.

A rear wing of a racing car was selected as test object for verification of all methods and techniques previously introduced. Experimental validation proved the technology to be effective in suppressing structural vibration, with the trailing edge's flutter mode on the endplates being reduced by 12.5dB (or 76%).

Zusammenfassung

Diese Arbeit untersuchte die Schwingungsdämpfung lasttragender Strukturen mittels piezoelektrischen Elementen und passiven elektrischen Netzwerken. Sie befasste sich mit Problemstellungen, welche von der einzelnen aktiven Materialkomponente bis hin zum fertigen intelligenten Prototypensystem reichen.

Teil I ist den piezoelektrischen keramischen Fasern gewidmet, der wichtigsten Komponente von sogenannten Active Fiber Composites (AFC). Eine neu entwickelte Prozedur erlaubte die ferroelektrische Charakterisierung von einzelnen piezoelektrischen Fasern. Schmetterlings- und Hysteresekurven sowie Kraft-Weg-Diagramme konnten für drei verschiedene, kommerziell verfügbare Fasern sowie für Fasern ermittelt werden, welche zurzeit an der Empa Dübendorf weiterentwickelt werden. Eine enge Korrelation zwischen der gemessenen ferroelektrischen Antwort und der jeweiligen Mikrostruktur ist erkennbar. Die Studie identifizierte die Faser zur Herstellung von AFC, welche später in das Testobjekt integriert wurden.

Teil II beschreibt die numerische und experimentelle Untersuchung der mikromechanischen Eigenschaften von Active Fiber Composites. Es wurden optimale Konfigurationen für die maximale freie Dehnung, die maximale Kraft beziehungsweise die maximale elektrische Kapazität ermittelt. Die erreichten Verbesserungen sind hinsichtlich des Einsatzes von AFC zur Schwingungsunterdrückung leider nur marginal.

Teil III vertieft ausgewählte Aspekte zur korrekten Einbettung von Sensoren und Aktoren in lasttragenden Strukturen. Eine neue Methode ermöglicht die labormässige Herstellung von grossflächigen leitfähigen Kupferbahnen auf Polyimid-Folien, einem elektrisch und thermisch stabilen Polymermaterial. Dank der darauffolgenden Einkapselung von piezoelektrischen keramischen Platten konnten grössere Module mit perfekter elektrischer Isolierung und vereinfachtem Handling hergestellt werden. Numerische und umfangreiche experimentelle Untersuchungen quantifizierten den Einfluss der Einbettung auf die Festigkeit von glasfaser- und kohlenstoffaserverstärkten Laminaten.

Teil IV fokussiert auf die Schwingungsdämpfung lasttragender Strukturen - das Gesamtziel der vorliegenden Arbeit. Die Schwingungsdämpfung mittels Active Fibre Composites und herkömmlichen piezoelektrischen keramischen Modulen wurde sowohl numerisch als auch experimentell untersucht. Aufgrund der höheren inhärenten Kapazität sind monolithische Aktoren besser für den Einsatz mit passiven elektrischen Netzwerken geeignet. AFC hingegen, sollten Dank der höheren generierten Spannung und der anisotropen Antwort Einsatz als Sensoren finden. Sowohl monolithische Aktoren als auch AFC Sensoren wurden so platziert, dass eine optimale Schwingungsdämpfung mittels *R-L* und schaltbaren *R-L* Netzwerken erreicht werden konnte. Die Optimierungsprozedur besteht aus einem CAD-Modell, einem FE-Modell und evolutionären Algorithmen. Damit konnten optimale Lösungen für reellen, komplexen Strukturen gefunden werden.

Der Heckflügel eines Rennautos diente als Testobjekt zur Verifizierung aller entwickelten Methoden und Techniken. Die experimentelle Validierung bestätigte, dass die angewandten Technologien effektiv zu einer Schwingungsdämpfung führen. Ein Schwingungsmode der Endplatten konnte um 12.5dB (oder 76%) reduziert werden.

Contents

Chapter 1

Introduction

In the 20th century, advanced research in materials science resulted in man-made structural materials such as composites. On the other hand, materials with amazing properties were discovered. These achievements have allowed embedding sensors and actuators into the load-carrying structure, thus opening up the design space to such an extent, that engineers started talking about structures that can monitor themselves and adapt to the environment.

Smart materials and structures have therefore long been heralded as the dawn of a new era in the automotive, transportation and aerospace industries, with engineers and managers planning to integrate them in products that have to meet ever more demanding performance requirements. This has largely not happened, at least not in the commercial arena. Among the many reasons for this are the prohibitive costs, the additional complexity and weight, and concerns about availability and robustness of the system. On the other hand, the intense activity and interaction among physicists, material scientists, control engineers, and structural engineers may be just one more indication of the potential represented by smart materials and structures. The current research efforts are best represented by four broad directions.

1.1 Materials

Smart materials have the capability of significantly change one or more properties upon external stimulus. Piezoelectric materials, e. g., show a charge separation when strained, and strain when an electric voltage is applied [1]. Electro- and magnetostrictive materials [2, 3] behave in a similar way. Shape memory alloys (SMA) [4, 5] are metals, which exhibit pseudo-elasticity (an almost rubber-like flexibility) and the shape memory effect (the ability to be severely deformed and then return to their original shape simply by heating). Electro-rheological (ER) [6] and magneto-rheological (MR) materials [7] are fluids, which can experience a dramatic change in their viscosity (from thick fluid to nearly solid) when exposed to a magnetic or electric field. Electroactive polymers (EAP) [8] can be used as actuators or sensors. As actuators, they are characterized by the fact that they can undergo a large amount of deformation while sustaining large forces. Ongoing research aims at improving smart materials in terms of performance, environmental impact and durability. Several researchers are looking for lead-free piezoelectric materials [9]; others work on SMA to increase their bandwidth [10]; and other institutions put significant effort into improving the long-term behavior of EAP [11].

1.2 Structures, Systems and Solutions

The amazing properties of smart materials are useless if not properly packaged in smart components, structures and systems. In the past, piezoelectric materials were most widely used as sensors in different environments. Significant efforts are being undertaken to develop sensors and actuators showing orthotropic response [12], and efficient actuators allowing larger displacements [13]. EAP are being manufactured in shell-like active elements, capable of smooth out-of-plane displacements [14]. Beam elements including ER fluid layers are regarded as a promising approach for the vibration damping of bridges and buildings [15], just as MR fluids are the core component of active dampers for cable-stayed bridges [16, 17]. In an attempt of manufacturing affordable, light-weight smart composite parts,

thin SMA layers are being sprayed on the load carrying structure [18, 19].

1.3 Tools and Methodologies

The assessment of the potential of new technologies implies a proper understanding of both the behavior of smart systems and of their components. Multi-field simulation gives more and more insight into physical aspects of smart components and predicts the response of complex systems. If coupled with an optimization engine, such simulation models often allow for better solutions that are beyond the engineer's intuition. Measuring instrumentation that senses and actuates at the micromechanical level is needed for validating numerical results. New manufacturing processes under development will allow tailoring structural components form the micro to macro levels. Embedding technologies are developed for the structural integration of sensors and actuators. Different control strategies are being tested that minimize energy consumption while enhancing system stability [20, 21]. Finding optimum locations for sensors and actuators is - finally - a key task, be it for vibration suppression, morphing or structural health monitoring.

1.4 Applications

Major current activities can be categorized in vibration control and noise abatement [22], morphing [23, 24, 25] and position control [26], and structural health monitoring [27]. Potential applications can be found in the aerospace, automotive, and transportation industries. Prototype applications can be found among manufacturing systems, medical devices [28, 29] and measuring systems. Piezoelectric materials are regarded as a promising approach to control vibration in elevons of fighter aircrafts at flutter [30], or in helicopter rotors at critical speeds [31]. They could further find application as positioning and vibration control devices in atomic force microscopes [32], in power harvesting devices or as aircraft sensors that warn of impending cracks [33]. MR fluids are being developed for use

in car shocks [34], damping washing machine vibration [35], prosthetic limbs, hydraulic displacement machines [36], exercise equipment [37], and surface polishing of machine parts [38]. ER fluids have mainly been developed for use in clutches and valves [39], as well as engine mounts [40] designed to reduce noise and vibration in vehicles. Due to the similarities with biological tissues in terms of achievable stress and force, EAP are often called artificial muscles [41], and have the potential for application in the field of robotics, where large linear movement is often needed.

As shown by this short overview of the state of research, the design of smart structures is on the cutting edge of engineering research and development. The reason for the yet missing breakthrough of the highly multidisciplinary field of smart materials and structures might then be that we do not understand how to properly integrate structure and control system design.

As a contribution to the development of comprehensive methodologies for the integration of smart systems, this thesis focuses on the *Vibration Control of Load-carrying Composite Structures via Shunted Embedded Piezoelectric Ceramic Elements*. Above description expresses the highly multidisciplinary character of the work, which encompasses aspects of mechanical engineering, dynamics, composite technology, control engineering and material science.

Relevance of vibration control

Dynamic behavior is one main design criterion for many kinds of load-carrying structures, as undesirable large-amplitude vibrations often impede the effective operation of various types of mechanical systems, including antennae, spacecrafts, rotorcrafts, automobiles, and sophisticated instruments. It is therefore desirable to introduce structural damping into a system to achieve a more satisfactory response and to delay fatigue damages [42]. Composites with piezoelectric sensors and actuators offer great potential for use in the field of active structural acoustic and vibration control as well as shape control and health monitoring.

1.5 Goals and Approach

Figure 1.1 illustrates our understanding of a general smart structure. This articulates in four levels. New materials with astonishing properties are discovered or synthesized in material science laboratories. Researchers and engineers combine a smart material component (mostly useless if taken alone) with a number of passive components to what we call a smart device. To fulfill its task, this has typically to be integrated into a passive host structure and controlled by a dedicated algorithm. The resulting active structural part can be assembled with one or more passive structural parts to a complex smart system.

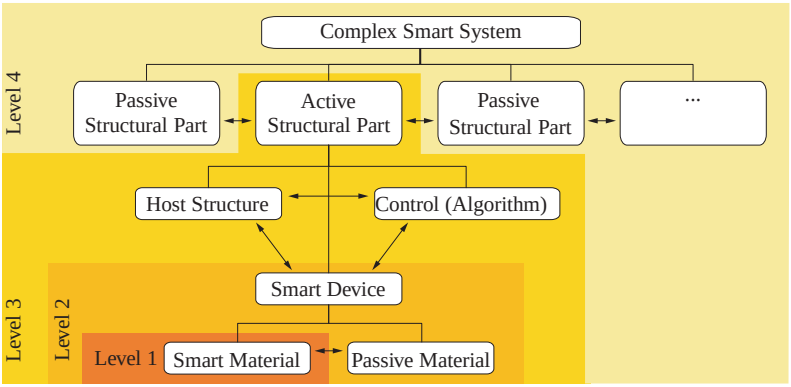

Figure 1.1: Schematic of a generic smart structure; Degrees of integration. The arrowheads symbolize interfaces and interactions between components.

Level 1 is, by nature, the realm of material scientists. Mechanical engineers design devices at Level 2 and, joining forces with control engineers, integrate them into active parts at Level 3. System engineers, finally, forge final products at Level 4.

Bolstered by the highly multidisciplinary team at Empa, by the col-

leagues of the Automatic Control Laboratory and by the manifold competence we found at the Centre of Structural Technologies; driven by curiosity, young ambition, and by some degree of unconsciousness; while defining the scope of the present work, we decided to tackle at least one aspect for every single level identified above. The research goals cover the whole range from the single components to the finished prototype system. The resulting Work Packages are depicted in Figure 1.2.

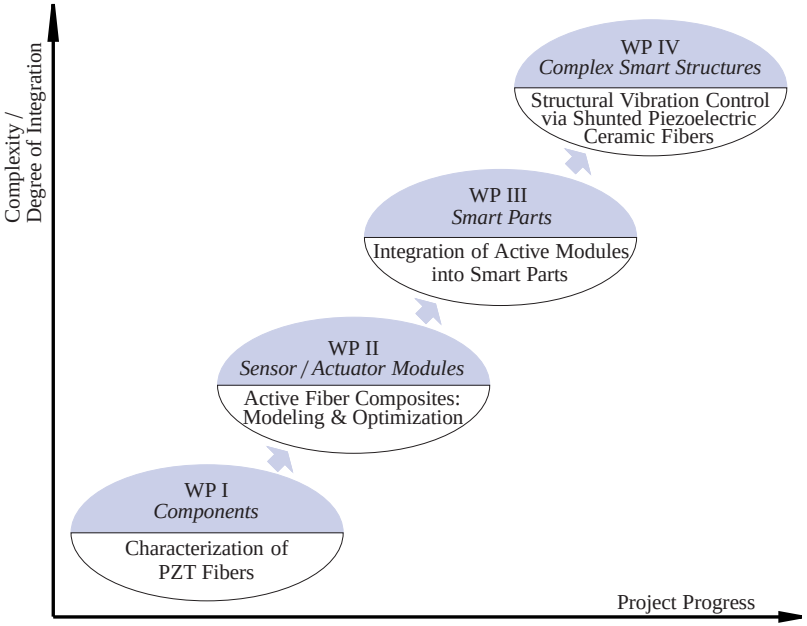

Figure 1.2: Increasing complexity and degree of integration in the research approach. Work Packages defined for the present thesis.

Work Package I will be devoted to piezoelectric ceramic fibers, the core component of Active Fiber Composites. An extrusion route for the production of PTZ-based piezoelectric ceramic fibers being currently developed

at Empa Duebendorf, this is a unique opportunity for customizing fiber properties and processing to the needs of the vibration control application. Commercially available fibers will be included in the investigations.

Distinct applications call for different characteristics of piezoelectric ceramic modules. *Work Package II* will investigate Active Fiber Composites, identify their actuating variables and disclose the optimization potential for different target entities.

The best sensor or actuator will show poor performance if not properly integrated in the load-carrying structure. This is why *Work Package III* will make contributions on enhancing the prototyping of electrical connections to the active material and on minimizing the impact of inclusions on laminate strength and on the structural behavior.

Work Package IV will consider application of methods and technologies developed in the previous work packages. Whenever necessary, missing elements will be developed in cooperation with other research groups. The validation phase will go beyond typically used demonstrators such as cantilever beams and plates. We will select a test object with higher complexity in term of geometry, boundary conditions and structural requirements. New control strategies, developed in the scope of the PhD thesis "Smart Damping Materials using Shunt Control" [20], will be considered and integrated at this stage.

The state of research and the resulting research needs for the single aspects investigated will be presented in the respective chapters.

Part I

Characterization of Piezoelectric Ceramic Fibers

Chapter 2

Novel Characterization Procedure for Single Piezoelectric Fibers

The work presented in this Chapter can be found with minor modifications as a publication in the scientific literature as:

A. Belloli, J. Heiber, F. Clemens and P. Ermanni. Novel Characterization Procedure for Single Piezoelectric Fibers. *Journal of Intelligent Material Systems and Structures*, 20(3):355-363, 2009.

The characterization of the ferroelectric properties of piezoelectric ceramic fibers is paramount for optimizing their manufacturing processes, for quality control purposes, and for modeling the response of components and structures. Until now, fibers were generally characterized by measuring so-called 1-3 composites, fiber arrays embedded in a polymer matrix. The fiber properties can then be extracted provided the volume

fraction and stiffness of each phase, the fiber piezoelectric charge constant as a function of the electrical field strength, and the matrix permittivity are known. This implies a large amount of time and experimental effort. This article presents a comprehensive procedure for the direct characterization of single piezoelectric ceramic fibers in terms of butterfly and polarization loops, as well as their blocking force. The experimental setup is composed of a wave form generator, a high-voltage amplifier, a dynamic mechanical analyzer, a current/charge measuring circuit, and an oscilloscope. The active circuitry used for reliably collecting the charge generated by a single fiber is presented in full detail. The very good repeatability of the measurements showed the proposed procedure to be robust. The comparison between single fiber measurements and the investigation of 1-3 composites revealed both procedures to be equal, at 99.9%, in determining the average strain and polarization properties. In addition, the single fiber measurement provides an estimation of the variation in fiber properties within a single production batch. This information is essential to understand how to optimize processing routes and build robust devices.

2.1 Introduction

In the past decade, the scientific community has put significant effort into developing piezoelectric ceramic fibers for orthotropic sensing and actuation. Several processes were developed to produce PZT fibers in a certain diameter range, e.g., the viscous suspension spinning process VSSP [43], the ALCERU method [44] and the extrusion route [45].

Piezoelectric fibers show high potential as components in ultrasonic transducers for higher resolution medical imaging [28, 29], sonar technology for naval applications [46], structural health monitoring systems [27], active twist control [47], reduction of acoustic radiation [48], and vibration suppression [49, 50]. The characterization of their physical, mechanical and piezoelectric properties is paramount for optimizing the manufacturing processes, for quality control purposes, and for modeling the response of components and structures.

2.1.1 Polarization Properties

The commonly accepted criterion of ferroelectricity is a hysteresis loop on a $D - E$ display [1]. The usual method consists of applying an alternating voltage to the material sample and relating the stored charge to the instantaneous voltage using a so-called Sawyer-Tower circuit [51], a large integrating capacitor placed in series with the sample. The voltage across it corresponds to the charge stored. Meyer et al. [29] used a modified Sawyer-Tower circuit to determine the remanent polarization and the coercive field of 1-3 composites, a multitude of uniaxially oriented fibers embedded in a polymer matrix. Nelson et al. [52, 53] measured the polarization response of 1-3 composites by using a device developed at the National Physical Laboratory [54]. In addition to contributions developed by the fibers and the matrix, the composite response also comprises a contribution from active fiber clamping by the polymer matrix. The polarization response of the fibers can then be extracted from the 1-3 composite response, provided that the volume fraction and stiffness of each phase, the fiber piezoelectric charge constant as a function of the electrical field strength and the matrix permittivity are known [46]. This implies a large amount of time and experimental effort.

Due to at least three reasons, the simple circuit proposed by Sawyer and Tower fails to reliably deliver precise hysteresis loops for single piezoelectric ceramic fibers. Firstly, the capacitance of such a fiber 3mm in length is in the order of 300 fF. Secondly, the input impedance of the oscilloscope (typically $1M\Omega$) is not large enough to keep a significant part of the charge stored on the sample (respectively on the integrating capacitor) from flowing to ground through the instrument. Finally, the voltage applied to the fiber can be as large as 10kV. In the case of a (not too unlikely) breakdown, such a voltage would possibly lead to major oscilloscope damage.

Due to similar reasons, a number of researchers proposed active circuitry solutions for determining the polarization behavior of polymers, ceramics, or composites. Dickens and co-workers [55] presented a method for estimating the remanent polarization, coercive field, dielectric constant and linear resistance of polymers with ideal capacitive and resistive behavior to a sinusoidally varying applied voltage. Additionally, an experimental

technique is introduced which allows the determination of the remanent polarization in the presence of non-ideal capacitive and conductive material behavior. Dias and Das-Gupta [56] published a similar way to measure the polarization of ferroelectric composites having 0-3 connectivity with non-ideal capacitive and/or conductive behavior. Their method is based on the simultaneous measurement of the current of a sample to which a bipolar voltage is applied, and that of two other reference samples to which a unipolar field is applied, thus generating resistive and capacitive current components only. These are then subtracted from the current flowing through the investigated sample, yielding its switching current.

The charge generated by a single piezoelectric ceramic fiber could be reliably collected by Yoshikawa et al. [57] by means of a non-specified active circuitry which replaced the passive capacitor. For the first time, the ferroelectric nature of a single piezoelectric fiber could be demonstrated. The same circuit was later used by Bystricky [58] for quality control of extruded PZT fibers.

2.1.2 Strain Properties

The piezoelectric strain constants of 1-3 composites were investigated by Steinhausen et al. [28] using a microdisplacement meter with a capacitive detector [59]. Due to issues related to the composite manufacturing, however, only composites up to a fiber volume fraction of 25% could be successfully characterized. Meyer et al. [29] obtained the displacement of 1-3 composites using a Linear Variable Differential Transformer (LVDT). Clamping of the fibers by the polymer matrix was observed for the composites with fiber volume fractions between 10% and 45%. Displacement clamping by the LVDT measuring probe and varying displacement values across the composite surface were also reported. Nelson et al. [60] used impedance analysis to determine the longitudinal coupling factor, the longitudinal induced strain constant, as well as the short circuit and open circuit longitudinal compliances for 1-3 composites. The authors then extracted fiber properties by applying equations proposed by Smith [46]. The fiber piezoelectric strain can be evaluated, provided the compliance and volume fraction of each composite phase are known. The authors later ex-

tended their investigation to the high-field behavior of the same 1-3 composites [52]. In their studies, the sample displacement was monitored using a capacitance sensor, linked to the sample via a leaf spring [54]. As pointed out by Nelson et al. [60], frequency dependence of the polymer matrix mechanical properties and the strength of the fiber matrix interface may cause extracted fiber properties to differ from their true values. The assumption that the composite behaves as a homogeneous medium - with the strain in the fiber and matrix being identical in the longitudinal direction - was shown to hold for composites with a volume fraction exceeding 10% [52]. Bent [61] was the first to measure the free-strain properties of single fibers (both sliced from monolithic PZT wafers and produced via the extrusion route) using a planar displacement measuring device including a laser interferometry system. Teflon surfaces minimized the frictional forces to be overcome by the activated fiber. His results show a large variation in actuation strain and coercive fields, thus confirming the usefulness of single fiber testing.

When using piezoelectric fibers as components of actuator modules, one is interested in knowing the work which can be carried out by a single piezoelectric fiber. To the knowledge of the authors, no successful measurement of the single fiber's blocking force has been reported in literature.

One could argue that only the average fiber performance is relevant for use in models. On the other hand, variation in fiber properties is just as important to understand how to optimize processing routes and build robust devices. Single fiber testing can provide information on standard deviation with a minimum amount of material, within a production batch or even a single fiber.

In the view of the limitations described above for the measurement of 1-3 composites, the author and his co-workers proposed a comprehensive procedure for the ferroelectric characterization of single piezoelectric ceramic fibers. After describing the experimental setup, the procedures for measuring hysteresis and butterfly loops are specified. The latter is then extended to determine the blocking force of single piezoelectric ceramic fibers. The proposed procedures were validated by comparing single fiber measurements with results from 1-3 composites prepared with a multitude of fibers from the respective batches.

2.2 Materials and Methods

For characterization of their ferroelectric properties, single PZT fibers from Smart Material, Corp. 250μm in diameter were cut into 3.5mm long pieces and placed vertically into a PMMA sample holder (Figure 2.1). The sample geometry was modeled and optimized using the Finite Element Method for the electrical field distribution in the single fiber to be as uniform as possible. Both fiber ends were coated with silver epoxy (Electrodag 5915, Acheson Colloids Company) to apply electrical contact. The active free length of the fibers was thereby shortened to about 2.5mm. The fibers were immersed in silicon oil to avoid an electrical breakdown. Poling was achieved by applying electrical fields of 35kV/cm for 5 min at room temperature.

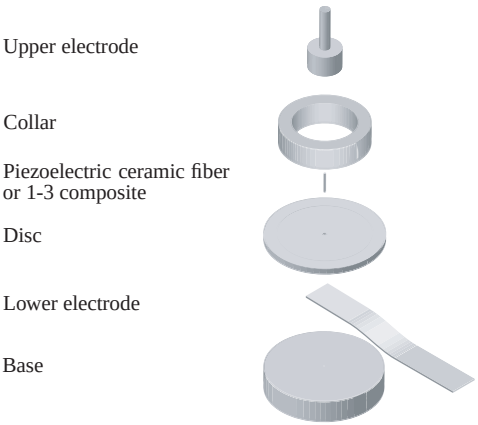

Figure 2.1: Exploded view of the sample holder.

The 1-3 composites (fiber volume fraction exceeding 60%) were prepared by incorporating a multitude of fibers from the same batch in cylindrical molds 2.0mm in diameter and infiltrating with a degassed low viscosity epoxy two-component resin system (Araldit BY 158 resin and Aradur

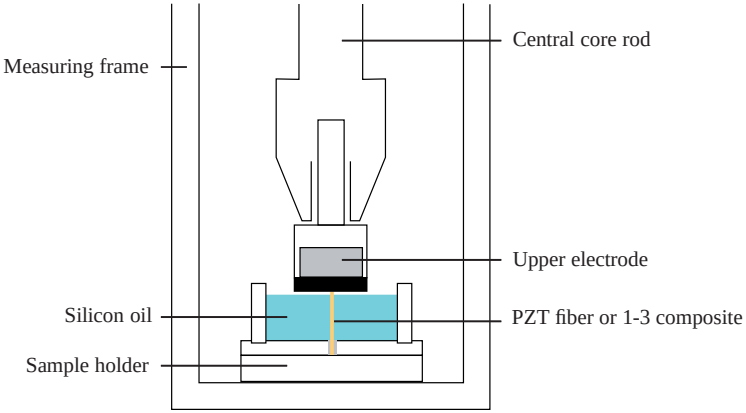

Figure 2.2: Detail view of the sample holder and the measuring head of the Dynamic Mechanical Analyzer.

21 hardener). The composites were cured for 24h at room temperature and cut to 4mm length. Conductive silver epoxy resin was then applied on their polished end faces. The sample holder depicted in Figure 2.2 was adapted in order to accommodate the 1-3 composites, now approximately 2.5mm in length. Again, poling was achieved by applying an electrical field of 35kV/cm at room temperature for 5 min.

As schematically depicted in Figure 2.3, the basic experimental setup is composed of a waveform generator (Agilent 33120A), a high-voltage amplifier (Trek Model 20/20C), a Dynamic Mechanical Analyzer (Perkin-Elmer DMA7e), a current/charge measuring circuit and an oscilloscope (Tektronix TDS5034B).

2.2.1 Hysteresis Loops

The current flowing through, and the charge generated by the piezoelectric ceramic fiber, are measured using the current/charge measurement circuit schematically depicted in Figure 2.4. The current measuring circuit con-

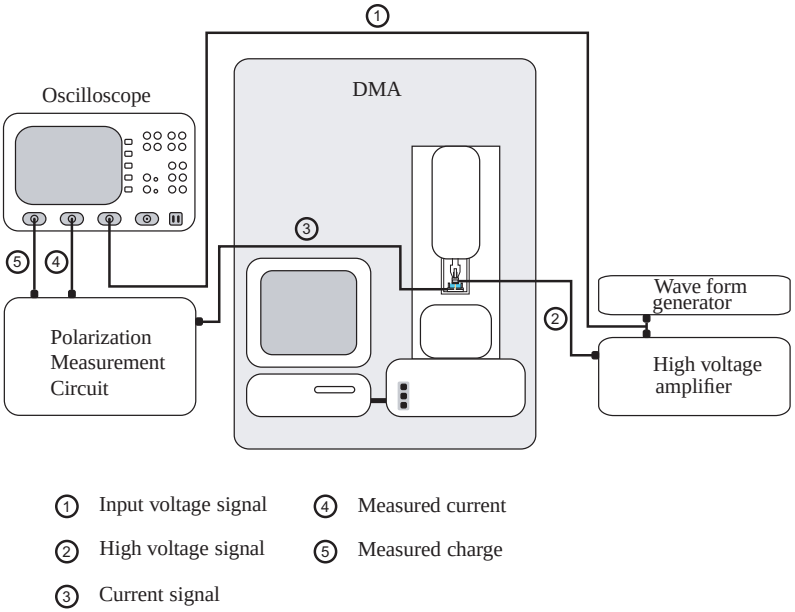

Figure 2.3: Experimental setup, consisting of a waveform generator, a high-voltage amplifier, a Dynamic Mechanical Analyzer, a current/charge measuring circuit and an oscilloscope.

sists of a transimpedance amplifier. The low-pass filter resulting from the addition of the capacitor $C1$ enhances stability, reducing overshoot and oscillations in the output signal. Its cut-off frequency is approximately 160Hz. The output voltage signal is proportional to the current flowing through the piezoelectric ceramic fiber investigated. This signal is fed into a voltage follower that has high input impedance, low output impedance and unity gain. Its purpose is to decouple the charge measurement from the current measurement. The charge stored on the test fiber is determined by an OpAmp integrator. This corresponds to an inverting resistance-feedback

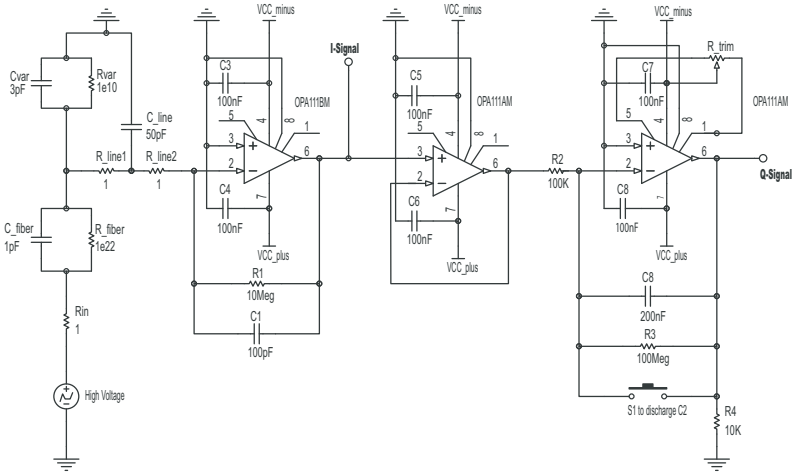

Figure 2.4: Current/charge measuring circuit for single piezoelectric fibers, consisting of a transimpedance amplifier, a voltage follower, and an OpAmp integrator.

amplifier with the addition of a feedback capacitor $C8$. The resistor $R3$ has DC stabilization purposes. R_{trim}, a trimming potentiometer, allows for the compensation of possible drifts. A varistor protects the measuring circuit (namely its OpAmps) in case of a breakdown. The input impedance of the measuring device is $10M\Omega$, 10-fold higher compared to the oscilloscope.

The current measuring circuit was calibrated using a Keithley 6221 AC and DC Current Source. The relative error between input current and measured current was found to be less than 1%.

The voltage monitoring signal from the high-voltage amplifier is displayed as the horizontal deflection of the oscilloscope. The current, and the charge signal, are displayed as the vertical deflections, yielding the loops shown in Figure 2.5.

Whenever the electrical resistance and capacitance of the specimen can

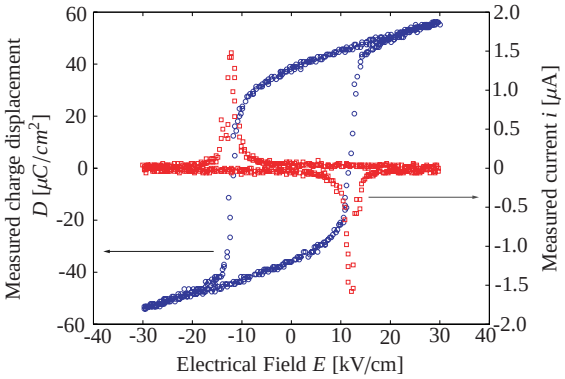

Figure 2.5: Measured charge displacement D (○) and measured current i (□) at $\pm 30 kV/cm$ electrical field, 1Hz. Note the missing saturation in the hysteresis loop, due to the influence of the experimental setup.

be considered independent of the applied voltage, the response of a ferroelectric material to a time-dependent applied voltage can be described by

$$i = C \cdot \frac{dV}{dt} + A \cdot \frac{dP}{dt} + \frac{V}{R} \tag{2.1}$$

where i is the current, C is the specimen capacitance, A is the specimen cross-sectional area, V is the applied voltage, t is the time, P is the ferroelectric polarization, and R is the electrical resistance of the specimen. This current consists of a capacitive current, a resistive contribution and the polarization or switching current. Hence, corrections must be made for electrical capacity and conductivity.

According to the ceramic manufacturer [62], the volume resistivity of PZT5A is in excess of $10^{11} \Omega m$. The conduction of the investigated piezoelectric ceramic fibers was therefore estimated to be three orders of magnitude lower than the capacitive response, and thus considered negligible. The dielectric charge Q_{Setup} to be ascribed to the experimental setup (mainly the condenser built by the measuring electrodes and the silicon

oil, in parallel to the piezoelectric ceramic fiber to be investigated) was determined by measuring a glass fiber in the original setup (Figure 2.6), multiplied by the ratio between the length of the dummy glass fiber and the investigated piezoelectric ceramic fiber and subtracted from the total charge measured during the tests.

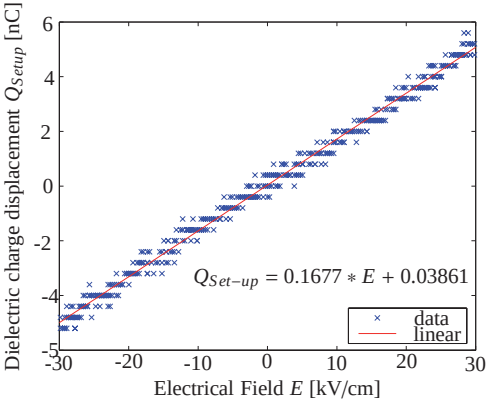

Figure 2.6: Dielectric charge displacement of the measuring setup, determined by using a glass fiber.

The resulting polarization P can be then described as:

$$P(E) = D(E) - \epsilon_F E = \frac{Q - Q_{Setup}}{A_F} - \epsilon_F \frac{V}{t_F} \tag{2.2}$$

where, Q is the measured charge, A_F the piezoelectric specimen's cross-section, ϵ_F the dielectric constant of the fiber material investigated, V the applied voltage, and t_F the piezoelectric specimen's length, respectively. The low field dielectric constant of the poled piezoelectric ceramic fiber was determined using an Impedance/Gain Phase Analyzer (HP 4194A) and a Dielectric Test Fixture (HP 16451B), both from Hewlett Packard. Following Yoshikawa et al. [57], measurements were carried out at room temperature and 10kHz on fibers 2-3mm in length.

An alternative to the correction presented here is the bipolar loop/unipolar loop method proposed by Dickens et al. [55]. The integration of the current would then have to be performed by a software package.

Fibers were prepared as described previously in this section and mounted in the DMA measuring system to ensure nearly free-strain conditions throughout the measurements (see next section). A linear ramp signal was then used to generate electrical field strengths up to 30kV/cm at 1Hz.

2.2.2 Butterfly Loops

In order to measure the high field, free-strain properties of single piezoelectric fibers, the equipment must fulfill three basic functions: to apply a voltage to the electroded fiber ends; to control and minimize the force applied to the sample; and to detect fiber elongation. The second and the third requirements can be fulfilled by a Dynamic Mechanical Analyzer having sufficiently high sensitivity. The instrument - a DMA 7e from Perkin Elmer - comprises four functional components: motor, detector, measuring system, and environmental system. The force generated by the motor is applied to the sample through the central core rod which is suspended in a magnetic field. The linear force motor can produce -8000mN to +6500mN force with a sensitivity of 0.01mN up to 51Hz. The detector, a linear variable differential transformer (LVDT), measures the vertical elongation of the sample with a sensitivity of $0.02\mu m$ in the range -5mm to +5mm. The measuring system allows the sample holder to be mounted easily as depicted in Figure 2.2. If desired, the environmental system would allow investigations in the temperature range -150°C to +600°C.

After mounting the sample holder in the measuring system, a force of 0±0.01mN was applied to enforce nearly free-strain conditions. Due to the relatively limited sampling frequency of the instrument (1Hz), voltage was applied at 2.8mHz to give cycle times of 6 min. A linear ramp signal was used to generate electrical field strengths up to 30kV/cm. The measured displacement is recorded by the DMA software, divided by the active fiber length and plotted against the applied electrical field strength.

2.2.3 Blocking Force

Using the same experimental arrangement as in the previous section, the displacement response was measured for single fibers subjected to a clamping force. The static force was applied by means of the DMA force motor and varied from 0 to 400mN in 80mN steps. For each force step, the applied electrical field strength was stepwise increased to 30kV/cm, yielding force-displacement curves. The blocking force values for a given actuation field can be interpolated from the measured data.

2.3 Results

2.3.1 Hysteresis Loops

Figure 2.7 depicts a polarization loop measured at ±30kV/cm for a fiber from Smart Material, Corp. 250μm in diameter. Its behavior is characterized by a coercive field E_C of 12kV/cm, a saturation polarization P_s of 43.5 $\mu C/cm^2$ and a remanent polarization P_r of 36.6 $\mu C/cm^2$. The hys-

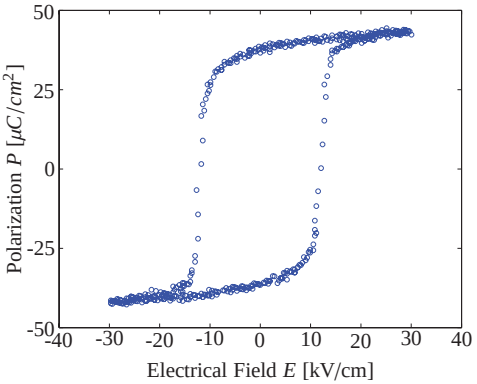

Figure 2.7: Polarization loop measured at ±30kV/cm electrical field strength, 1Hz.

teresis loops for the same fiber at different electrical field strength values are depicted in Figure 2.8. All measurements were carried out at 1Hz. The good repeatability of the measurement is shown in Figure 2.9, with

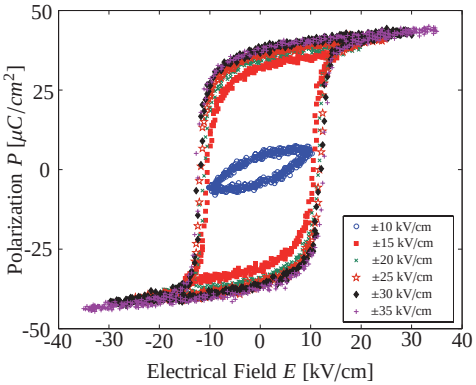

Figure 2.8: Polarization loops measured at different electrical field strength values, 1Hz.

five measurements carried out on the same fiber. The sample holder was removed and put in place again after each measurement.

The presented current/charge measuring circuit provides a simple and efficient method to determine the hysteresis loops in single piezoelectric ceramic fibers. The variation of the $C1$ and $R1$ values (Figure 2.4) allows the investigation of samples having different capacitance values, such as 1-3 composites [52] or piezoelectric foams [63, 64].

Comparison between 1-3 composite and single fiber measurements

The fiber's polarization can be extracted from the 1-3 composite response, provided the volume fraction, the stiffness of each phase, the matrix per-

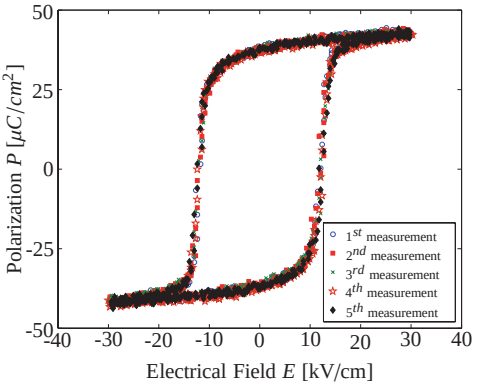

Figure 2.9: Polarization loops measured at ±30kV/cm electrical field, 1Hz. Even though the sample holder was removed and put in place again after each measurement, good repeatability was achieved.

mittivity, and the fiber d_{33} are known [46, 52].

$$P^f(E) = \frac{1}{\nu}\left\{\overline{P}(E) - [(1-\nu)P^m(E)] + \left[\frac{\nu(1-\nu)d_{33}^2(E)E}{\nu s_{11} + (1-\nu)s_{33}^E}\right]\right\} \tag{2.3}$$

where, ν is the fiber volume fraction, $d_{33}(E)$ is the fiber d_{33} coefficient at electrical field E, and s_{11} and s_{33}^E are the compliances of the matrix and fiber respectively. As pointed out by Nelson et al. [52], the clamping effect of the matrix is negligible at high volume fractions. This is the case for the 1-3 composites used in the present study. The average hysteresis loop from 12 single fiber measurements is plotted in Figure 2.10. The hysteresis loops from the 1-3 composites investigated fall within the 99.9% confidence interval resulting from the standard deviation of the 12 single fiber measurements. No statistically relevant difference can be recognized between the two measurement procedures.

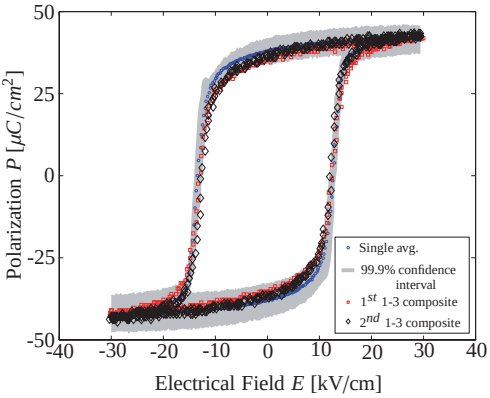

Figure 2.10: Average polarization loop of 12 single fibers and 99.9% confidence interval; polarization loops of two 1-3 composites. Measurements carried out at 1Hz. The plots reveal no statistically relevant difference between the two measurement procedures.

2.3.2 Butterfly Loops

Figure 2.11 depicts a butterfly loop measured at ±30kV/cm for a fiber from Smart Material, Corp. 250μm in diameter. The fiber achieves a free saturation strain of approximately 3700$\mu\epsilon$ peak-to-peak.

The good repeatability of the measurement is shown in Figure 2.12, with six measurements carried out on the same fiber. The sample holder was removed and put in place again for measurements 4-6.

Comparison between 1-3 composite and single fiber measurements

The 1-3 composites were mounted in the DMA measuring system to ensure nearly free-strain conditions throughout the measurements. Butterfly loops were measured at field levels up to ±30kV/cm.

The free fiber piezoelectric strain can be evaluated from the 1-3 composite response by compensating for the restraining mechanical strain, im-

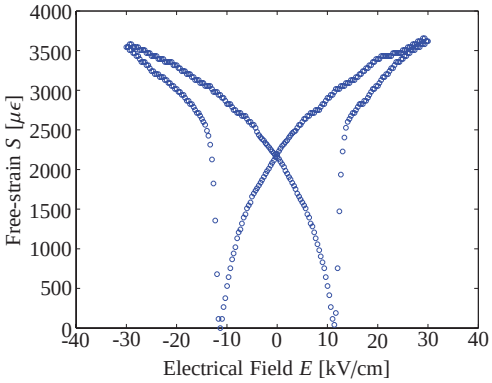

Figure 2.11: Butterfly curve measured at ±30kV/cm electrical field strength. Fiber from Smart Material, Corp., 250μm in diameter.

posed by the polymer matrix [46, 52]:

$$S^{f}_{piezo}(E) = \overline{S}(E)\left[\frac{\nu s_{11} + (1-\nu)s^{E}_{33}}{\nu s_{11}}\right] \tag{2.4}$$

where, ν is the fiber volume fraction, and s_{11} and s^{E}_{33} are the compliances of the matrix and fiber respectively. The average butterfly loop from 12 single fiber measurements is plotted in Figure 2.13. The butterfly loops from the 1-3 composites investigated fall within the 99.9% confidence interval resulting from the standard deviation of the 12 single fiber measurements. Again, no statistically relevant difference can be recognized between the two measurement procedures.

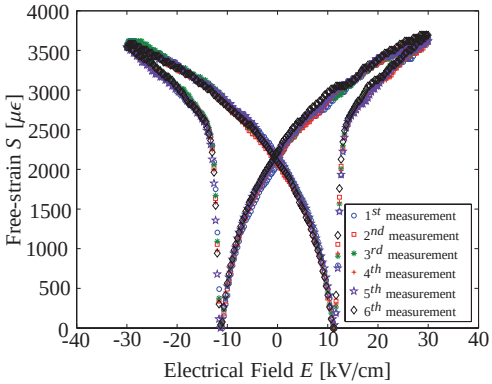

Figure 2.12: Butterfly curves measured at ±30kV/cm electrical field strength. A good repeatability can be observed. The fiber was removed and put in place again for the 4^{th}, 5^{th} and 6^{th} measurement.

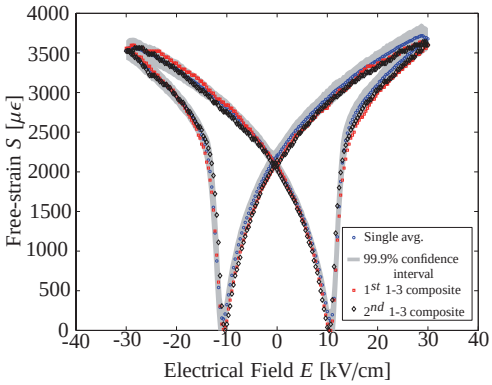

Figure 2.13: Average butterfly loop of 12 single fibers and 99.9% confidence interval; butterfly loops of two 1-3 composites. The plots reveal no statistically relevant difference between the two measurement procedures.

2.3.3 Blocking Force

Figure 2.14 shows the elongation of a fiber (250μm in diameter - from Smart Material, Corp.) as a function of clamping force and applied electrical field strength. The linear response of the fiber is consistent with the response known from bulk PZT materials and suggests that two measuring points, typically zero force and a load well below the fiber ceramic compressive strength, are sufficient to characterize the displacement response at a given applied electrical field strength.

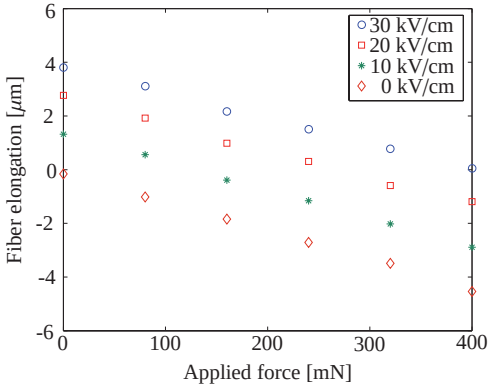

Figure 2.14: Fiber tip displacement as a function of the applied electrical field strength and force.

To the knowledge of the authors, force-displacement curves and blocking force values for single piezoelectric fibers have not been reported before.

2.4 Conclusions

The present Chapter proposed a novel comprehensive procedure for the ferroelectric characterization of single piezoelectric ceramic fibers. Butterfly and hysteresis loops and force-displacement curves were measured using an experimental setup composed of a waveform generator, a high-voltage amplifier, a Dynamic Mechanical Analyzer, a current/charge measuring circuit, and an oscilloscope. The comparison between single fiber measurements and the investigation of 1-3 composites revealed both procedures to be equal, at 99.9%, in determining the average strain and polarization properties. In addition, the single fiber measurement provides an estimation of the variation in fiber properties within a single production batch. This information is essential to understand how to optimize processing routes and build robust devices. The procedure was used by Heiber et al. [65] to characterize commercially available fibers and to compare their performance with fibers developed at Empa. The results from that study are summarized in the next Chapter.

Chapter 3

Ferroelectric Characterization of Single Piezoelectric Fibers

The work presented in this Chapter can be found with minor modifications as a publication in the scientific literature as:

J. Heiber, A. Belloli, P. Ermanni and F. Clemens. Ferroelectric Characterization of Single Piezoelectric Fibers. *Journal of Intelligent Material Systems and Structures*, 20(4):379-385, 2009.[1]

In the previous Chapter, a comprehensive procedure was presented for the direct characterization of single piezoelectric ceramic fibers in terms of butterfly and polarization loops and blocking force. The ability to investi-

[1]The first and second authors contributed in equal manner to the scientific results and to the redaction of this article. The first author explicitly consents the present chapter be included into this thesis.

gate single fibers is relevant for optimizing their manufacturing processes, for quality control purposes, and for modeling the response of components and structures. In this Chapter the novel testing procedure is used to characterize commercially available fibers distributed by Advanced Cerametrics Inc., CeraNova Corp., and Smart Material Corp., respectively, and to compare their performance with fibers developed at Empa. Their porosity, grain size and phase composition were investigated to correlate the ferroelectric properties with the microstructure. Fibers supplied by Smart Material Corp. exhibited the best ferroelectric performance, in particular the highest saturation and remnant polarization, the lowest coercive field and the highest P–E loop squareness. The said properties result from a low porosity, a sufficiently large grain size and a phase composition near the morphotropic phase boundary. After removing a surface layer dominated by a rhombohedral phase, Empa fibers developed maximum average free-strains 15% larger than any commercially available fiber. Better control of the sintering atmosphere thus promises to be the key to very high performance fibers.

3.1 Introduction

Piezoelectric ceramic fibers are key components for orthotropic sensing and actuation. Several processes were developed to produce PZT fibers in a certain diameter range. Examples thereof are the sol-gel route [66], a combined sol-gel-extrusion process [67], an electrospinning method [68] or an electrophoretical coating procedure of SiC fibers with PZT [69]. However, only fibers fabricated via the viscous suspension spinning process VSSP [43], the ALCERU method [44] and the extrusion route [45] are commercially available.

All three major techniques use previously synthesized PZT powder as the starting material, which is either dispersed in water and subsequently mixed with viscose or cellulose (VSSP and ALCERU, respectively) or compounded with a thermoplastic material (thermoplastic extrusion). The yield mixtures are extruded through dies with appropriate orifice dimensions. For fiber forming, solidification and purification VSSP and AL-

CERU fibers have to pass through several acid and salt containing baths [70, 71]. Finally, the green fibers are thermally debound and sintered at temperatures up to 1200 °C. With these techniques fiber diameters down to 15, 30 and 80 μm can be fabricated using the VSSP, the ALCERU or the extrusion process, respectively [58, 71, 72].

The ALCERU process differs only slightly from the VSSP method. The major difference is the use of natural cellulose fibers as a carrier material as opposed to viscose. Thus, based on the CS_2-free Lyocell method known from the textile industry, the ALCERU process requires fewer production steps, puts less impact on the environment and offers the possibility of producing PZT fibers with a high purity [44]. Both methods, however, require strict control of the process parameters (e.g. acid concentrations in the spinning, coagulation and finishing baths) and the sintering temperatures are clearly in excess of 1000 °C where lead zirconate titanate starts to decompose [73, 74]. The extrusion process is characterized by an achievable powder-loading content in the green fiber of more than 92 wt.-% and a relatively high variability of the fiber cross-sectional geometry. Because of its low number of processing steps and parameters to control, extrusion represents a rather economical technique [45, 75].

Up to now only extruded or sol-gel-derived single fibers have been characterized with regard to their ferroelectric properties. Bent [61] investigated the strain S developing as a function of the applied electrical field E (butterfly curves), while Yoshikawa [57] and Bystricky [58] measured the polarization P as a function of the applied electrical field (hysteresis curves). However, none of these authors has given any validation for their measurements. Otherwise, the fibers are tested in a composite structure [72, 52] where the fiber properties are extracted from the composite response and symbolize an average value of a multiplicity of fibers. To the knowledge of the author, Nelson and co-workers [52] were the first to characterize and compare all commercially available fibers using 1-3 composites and they found VSSP fibers performed best in terms of free-strain, polarization, coercive field and hysteresis. However, the microstructural properties such as grain size, porosity and phase composition of the investigated fibers are not given, making any comparison very difficult. A later study by Dent et al. [76] presented the microstructure of commercially

available PZT-fibers, but the results were not put into any correlation with the ferroelectric properties of the fibers published by Nelson et al. [52].

Single fiber testing methods are essential for the determination of the property dependencies from the fiber homogeneity and microstructure, the investigation of the influences of changes in production parameters, and finally with the view to further improving fiber performance. At the Centre of Structure Technologies, ETH Zurich, new testing methods were developed to fulfill these requirements [77]. These are presented in detail in Chapter 2.

The present Chapter summarizes results from a significant amount of fibers and correlates the observed performance with their intrinsic microstructure. Commercially available fibers are compared with fibers developed at EMPA Duebendorf using a thermoplastic extrusion process [78].

3.2 Materials and Methods

Commercially available PZT fibers fabricated by Advanced Cerametrics Inc. (AC), Smart Material Corp. (SM) and CeraNova Corp. (CN) via the VSSP method, the ALCERU process and the extrusion route, respectively, were chosen to compare their microstructural and ferroelectric properties. The investigated fibers consist of the same piezoceramic material composition (PZT5A) and their fiber diameters are in a similar range of around 250μm. In addition, fibers developed at EMPA Duebendorf were also analyzed. These fibers were produced by mixing a commercial PZT5A type powder (EC65, EDO Corporation) with a thermoplastic binder system, extruding the compound vertically downwards through a die 300μm in diameter and thermally heat-treating the green fibers at 1200°C in a PbO-enriched atmosphere. The production steps are described in more detail in Heiber et al. [79].

All fibers were characterized with regard to porosity, grain size, phase composition near the fiber surface, phase composition of the bulk material and ferroelectric properties (free-strain development and polarization as a function of the applied electrical field).

To determine the porosity and the grain size, fibers were embedded in

a three-component epoxy resin (Technovit 4000, Heraeus Kulzer GmbH & Co. KG), and polished as described in detail by Heiber et al. [78]. The porosity was quantified by performing scanning electron microscopy (Vega Plus 5136 MM, Tescan) and using image analysis (Digital Micrograph 3.10.0, Gatan Inc.). Thereafter, the sample was etched several seconds for grain size visualization using a solution consisting of 5 ml hydrochloric acid, 95 ml distilled water, and 5 drops of a 40-percentage hydrofluoric acid [80]. The grain size was determined by the linear intercept method [81].

X-ray diffraction (XRD) investigations were performed using the X'Pert Pro MPD equipment by PANalytical. Due to the low X-ray penetration depth into PZT materials of 3-4μm [82], the fibers were first measured in silica glass capillaries (Debye-Scherrer configuration) to reveal their surface phase composition [83]. Thereafter, they were crushed, ground, and stuck on silicon single crystal wafers by using Vaseline, in order to obtain information on the average phase composition of the fiber bulk material (Bragg-Brentano configuration [83]). Wide-angle scans of 2Θ from 2° to 120° (Debye-Scherrer configuration) and from 5° to 80° (Bragg-Brentano configuration) with a step width of 0.017° and exposure time of 8 and 2s per step (CuKα-radiation, 40mA heating current, 40kV beam potential) were performed, respectively.

For characterization of their ferroelectric properties PZT fibers were cut into 3.5mm long pieces and placed vertically into a PMMA sample holder (Figure 2.1). Both fiber ends were coated with silver epoxy (Electrodag 5915, Acheson Colloids Company) to apply electrical contact. The active free length of the fibers was thereby shortened to about 2.5mm. The fibers were immersed in silicon oil to avoid an electrical breakdown. Poling was achieved by applying electrical fields of 35kV/cm for 5 min at room temperature. The fibers were subsequently measured in terms of their free-strain evolution as a function of the applied electrical field by using a wave form generator (Agilent 33120A) and a high voltage amplifier (Trek Model 20/20C). The free-strain evolution was recorded for electrical fields ranging from -30kV/cm to +30kV/cm with a frequency of 2.8mHz using a Dynamic Mechanical Analyzer (Perkin Elmer DMA 7e). This piece of equipment can apply forces to the sample with a sensitivity of 0.01mN,

thus enforcing nearly free-strain conditions.

Hysteresis curves were measured at room temperature using the same DMA setup and a current/charge measurement circuit for charge collection (Figure 2.4). The measured current consists of a capacitive, a resistive (considered to be negligible) and a polarization contribution. Corrections have thus to be made for determining the polarization response:

$$P(E) = \frac{Q - Q_{Setup}}{A_F} - \epsilon_F E \tag{3.1}$$

wherein, Q describes the measured charge, Q_{Setup} the dielectric charge contributed by the experimental setup, A_F the cross-section of the PZT fibers and ϵ_F the fiber dielectric constant measured using an Impedance/Gain Phase Analyzer (HP 4194A) and a Dielectric Test Fixture (HP 16451B). The electrical field E was applied as a linear ramp signal having a strength of up to 30kV/cm with a frequency of 1 Hz.

3.3 Results

3.3.1 Microstructure of the Investigated Fibers

The ferroelectric properties of PZT materials depend mainly on their microstructure, i.e., density or rather porosity, grain size, chemical composition, and phase composition. Table 3.1 summarizes the fiber diameter, porosity and grain size values measured for AC, CN, SM and Empa fibers. Among the fibers investigated, AC fibers showed the highest porosity (approx. 10%) and the largest grain size (approx. $4\mu m$), suggesting insufficient sintering. Apart from the slightly higher amount of pores for CN fibers, the remaining fibers exhibit comparable values for the porosity and the grain size. Figures 3.1 and 3.2 show XRD profiles in a 2Θ range between 40° and 48° for the fiber bulk material and the fiber surface, respectively.

The XRD profiles depict the (h0k)-reflection peaks at around 44°. For compositions close to the desired morphotropic phase boundary (MPB) - where maximum ferroelectric properties are expected - the tetragonal

Table 3.1: Fiber diameter, porosity, and grain size of PZT5A fibers. Average values and standard deviation for 10 fibers.

Fiber name	AC	CN	SM	Empa
Production method	VSSP	Extrusion	ALCERU	Extrusion
Fiber diameter [μm]	241 ± 7	282 ± 1	252 ± 8	280 ± 9
Porosity [%]	10.1 ± 1.3	3.6 ± 0.5	2.1 ± 0.4	1.8 ± 0.4
Grain size [μm]	3.8 ± 1.2	2.1 ± 0.2	1.8 ± 0.1	1.9 ± 0.8

and rhombohedral phases coexist. Due to the small differences between the tetragonal and rombohedral lattice parameters, many of the diffraction lines in the coexistence region overlap to some degree. In the present work, the (200) plane was selected, where three distinct lines are produced, i.e., $(002)_T$, $(200)_R$ and $(200)_T$ [84]. The different stages of overlapping can be seen in Figure 3.1. A clearly detectable peak splitting, and nearly completely separated reflexes, indicate a predominant tetragonal phase and a low amount of rhombohedral phase. This is the case for the XRD patterns of the AC and CN fibers depicted in Figure 3.1 (bulk material). The shoulder on the tetragonal peak for the Empa and SM fiber bulk material indicates a larger amount of rhombohedral phase, and thus a composition closer to the morphotropic phase boundary. Summarizing, Figure 3.1 reveals that AC and CN fibers consist of a higher amount of tetragonal phase than SM and Empa fibers. Figure 3.2 depicts the XRD profiles measured at the fiber surface. All fibers but the SM fibers show distinct profiles for the bulk and surface compositions. The changes in phase composition are especially pronounced in the case of Empa fibers. Due to the sintering conditions, these consist predominately of a rhombohedral phase at the surface. Conversely, CN fibers show a larger amount of tetragonal phase at the fiber surface, as indicated by a more pronounced peak splitting.

The effect of sintering on the surface phase composition was investigated. A surface layer $30\mu m$ in thickness was removed from Empa fibers by using the etching solution given in Section 3.2. Figure 3.3 shows a fiber cross-section, the original contour and the one after removing the surface layer. The respective XRD profiles disclose the phase compositions.

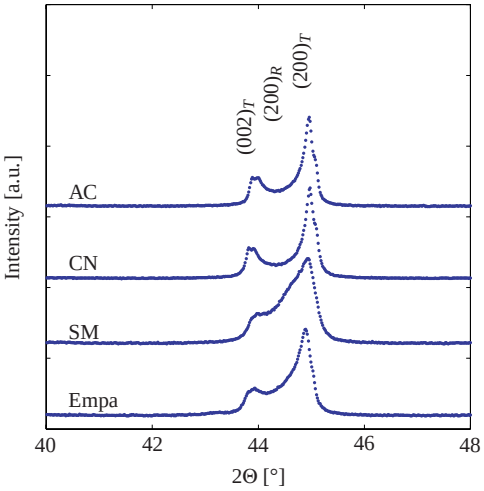

Figure 3.1: X-ray diffraction profiles between 40° and 48° for the fiber bulk material (T - tetragonal phase; R - rhombohedral phase).

While the rhombohedral phase predominates near the initial fiber surface (23±10 wt% of tetragonal phase), a higher fraction of tetragonal phase is present 30μm below (59±9 wt%), as visualized by a split peak. In the case of Empa fibers, these changes across the fiber radius are caused by the lead oxide-enriched sintering atmosphere that leads to a lead oxide absorption accompanied by a titanium oxide loss. The grain fracture behavior (from intergranular to transgranular) and the chemical composition were found to vary as well, whereas the porosity and the grain size were relatively unaffected [78]. Secondary phase - which might affect the ferroelectric performance - was not found by X-ray in any of the fibers investigated.

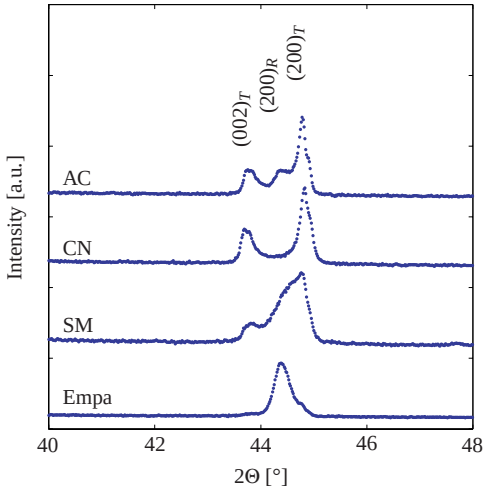

Figure 3.2: X-ray diffraction profiles between 40° and 48° for the fiber surface (T - tetragonal phase; R - rhombohedral phase).

3.3.2 S(E)-Behavior

The free-strain evolution S as a function of the applied electrical field E was measured for 10 single fibers from each manufacturer. The maximum free-strain S_{max} and the coercive field E_C are obtained from the butterfly curves. Figure 3.4 depicts average butterfly curves of the fibers investigated. Average values and standard deviation for the maximum free-strain S_{max} and the coercive field E_C are summarized in Table 3.2.

The investigations showed that the etched Empa fibers developed the highest average maximum free-strain. The remaining fibers reached a comparable average S_{max}, whereas the CN fibers with about 4000$\mu\epsilon$ showed slightly better and the AC fibers with 3600$\mu\epsilon$ slightly worse strain properties. The reduced properties of the AC fibers might be caused mainly by the higher porosity [58, 85], whereas the better properties of CN fibers

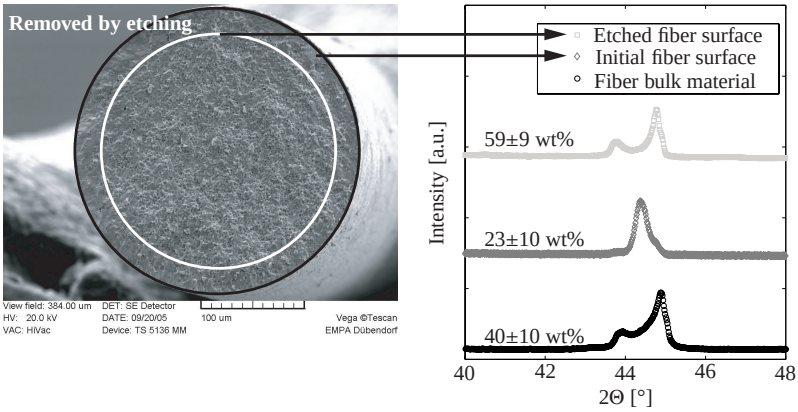

Figure 3.3: (a) Fiber cross-section of an Empa fiber; original contour (black) and the one after removing the surface layer (white). (b) Corresponding XRD profiles and relative amounts of tetragonal phase, determined by Rietveld analysis.

could be explained by their phase composition. As with the CN fibers, etched Empa fibers consist of a phase composition dominated by a tetragonal phase (assuming the phase composition at the etched fiber surface to be representative for the bulk material). Nevertheless, etched Empa fibers develop a significantly higher maximum free-strain. This could be explained by the lower porosity in Empa fibers. The relatively high coercive field strength of CN fibers (E_C = 13.8kV/cm) - on the other hand - indicates that the CN fibers consist of a larger amount of the tetragonal phase than the etched Empa fibers [86]. This leads to the assumption of a phase composition further from the desirable morphotropic phase boundary, resulting in the lower maximum free-strain of CN fibers compared to etched Empa fibers [87].

Etching of the Empa fibers revealed significant changes in the phase composition across the fiber diameter. Again, the significant increase in coercive field values suggests a larger relative amount of tetragonal phase.

Table 3.2: Maximum free-strain S_{max} and coercive field E_C. Average values and standard deviation for 10 fibers.

Fiber	S_{max} [$\mu\epsilon$]	E_C [kV/cm]
AC	3600 ± 400	10.5 ± 0.8
CN	4000 ± 500	13.8 ± 1.1
SM	3700 ± 300	10.7 ± 1.0
Empa	3800 ± 200	9.2 ± 0.5
Empa_{etched}	4500 ± 350	10.1 ± 0.3

After removing the surface layer (30μm thick), dominated by the rhombohedral phase, the average maximum free-strain was enhanced by 15%.

3.3.3 P(E)-Behavior

The polarization P as a function of the applied electrical field E was investigated. Average values and standard deviation are summarized in Table 3.3 for the saturation polarization P_s, the remanent polarization P_r, the coercive field E_c and the loop squareness. Average hysteresis loops are shown in Figure 3.5. The dielectric constant ϵ_r measured at 10 kHz - needed for subtracting the capacitive contribution from the charge collected - is also given in Table 3.3. The hysteresis measurement results reveal average saturation polarization values for SM, Empa and etched Empa fibers of up to $40\mu C/cm^2$. CN and AC fibers do not quite match this performance. The similar behavior of SM and Empa fibers is in line with their comparable phase composition for bulk material, porosity and grain size. SM fibers show a slightly lower coercive field due to a larger amount of rhombohedral phase as opposed to Empa fibers. Conversely, the larger amount of tetragonal phase in etched Empa fibers is responsible for a higher coercive field compared to the original Empa fibers. However, the changes in chemical composition across the fiber diameter, do not show such a large influence on the polarization behavior as is the case of the strain response (Section 3.3.2).

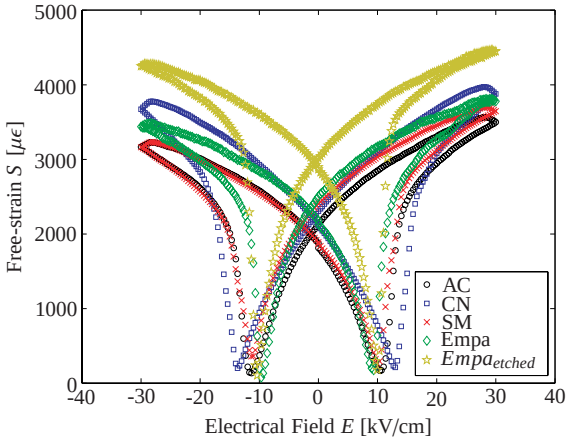

Figure 3.4: Average butterfly curves (10 fibers each).

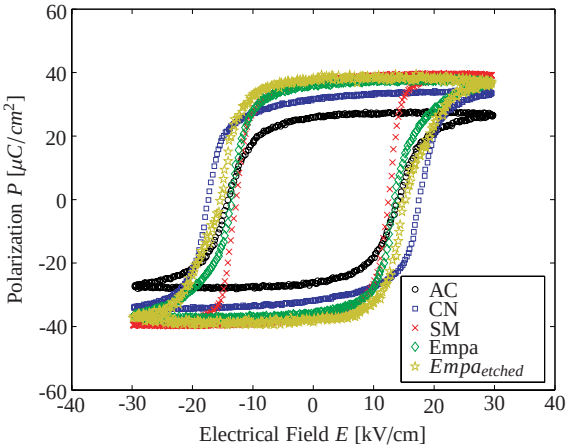

Figure 3.5: Average hysteresis curves (10 fibers each).

Table 3.3: Dielectric constant ϵ_r (measured at 10kHz), saturation P_s and remanent polarization P_r, coercive field E_C and hysteresis loop squareness (measured at 1Hz). Average values and standard deviation for 10 fibers.

Fiber		AC	CN	SM	Empa	$Empa_{etched}$
ϵ_r	[-]	1140 ± 50	1010 ± 70	1110 ± 70	1090 ± 70	1040 ± 60
P_s	$[\mu C/cm^2]$	27.8 ± 2.3	34.6 ± 1.8	39.6 ± 2.0	37.3 ± 2.2	37.8 ± 0.7
P_r	$[\mu C/cm^2]$	25.8 ± 1.5	31.7 ± 2.1	37.0 ± 1.9	36.1 ± 2.3	38.2 ± 0.2
E_C	[kV/cm]	14.1 ± 0.5	17.3 ± 0.5	12.5 ± 0.8	13.6 ± 0.9	14.9 ± 0.4
Squareness	[-]	1.3 ± 0.1	1.3 ± 0.1	1.5 ± 0.1	1.3 ± 0.1	1.3 ± 0.1

According to Haertling and Zimmer [88], the polarization properties are significantly affected by the microstructural properties. Material density has a large influence on the remanent polarization, whereas the coercive field mainly depends on the grain size. While having comparable phase compositions, CN and AC fibers show significant differences in porosity and grain size. The lower remanent and saturation polarization values of AC fibers can consequently be attributed to their higher porosity. Their larger grain size, on the other hand, explains the lower coercive field compared to CN fibers.

A comparison between the results from the hysteresis and the butterfly measurements reveals a significant discrepancy in coercive field values. Distinct measuring frequencies (1Hz for the hysteresis loops, 2.8mHz for the butterfly loops) are assumed to be the reason for such differences. A preliminary investigation - carried out exemplarily on CN fibers - yielded larger coercive field values for increasing measuring frequencies (Figure 3.6). The results presented in this study were measured at 1Hz, as are most values given in literature.

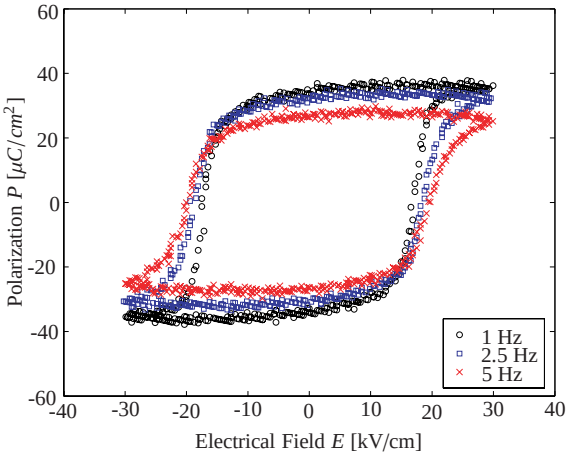

Figure 3.6: Frequency dependence of the hysteresis loop for CN fibers.

As per Bystricky [58], an optimal ferroelectric material exhibits high remanent polarization, low coercive field, no conductivity, and a square-shaped hysteresis loop. Signs of conductivity were not found in any of the samples investigated. High remanent polarization and low coercive fields were measured in SM and Empa fibers. In particular SM fibers also exhibit a high $P-E$ loop squareness R_{sq}, defined as:

$$R_{sq} = \frac{P_r}{P_s} + \frac{P_{1.1E_C}}{P_r} \tag{3.2}$$

where $P_{1.1E_C}$ corresponds to the polarization at an applied electrical field of $1.1E_C$ [88].

3.4 Summary

Three different commercially available PZT fibers and fibers developed at Empa Duebendorf were investigated in terms of their microstructural properties and their ferroelectric response. The observed free-strain response and the polarization behavior were correlated to the measured values for the porosity, the grain size and the phase composition. The strain and polarization investigations were performed using a novel measurement procedure for single fibers developed at ETH Zurich. The following conclusions can be drawn:

- Fibers produced by Smart Material Corp. using the ALCERU method, showed low porosity and a grain size of about $2\mu m$. SM fibers performed best in terms of ferroelectric behavior - reaching the highest saturation polarization, showing a high remanent polarization, having the lowest coercive field and the highest $P-E$ loop squareness.

- Extruded fibers made by CeraNova Corp. exhibit slightly higher porosity that affected mainly the polarization response. Their very high coercive field is a consequence of the large relative amount of tetragonal phase. CN fibers developed the highest free-strain values

among the fibers investigated in this study.

- Fibers produced by Advanced Cerametrics Inc. via the Viscous Suspension Spinning Process showed the highest porosity, the largest grain size and the lowest ferroelectric performance.

- Empa fibers - fabricated via a thermoplastic extrusion route - showed microstructural properties, to a large extent comparable to those of SM fibers. Their ferroelectric performance was accordingly high.

- Compared to the commercial fibers, Empa fibers present a strongly influenced fiber surface with a predominantly rhombohedral phase composition. After removing the surface layer, the Empa fibers show an exceptionally high maximum free-strain of about $4500\mu\epsilon$, while the polarization properties remain unchanged.

- The phase composition was found to influence mainly the strain behavior and the coercive field. The porosity affected the remanent and saturation polarization, whereas the grain size impacted the coercive field.

- Sintering the Empa fibers in a $PbZrO_3$-ZrO_2 enriched atmosphere could represent a way to mitigate the influence of the sintering step on their surface layer.

Based on the present findings, fibers produced by Smart Material Corp. were selected for manufacturing AFC modules used in Chapter 4, Chapter 5, Chapter 7, Chapter 8 and Chapter 10.

Part II

Active Fiber Composites: Modeling and Optimization

Chapter 4

Modeling and Characterization of Active Fiber Composites

The work presented in this Chapter can be found with minor modifications as a publication in the scientific literature as:

A. Belloli, B. Castelli, X. Kornmann, C. Huber and P. Ermanni. Modeling and Characterization of Active Fiber Composites. *SPIE Smart Structures and Materials - Smart Structures and Integrated Systems*, volume 5390, pages 78–88, San Diego, CA, March 2004.

The scientific community has put significant efforts in the manufacturing of sensors and actuators made of piezoceramic fibers with interdigitated electrodes. These allow for increased conformability and actuation capability at high field regime. The prediction of their coupled field behavior, however, is so far limited to low field applications, where the piezoelectric

coupling coefficient is assumed to be constant. An approach, which takes into account the strain driven nonlinearity of a representative work cycle at high field regime is still lacking. This study presents a nonlinear Finite Element Model to simulate the free-strain properties of Active Fiber Composites (AFC) under high electric field conditions. Input data for the fully parametric model are the Representative Volume Element (RVE) geometry and the material properties of its piezoceramic and epoxy resin components. The high field properties of single PZT fibers under free-strain conditions were determined using the characterization procedure described in Chapter 2. Free-strain properties of the actuators were measured experimentally, and important geometrical parameters (contact angle between the fiber and the electrode, average spacing between the fibers) were measured using micrographical imaging. The results of the simulation show good agreement with the free-strain measurements, allowing for prediction of a representative work cycle hysteresis. The influence of important geometrical parameters on the actuator properties such as the electrode spacing and the contact angle between electrode and fiber was investigated both numerically and experimentally.

4.1 Introduction

Active Fiber Composites (AFC) originated from work started at MIT in 1992 [89]. AFC are composed of PZT (lead zirconate titanate) fibers and epoxy resin. Interdigitated electrodes (IDE) are used for poling and to direct the electrical field along the longitudinally oriented PZT fibers (Figure 4.1). AFC achieve greater actuation energy density by exploiting the d_{33} effect along the fibers versus the d_{31} actuation used in most monolithic piezoceramic materials. The use of piezoceramic fibers maintains the majority of the stiffness and the bandwidth of pure piezoceramics, by simultaneously achieving high conformability and thus integrability in complex curved structures. Furthermore, they allow for anisotropic actuation. These properties make AFC interesting components for applications in different fields, such as shape and vibration control.

Analytical and numerical methods were used to predict the perfor-

mances of AFC. In his PhD thesis, Bent [61] proposes an analytical model as summation of parallel and series additions of two phase materials. The resulting Uniform Fields Model (UFM) is thus a generalization of the well known "Rules of Mixtures" and assumes the uniformity of the electrical and mechanical fields in each phase. Compatibility and equilibrium are violated at some interfaces. The UFM simplifies the AFC's complex geometry, thus not taking into account the electrical field distortion under the electrode fingers. Nevertheless, it provides a closed form solution that allows physical insight into the problem. The AFC geometry (i.e. circular fiber cross sections, electrode configuration) can be fully modelled with FE, and electrical field variations in the single phases can be visualized and quantified. This is of special interest in the matrix gap between electrode and fiber and in the "dead-zone" under the electrode finger, where the actuation is supposed to be very small or completely absent.

The influence of configuration parameters on the actuation behavior of AFC has been investigated by different authors, however only for low field actuation. According to Rossetti [90] and Bent [47], AFC with a small electrode spacing p to fiber diameter d ratio show good actuation at lower voltages, but are less efficient due to the steep curvature of the electrical field in the vicinity of the electrode traces. Alternatively, larger p/d ratios are more efficient, but require higher drive voltages to achieve actuation at the same field levels. Nelson [60] claims that 80% of the theoretical maximum strain can be achieved with a p/d ratio greater than 4. Investigating the influence of the interdigitated electrode structure on the strain response of a PZT bulk substrate, he identifies an optimum electrode width to substrate thickness ratio of 0.5.

An approach is still lacking that predicts the strain driven nonlinearity observed in AFC under free-strain conditions. In the scope of this study, a fully parametric FE model is implemented, which predicts the nonlinear work cycle of different AFC configurations. Butterfly loops and work cycles of single PZT fibers - later required for the model - are measured using the procedure developed in Chapter 2. Manufacturing and characterization of corresponding AFC allow for experimental validation of the numerical results.

4.2 FE Analysis

In the scope of this study, the response behavior of AFC is predicted by a FE model. In order to minimize computational requirements, an AFC unit cell is defined, that comprises all relevant parameters. Because of symmetry, the so called Representative Volume Element (RVE) can be defined as an octant of a single fiber and its surrounding matrix included between two adjacent electrode fingers (Figure 4.1).

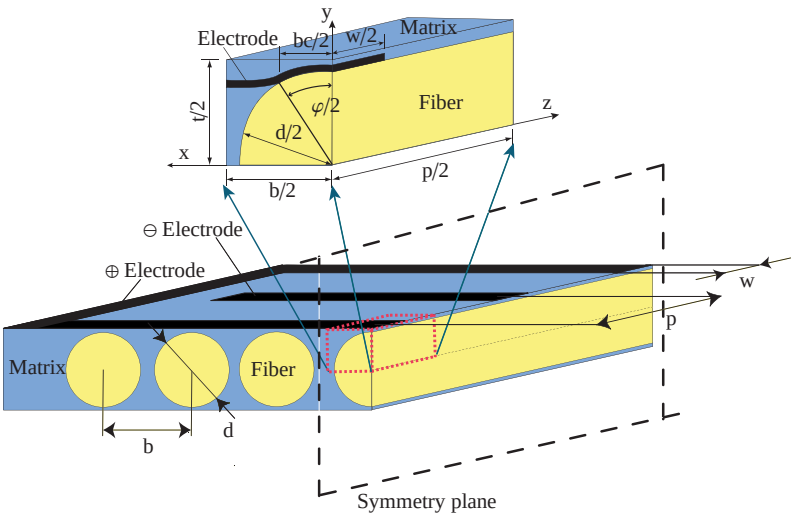

Figure 4.1: Schematic view of an Active Fiber Composite (AFC). The Representative Volume Element (RVE) is defined as an octant of a single fiber and its surrounding matrix included in two adjacent electrode fingers.

4.2.1 Geometrical Parameters

The fiber diameter d, the fiber spacing b, the electrode width w, the electrode spacing p and the contact angle φ are considered in the numerical

model (Figure 4.1). The angle of contact defines the portion of the circular cross-section, which is in contact with the upper resp. lower electrode finger. In addition, the thickness of the insulating polyimide foils is accounted for. w and p were obtained from the AFC manufacturer, whereas the remaining parameters were investigated taking advantage of the micrographical imaging technique (Section 4.3.2).

4.2.2 Material Properties

Stress piezoelectric constants, relative dielectric constants and stiffness constants are summarized in Table 4.1.

Table 4.1: Material properties for PZT5A1 and Epoxy Resin Araldite LY 564 / Aradur 2954.

Fiber		Epoxy	
e_{31} [C/m^2]	-2.8	-	-
e_{33} [C/m^2]	16.4	-	-
e_{15} [C/m^2]	8.4	-	-
$\varepsilon_1^S/\varepsilon_0$	916	$\varepsilon_1/\varepsilon_0$	4
$\varepsilon_3^S/\varepsilon_0$	830	$\varepsilon_3/\varepsilon_0$	4
c_{11}^E [GPa]	120	c_{11} [GPa]	6.52
c_{12}^E [GPa]	75.1	c_{12} [GPa]	3.98
c_{13}^E [GPa]	75.1	c_{13} [GPa]	3.98
c_{22}^E [GPa]	120	c_{22} [GPa]	6.52
c_{23}^E [GPa]	75.1	c_{23} [GPa]	3.98
c_{33}^E [GPa]	111	c_{33} [GPa]	6.25
c_{44}^E [GPa]	21	c_{44} [GPa]	1.27
c_{66}^E [GPa]	21	c_{66} [GPa]	1.27

The experimentally obtained representative work cycle of the investigated AFC reveals a large nonlinear response (Figure 4.6). The strain driven nonlinearity becomes important for free-strain conditions at high

field regime. Accordingly, the piezoelectric response has to be described with constants for low field, respectively strain vs. electric field curves for high field applications.

Since no representative work cycle could be found in the literature, a procedure was proposed in Chapter 2 for the characterization of single PZT fibres. Polynomial interpolation yields characteristic curves $d_{33} = f(E_3)$ for the upward resp. downward sectors of the measured work cycle to be implemented in the free-strain model presented in subsection 4.2.3.

4.2.3 The FE-Model

The AFC's behavior is predicted using ANSYS Direct Coupled Field Analysis. SOLID 5, 8-node 3D multifield elements are used. The mesh is generated in a parametric way, thus assuring similar degree of accuracy for different fiber diameters d and electrode spacings p.

The electrode is not explicitly modeled as shown in Figure 4.1, but defined as an electrical boundary condition. According to Castelli [91], the part of the electrode in the matrix has only little effect on the fiber due to the low resin dielectric constant ε. Consequently, the electrode is only modeled on the fiber, but not in the matrix. A defined voltage is applied to the nodes lying on the surface of the fiber and in the area $0 < z < w/2$ and $0 < x < bc/2$. Because of symmetry, the fiber is grounded at $z = p/2$ and the voltage on the electrode is U/2, where U is the voltage applied to actuate the AFC.

Prediction of the AFC response under free-strain conditions requires the implementation of the nonlinear piezoelectric coefficients (Figure 4.2). For a continuous increase of the tension on the electrodes the homogeneous electric field is determined as $(E_P|_{z=\frac{p}{2}})$. Piezoelectric coefficients $d_{33} = f(E_3)$ are computed using the characteristic curves described in subsection 4.2.2. Values for d_{31} and d_{15} are computed in accordance to following expressions [1]:

[1] Smart Material Corp., 4721 White Tail Lane, Sarasota, FL 34238 USA, www.smart-material.com

$$\begin{array}{lcccc} d_{33} & = & & = & 440\text{pm/V} \\ d_{31} & = & -d_{33}/2.38 & = & -185\text{pm/V} \\ d_{15} & = & d_{33} \cdot 1.27 & = & 560\text{pm/V} \end{array}$$

Stress piezoelectric coefficients are updated according to the constitutive equations [92]:

$$e = dc^E, \tag{4.1}$$

where c^E is the stiffness matrix. For each substep the electric field and free-strain values are computed. Electrical and mechanical boundary conditions are defined in Table 4.2.

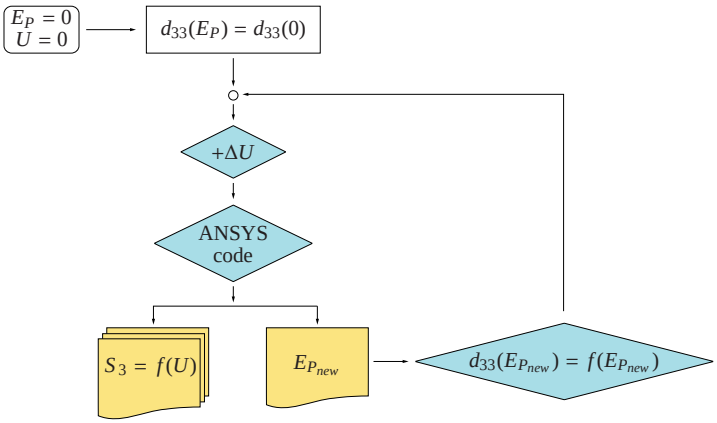

Figure 4.2: Implementation of $d_{33}(E)$ in ANSYS.

4.3 Materials and Methods

Piezoelectric ceramic fibers PZT-5A with a diameter of 255μm were supplied by Smart Material Corporation, Osprey, USA. Polyimide foils of

Table 4.2: Electrical and mechanical boundary conditions for the free-strain model.

Coordinate	Mechanical	Electrical
$x = 0$	$u_1 = 0$	$D_1 = 0$
$y = 0$	$u_2 = 0$	$D_2 = 0$
$z = 0$	$u_3 = 0$	$D_3 = 0$
$x = b/2$	coupled u_1	$D_1 = 0$
$y = t/2$	coupled u_2	$V = U/2$ on electrode ($D_2 = 0$ elsewhere)
$z = p/2$	coupled u_3	$V = 0$

Kapton 100 HN (25μm in thickness) supplied by Dupont, Mechelen, Belgium were used for the preparation of the screen-printed electrodes. The silver paste used for the electrodes was the CB025 from Dupont. The two-component epoxy resin, Araldite LY 564/Aradur 2954 from Vantico AG, Basel, Switzerland, was used in combination with few drops of the antifoaming agent BYK-A530 supplied by BYK-Chemie GmbH, Wesel, Germany as matrix for the AFC.

The high field properties of PZT fibers were determined using a characterization procedure for single fibers described in Chapter 2. The strain versus electrical field response of a single fibre is measured using a Dynamic Mechanical Analyzer. Its force control allows for free-strain conditions during the whole measurement. After poling at room temperature, butterfly loops were recorded. Work cycles were then measured for electrical field values ranging from -9kV/cm to 30kV/cm.

4.3.1 AFC Manufacture

AFC were manufactured by laminating a piezoelectric fiber mat constituted of approximately 75 fibers sandwiched between two screen-printed interdigitated electrodes and embedded in an epoxy matrix [93]. The interdigitated electrodes had a finger width of approximately 200μm, a finger electrode spacing of 700, 900, 1100, or 1300μm and a finger thickness of

approximately 15μm. The active area of the AFC module was 20mm in width and 31mm in length. The AFC were cured under pressure (3.4MPa) in an hydraulic press at 120°C for 1 hour. They were then post-cured 8 hours in an oven at 160°C. They were then poled through the IDE by applying an electrical field of 28kV/cm during 20 minutes in an oven at 80°C.

4.3.2 AFC Characterization

Free-strain Measurement

The free-strain response of AFC was measured thanks to standard 350Ω electrical resistance foil strain gauges (Type 10/350LY11, 10mm in length, 5mm in width) supplied by HBM AG, Naenikon, Switzerland bonded symmetrically on both sides of the AFC and connected in series to an amplifier via a half Winston bridge. Electrical fields between -10kV/cm and 30kV/cm were applied to the AFC in order to generate characteristic actuation curves (i.e. work cycles).

Microscopy

AFC were cut at different angles and observed under the optical microscope (see Figure 4.3). The measured entities were statistically analyzed to obtain realistic parameters. These are listed in Table 4.3.

Electronic Speckle Pattern Interferometry

AFC were finally characterized using Electronic Speckle Patterning Interferometry (ESPI). The method, described in Pini et al. [94], allows for non-destructive investigation of the AFC strain response. Unlike strain gages, which deliver an averaged information over a given region, it gives both local and global information on the deformation response of the sample. The interested reader finds further information on ESPI in Goudemand [95].

ESPI measurements were performed using a Steinbichler 3D-ESPI system. The actuator was held in place on a polypropylene plate with a thin layer of vacuum grease which only minimally affects the deformation in both the actuator's in-plane and out-of-plane directions. The actuator

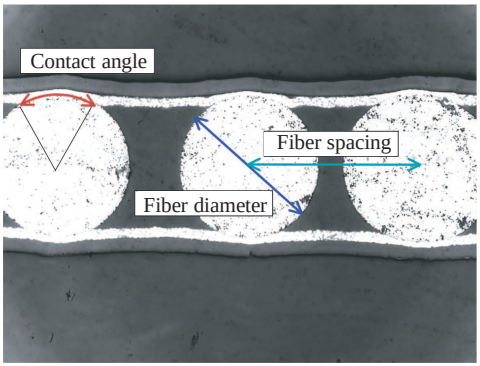

Figure 4.3: Geometrical parameters measured using the micrographical imaging technology. Fiber diameter, fiber spacing, contact angle and electrode thickness are described.

was covered with a thin coating of a white aerosol developer (Magnaflux Spotcheck SKD-S2). The ESPI experimental setup records phase maps for each of the 3 illuminated directions of the actual state, which are then unwrapped and demodulated in 2 displacement fields. Corresponding strain fields are computed from the displacement fields.

4.4 Results

The micrographical imaging investigation revealed a contact region between fiber and electrode. The contact angle is observed to be directly proportional to the pressure applied during manufacturing and to the electrode thickness. The investigated AFC showed a main value of 63.10°, whereas the single values are sensitive to the sequence of fiber diameters, as emphasized by the relatively high standard deviation of 20.81%. A fiber with smaller diameter that the neighbor fibers will have a smaller contact angle to one or both electrodes. The circular fiber cross section presents a main

diameter of 256.6μm with a standard deviation of 1.46%. The main center-to-center fiber spacing is 291.5μm with a standard deviation of 5.17%.

Table 4.3: Geometrical parameters. Fiber diameter d, fiber spacing b and contact angle φ were investigated using the micrographical imaging technology. Values for electrode spacing p and electrode width w refer to the electrode supplier.

Geometrical parameter		Main value	Std. Dev.	CV%
d	Fiber diameter [μm]	256.6	3.75	1.46
b	Fiber spacing [μm]	291.5	15.06	5.17
φ	Contact angle [^{o}]	63.1	13.13	20.81
p	Electrode spacing [μm]	900	-	-
w	Electrode width [μm]	200	-	-

4.4.1 High Field Response of PZT Fibers

Butterfly loops were measured for the used piezoelectric ceramic fiber. Figure 4.4 (a) shows a quite symmetric curve with a developed strain of approximately 3500$\mu\epsilon$. The coercive electrical field lies around 10kV/cm. These results show very good agreement with the literature [52].

The measured work cycle shows a peak-to-peak actuation of approximately 3100$\mu\epsilon$ for an electrical field ranging from -9kV/cm to 30kV/cm. The typical strain driven nonlinearity can be recognized in Figure 4.4 (b).

4.4.2 FE Results for the RVE

The isopotential lines in Figure 4.5 (a) show the potential distribution in the RVE and the negligible contribution of the electrode area separated from the fiber by the epoxy resin. The direct contact between electrode and fiber induces high electrical field near the electrode edge (Figure 4.5 (b)). The resulting strain peak is up to four times larger than the strain in the middle of the fiber, where the electrical field is uniform. Further, a reduction in the strain response along the fiber axis can be observed under the electrode

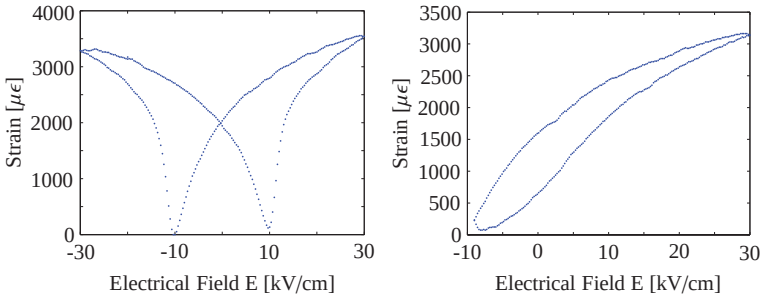

Figure 4.4: Characterization of a PZT5A piezoelectric ceramic fiber via DMA device. a) Butterfly loop, electrical field ±30kV/cm. b) Work cycle for an electrical field ranging from -9kV/cm to 30kV/cm.

in Figure 4.5 (d). This "dead zone" is generated by the distortion of the electrical field under the electrode, as shown in Figure 4.5 (c).

The predicted AFC behavior is presented in Figure 4.6. Free-strain response versus applied voltage was computed for discrete substeps. The clamping effect of the resin and the polyimide foils is reflected in the narrower hysteresis curve, compared to the fiber work cycle in Figure 4.4 (b).

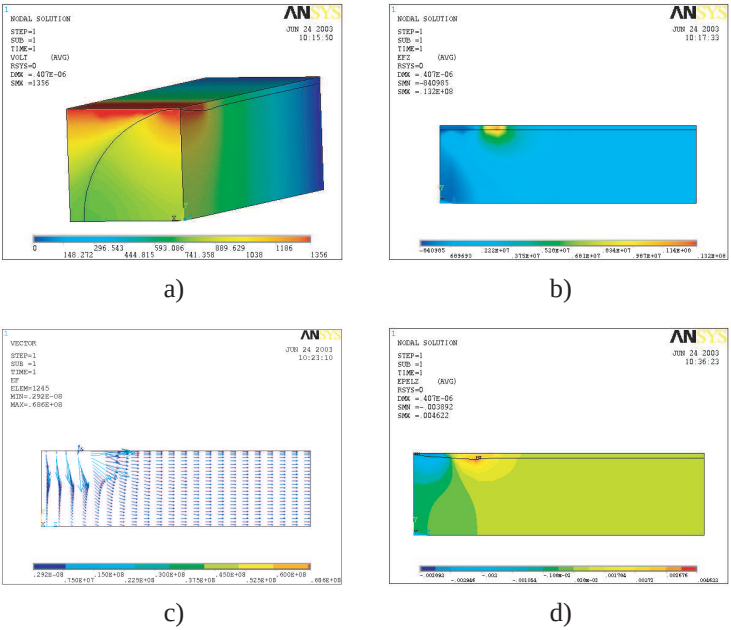

Figure 4.5: FE results. a) Potential distribution in the RVE with contact between electrode finger and fiber. b) Electrical field distribution in the RVE . Notice the field peak near the electrode edge and the ”dead zone” under the electrode surface. Far away from the electrodes, a uniform field distribution can be observed. c) Electrical field lines in the RVE. Notice the field distortion under the electrode. d) Strain distribution in the RVE.

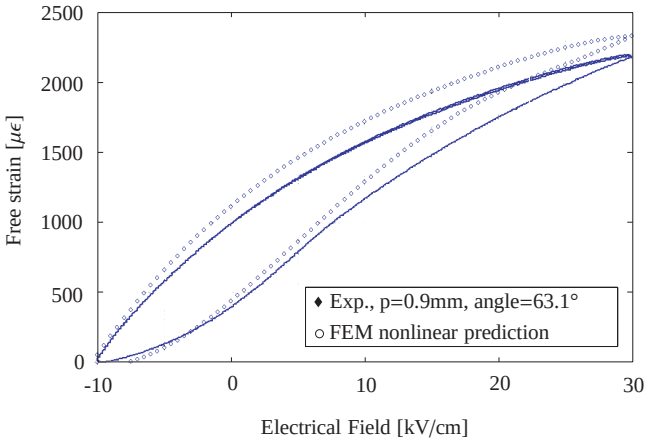

Figure 4.6: Work cycles for an electrical field ranging from -10 to $30kV/cm$. The numerical prediction slightly overestimates the measured free-strain response.

4.4.3 Experimental Results and Validation

Figure 4.6 presents the work cycle measured for the investigated AFC. This presented an electrode spacing p of 0.9mm and a contact angle of 63.10°. The comparison with results from the nonlinear simulation shows a good agreement between the predicted free-strain response and the measured work cycle. The numerical model overestimates the peak-to-peak strain by 6.5%. This is mainly due to the uniformly defined piezoelectric coefficients (see also [60]). Being computed for the electrical field reigning at $z = p/2$, these are clearly exceeding the real values in the ”dead zone” under the electrode. Hysteresis shape and width are accurately predicted.

4.4.4 Parameter Influence

Contact Angle

The contact area between the electrode and the fiber has a large influence on the AFC's performance. Increasing the contact angle for a given electrode width allows for a more efficient field distribution while limiting the "dead zone" under the electrode. On the other hand, increasing the electrode width for a given contact angle would lead to a larger "dead zone" and increase the breakdown risk in the resin matrix. The effective piezoelectric constant was compared to the theoretically attainable for different contact angles. Figure 4.7 shows a large performance enhancement for increasing contact angles, asymptotically approaching the 90% mark. AFC manufactured with different pressures show according contact angles and free-strain actuation. The experimental results are in good agreement with the numerical prediction. Current AFC manufacturing technology is expected to allow contact angles up to 80°. Trough-the-thickness electrodes under development [96] will completely enclose the fibers, thus generating a rotationally symmetric electrical field.

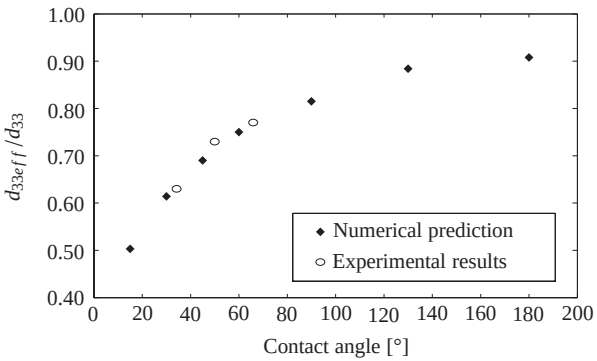

Figure 4.7: AFC performance versus contact angle between electrode and fiber. Experimentally investigated configurations show good agreement with the numerical prediction.

Electrode Spacing

Simulation and experimental results were compared for four AFC manufactured with different electrode spacings. The remaining manufacturing parameters are supposed to be unchanged. A value of 50° was assumed for the typical contact angle. Larger electrode spacings show an actuation improvement. Again, the numerical model overestimates the peak-to-peak strain. Both the experimental curves and the numerical results reveal a decreasing performance enhancement with increasing electrode spacing (Figure 4.8). This is due to the decreasing relative influence of the "dead-zone" under the electrode (w/p-ratio). These findings are in good agreement with results presented by different authors in previous work [90, 47, 60].

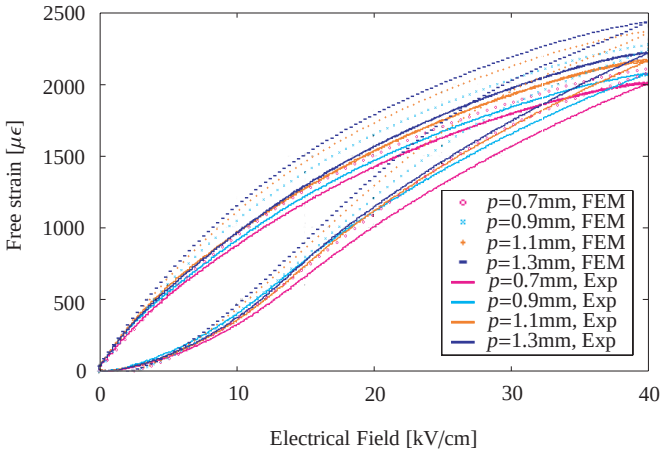

Figure 4.8: Work cycles of AFC manufactured with different electrode spacings. Both experimental and numerical results predict larger peak-to-peak strains for increasing electrode spacing.

4.4.5 Electronic Speckle Pattern Interferometry

Figure 4.9 shows a quantitative strain distribution in longitudinal direction for a representative AFC. Measured by ESPI, these results give insight on both the local and the global deformation response of the sample. Figure 4.9 (b) depicts the regular strain pattern between the finger electrodes. The constraining action of the polymer matrix and the polyimide films is evident at the borders of the investigated module. The "dead-zone" underneath the finger electrodes can be easily recognized in Figure 4.9 (c).

Thanks to its nondestructive nature, the procedure could be used for quality control of AFC to be later integrated in active structural parts, namely to identify possible non-active regions. At the same time the method can also deliver very accurate quantitative strain measurements [94].

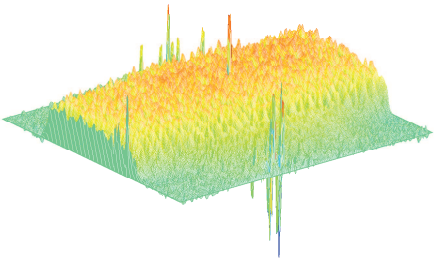

(a) Isometric

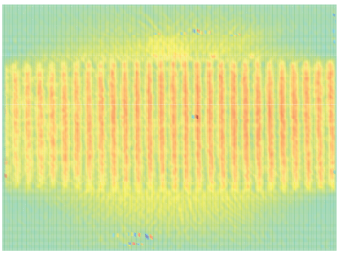

(b) Top

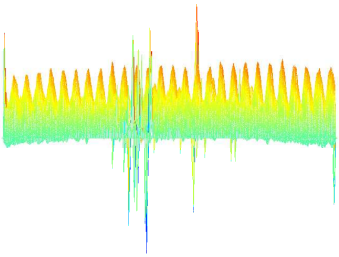

(c) Side

Figure 4.9: Quantitative strain distribution in longitudinal direction for a representative AFC, measured by ESPI. (a) isometric view; (b) top view; (c) side view. Notice the "dead zone" underneath the finger electrodes.

4.5 Conclusions

The free-strain response behavior of AFC under high field conditions has been predicted by a nonlinear FE Model. The micrographical imaging technology was chosen for determination of relevant geometrical parameters. This revealed a direct contact region between electrode fingers and piezoelectric ceramic fibers. Required characteristic curves for the piezoelectric coefficients have been accurately determined using a characterization procedure for single PZT fibers based on the DMA device. The numerical simulation accounted for the AFC's geometrical complexity and gave insight into the electric field and strain distributions. Due to the assumed uniformity of the piezoelectric coefficients, numerical results slightly overestimate the experimentally determined free-strain response. The typical work cycle has been predicted for AFC with different electrode configurations, thus providing a tool for further AFC optimization, as documented in the next Chapter. Numerical and experimental findings corroborate previously published results, revealing enhanced actuation performance for increasing electrode spacing to fiber diameter ratios. Finally, the influence of the contact angle has been investigated, showing interesting potential for further performance improvements. Insight on both the local and the global deformation response of the sample was given by measurements carried out with the ESPI method, a nondestructive procedure that could be used for quality control of AFC to be later integrated in active structural parts.

Chapter 5

Numerical Optimization of Active Fiber Composites

This Chapter presents a comprehensive approach for the optimization of the response of Active Fiber Composites (AFC). Based on a nonlinear finite element model of its Representative Volume Element (RVE) and evolutionary algorithms, it allows the simultaneous investigation of the relevant parameters directly influencing the AFC performance in terms of developed free-strain, generated force per cross-sectional area and capacitance. Free-strain could be enhanced by 14.9%, stress by 6.4% and capacitance by 438% compared to the reference AFC.

5.1 Introduction

Previous work in predicting the actuation performance of AFC shows the influence of configuration parameters on their actuation behavior. Following Rossetti et al. [90] and Bent and Pizzochero [47], a small ratio between electrode spacing p and fiber diameter d enables actuation at lower voltages, but is detrimental to actuation efficiency due to the electric field distortion in the vicinity of the electrode traces. Conversely, larger p/d ratios lead to better actuation efficiency, but require higher driving voltages to achieve actuation at equivalent field levels. Further, higher active fiber volume content results in larger actuation force capability [47].

An approach is still lacking, however, that simultaneously investigates the influence of all main parameters (fiber diameter, electrode spacing and electrode width) on AFC performance. Moreover, different potential applications require the optimization of the corresponding problem objective (e.g. maximum strain, force or capacitance). In this study, both problems are addressed by implementing a finite element model and evolutionary algorithms (EA). Results will be useful for assessing the potential of AFC as active components in structural vibration control.

5.2 Optimization Procedure

For the sake of conciseness, we refrain from elaborating on basic concepts of EA and confine ourselves to a brief description of the application of evolutionary optimization methods to the problem at hand. The interested reader will find more detailed information on EA in [97, 98, 99].

Before evolutionary algorithms can be used for the optimization of any property of the AFC, some preparatory steps have to be carried out. First, a simulation model of the active structure to be optimized is required in order to evaluate the fitness value for each individual. The strain driven nonlinearity becomes important for free-strain conditions at high field regime. Accordingly, the nonlinear finite element model described in Section 4.2.3 is used for the optimization of the AFC's free-strain response S. Conversely, a clamped finite element model with linear piezoelectric relation-

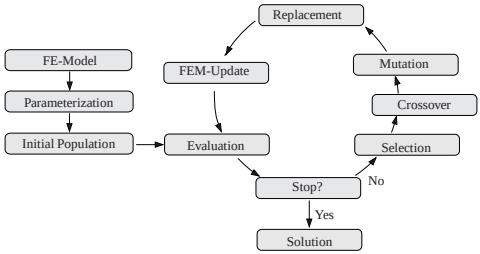

Figure 5.1: Working schedule of evolutionary algorithms.

ships is used to describe the AFC's generated force per cross-sectional area (stress σ) and the capacitance-density C_d. This speeds up the corresponding optimizations.

After defining the simulation model, the optimization process can be set up. The so-called parameterization is the key to an efficient and successful optimization. It has to be defined which parameters are modified during the optimization process. The last task to be accomplished before starting the optimization process is the definition of the evaluation step, in particular of the fitness function. Both aspects are presented in some detail in Sections 5.2.2 and 5.2.3.

Figure 5.1 illustrates a general working schedule for optimization problems addressed with an evolutionary approach. Starting from a randomly initialized population, the optimization loop containing evaluation, selection, crossover, mutation, replacement and model update is iteratively run until a given stopping criterion is satisfied and an optimum design solution is found. A proprietary software tool called DynOPS (Dynamic Optimization Parameter Substitution) written in C++ copes with the complex task of managing the optimization loop. For more detailed information on DynOPS, the interested reader is referred to Wintermantel [98].

5.2.1 Optimization Runs

First, the free-strain developed by the Active Fiber Composite is investigated as a function of the electrode width w and the fiber diameter d, whereas the electrode spacing p is held constant. For optimization runs 2 and 3, the fiber diameter d is then held constant at values corresponding to commercially available fibers. The free-strain is computed as a function of the electrode spacing p and the electrode width w. Finally, the fiber diameter d, the electrode width w and the electrode spacing p are simultaneously optimized for maximum free-strain (optimization run 4), generated force per cross-sectional area (optimization run 5) and capacitance (optimization run 6), respectively (see Table 5.1 for a summary of the optimization runs).

5.2.2 Parameterization

The parameterization links the search space (genotype) to the solution space (phenotype). The following parameters define the RVE:

- Fiber diameter d
- Electrode width w
- Electrode spacing p

Parameter Bounds

Table 5.1 summarizes the parameter bounds defined for the different optimizations. For optimizations 2 and 3 the lower bound for the electrode width w corresponds to the accuracy achievable by the screen printing technology, the method of choice at Empa Duebendorf. The use of alternative technologies (e.g. photolithography) is considered in optimizations 1 and 4 through 6. Even though current PZT fibers with a diameter d<100μm do not show the quality required for manufacturing AFC with reproducible performance, this limit is expected to be lowered to 30μm in the next future.

Table 5.1: Boundaries for the geometrical parameters.

Optimization	Constant [μm]	Variables	Bounds lower [μm]	Bounds upper [μm]
1	$p \equiv 900$	d	45	300
		w	45	300
2	$d \equiv 105$	w	100	300
		p	400	1670
3	$d \equiv 255$	w	100	300
		p	400	1670
4-6		d	30	300
		w	10	300
		p	400	1670
Reference	$d \equiv 255$			
	$w \equiv 200$			
	$p \equiv 900$			

5.2.3 Fitness Function

The fitness function to be minimized by the optimization engine is described by Equation 5.1. This comprises an optimization objective and a constraint, expressed by the penalty function.

$$fitness = -\frac{o}{o_{ref}} + \alpha \cdot \underbrace{\frac{1}{1 + \exp\left(-\gamma \cdot \left(\frac{E_{max}}{E_{ref}} - 1\right)\right)}}_{Penalty\,function} \tag{5.1}$$

where o is the optimization objective
o_{ref} is the respective value from the reference AFC
α is a weighting factor for the penalty function
γ is the steepness-factor of the penalty function
E_{max} is the maximum E-field in the fiber
E_{ref} is the respective value from the reference AFC

Three different target values of the RVE are investigated:

- Strain S
- Generated force per cross-sectional area σ
- Capacitance-density C_d

The maximum target value, obtained without or only slightly offending the electrical field constraint, will correspond to the minimum value of the respective fitness function. Based on previous experience, α and γ in the fitness function (Equation 5.1) are set to 3 and 60, respectively. The population size is set to 20 individuals.

5.3 Results

5.3.1 Strain

Constant Electrode Spacing

In a first optimization, the developed free-strain is investigated as a function of the fiber diameter d and the electrode width w, both in the range 45-300μm, whereas the electrode spacing is held constant at 900μm. Only results for configurations not exceeding the constraint of 30 kV/cm in electrical field are presented in Figure 5.2. Blue dots represent configurations evaluated numerically after selection by the optimization engine, the color-scaled surface is interpolated through the blue dots. Best performance in terms of the developed free-strain is found for $d = 90\mu m$ and $w = 48\mu m$ with a value of 2020$\mu\epsilon$. This is 11.6% more than the value predicted and measured for the reference AFC (1810$\mu\epsilon$). With this best set for d and w,

the resulting E_{max} is 28.2kV/cm compared to 28.7kV/cm for the reference AFC.

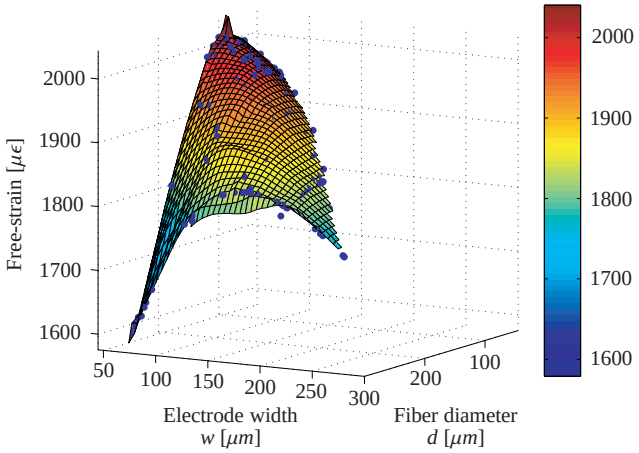

Figure 5.2: Resulting strain against d and w for $p = 900\mu m$.

Constant Fiber Diameter

A second investigation focuses on two commercially available fiber diameters. Combinations of electrode spacing p and width w are evaluated for $d = 105\mu m$ and $d = 255\mu m$, respectively. Again, only results for configurations not exceeding the constraint of 30 kV/cm in electrical field are considered.

Results for $d = 105\mu m$ are discussed first. Not surprisingly, the larger the electrode spacing, the higher is the resulting average strain. Defining the bounds for p and w imposed by the current electrode manufacturing technology, highest free-strain ($2050\mu\epsilon$) is achieved for nearly maximum electrode spacing $p = 1630\mu m$ and an electrode width $w = 103\mu m$, close to the lower bound. This is 13.3% more than the value predicted and mea-

sured for the reference AFC (1810$\mu\epsilon$); E_{max} is 30.5kV/cm. Results are depicted in Figure 5.3.

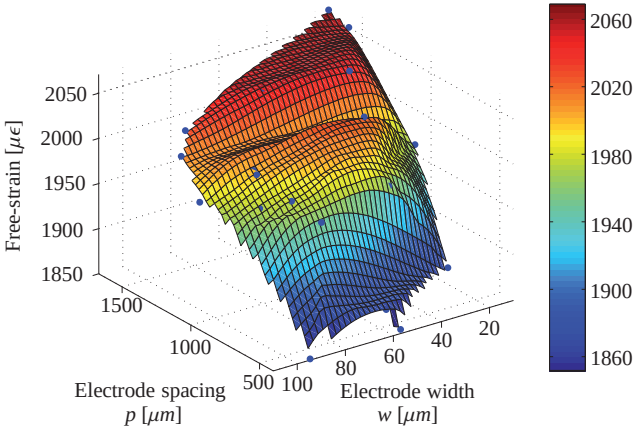

Figure 5.3: Resulting strain against p and w for $d = 105\mu m$.

Similar results were obtained for $d = 255\mu m$. Slightly lower maximum free-strain (2010$\mu\epsilon$) is achieved for nearly maximum electrode spacing $p = 1660\mu m$ and an electrode width $w = 150\mu m$. This is 11.0% more than the value predicted and measured for the reference AFC (1810$\mu\epsilon$); E_{max} amounts to 27.6kV/cm. Results are depicted in Figure 5.4.

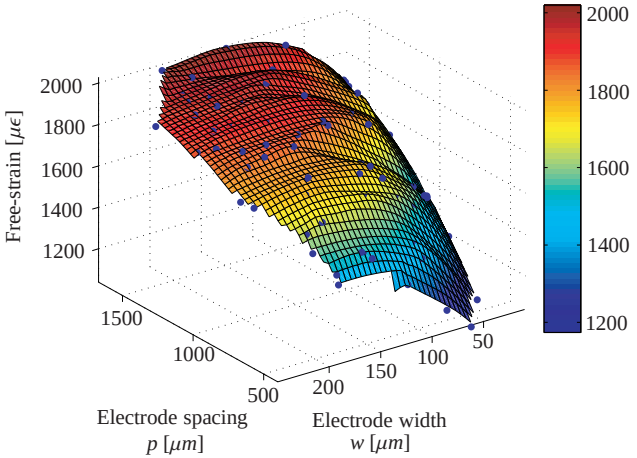

Figure 5.4: Resulting strain against p and w for $d = 255\mu m$.

Simultaneous Optimization of *p*, *d* and *w*

The simultaneous optimization of electrode spacing p, fiber diameter d and electrode width w yielded a slight increase in predicted free-strain compared to the previous optimizations. By allowing narrower electrodes (which would require photolithography or equivalent technologies for manufacturing) its value is increased by roughly 14.9% compared to the reference AFC ($2080\mu\epsilon$ vs. $1810\mu\epsilon$). The optimization engine identified a best set composed of an electrode spacing $p = 1670\mu m$, an electrode width $w = 45\mu m$ and a fiber diameter $d = 120\mu m$. Such a fiber diameter is not commercially available, but could easily be manufactured using dies with according orifices, as described in Chapter 3.1. With E_{max}=28.0kV/cm, the narrower electrodes don't generate higher electrical field concentrations compared to the reference AFC.

Table 5.2: Optimization results (bold numbers were defined as constant).

	d [μm]	p [μm]	w [μm]	E_{max} [kV/cm]	Strain S [$\mu\epsilon$]	Δ [%]
Reference	**255**	**900**	**200**	28.7	1810	
$d-w$	90	**900**	48	28.2	2020	11.6
$p-w$	**105**	1630	103	30.5	2050	13.3
$p-w$	**255**	1658	150	27.6	2010	11.0
$p-d-w$	120	1670	45	28.0	2080	14.9

	d [μm]	p [μm]	w [μm]	E_{max} [kV/cm]	Stress σ [$10^6 Pa$]	Δ [%]
Reference	**255**	**900**	**200**	32.2	32.7	
$p-d-w$	300	1640	246	32.4	34.8	6.4

	d [μm]	p [μm]	w [μm]	E_{max} [kV/cm]	C_d [F/m^3]	Δ [%]
Reference	**255**	**900**	**200**	32.2	0.0266	
$p-d-w$	293	400	192	32.4	0.1432	438

5.3.2 Generated Force per Cross-sectional Area

The investigation of the clamped model yielded largest generated stress for largest fiber diameter d and electrode spacing p. The optimization engine identified a best electrode width $w = 246\mu m$. The present findings are in line with results reported by Bent and Pizzochero [47]. With the optimized parameters, the stress, respectively the blocking force could be increased by 6.4% compared to the reference AFC.

5.3.3 Capacitance

The largest improvement in target value could be achieved for the capacitance optimization. The total capacitance of the AFC module is a result of the capacitance of the RVE and of the parallel and serial alignment of

the RVEs within the AFC module. The RVE volume, on the other hand, directly depends on the fiber diameter and the electrode spacing. It makes therefore sense to compare results in terms of capacitance per volume. Not surprisingly, the optimization engine selected a fiber diameter close to the upper bound ($d = 293\mu m$) and minimum electrode spacing ($p = 400\mu m$). With $w = 192\mu m$, the optimum electrode width remained virtually unchanged compared to the reference AFC. According to these findings, the capacitance of the AFC module with equivalent volume could be increased by 438% from 0.90 nF to 4.82 nF.

All optimization results are summarized in Table 5.2.

5.4 Conclusions

The AFC response is decisively influenced by the electrode width w, the electrode spacing p, as well as the fiber diameter d. Based on previously developed parametric FE models (see Chapter 4), the influence of all three parameters was simultaneously investigated using evolutionary algorithms. Best configurations were found for largest free-strain, maximum generated force per cross-sectional area and largest capacitance density, respectively. Free-strain could be enhanced by 14.9%, stress by 6.4% and capacitance by 438% compared to the reference AFC.

As documented in Chapter 8, this represents only marginal improvements considering the requirements imposed to active components for use in structural vibration control.

Part III

Integration of Active Modules into Smart Parts

Chapter 6

Inkjet Printing of Palladium Catalyst Patterns on Polyimide Film for Electroless Copper Plating

The work presented in this Chapter can be found with minor modifications as a publication in the scientific literature as:

S. Busato, A. Belloli and P. Ermanni. Inkjet printing of palladium catalyst patterns on polyimide film for electroless copper plating. *Sensors and Actuators B*, 123(1):840-846, 2007.

A convenient method has been developed that provides for applying patterned copper tracks on flexible polyimide film for electronic applications. The workflow comprises inkjet printing of an aqueous palladium(II) solution onto surface treated polyimide film, followed by reduction to metallic palladium and electroless copper plating. All processing steps involved require minimal infrastructure and result in metallic feature dimensions down to 100μm using a desktop inkjet printer. Ink stability is documented by UV/vis, and copper line dimensions and electrical resistivity are examined as function of design dimensions and electroless plating time. The procedure was successfully applied for manufacturing interdigitated electrode films as used in Active Fiber Composites.

6.1 Introduction

Since the advent of inkjet printing for typeset and graphic arts applications, the technology's potential for the patterned deposition of virtually any type of liquid material, including polymer solutions and molten metals [100], has been recognized. In particular, significant research efforts have been directed towards printing low-cost, large-area electronic circuits on flexible substrates by additive inkjet patterning [101]. When printing electronic devices such as transistors or organic light emitting diodes based on organic (semi-)conductors, the typical resolution limit of inkjet printers (50–100μm) imposes a limit to its direct printing capabilities. Printing of sub-hundred-nanometer features has been demonstrated, however, with indirect printing techniques by either lithographically pre-patterning the substrate into regions of different surface energy [102, 103] or by the self-aligning drying behavior of printed droplets overlapping two regions of different surface energy [104]. On the other hand, there exists a range of electronic applications with lower requirements in terms of spatial resolution that can easily be met with direct inkjet printing. Flexible printed circuitry (FPC) as used in radio frequency tags or connections of modular electronic subassemblies is conventionally prepared by photolithographical patterning and subsequent etching of a metal clad polymer film with a final metal track width down to 0.1mm. Direct inkjet printing of such cir-

cuitry has been reported by several authors. Printing of concentrated non-aqueous gold or silver nanoparticle colloids followed by low-temperature sintering [105] or laser curing [106] resulted in features with resistivities in proximity of the corresponding bulk metals, avoiding the extreme conditions required for liquid metal printing. Similarly, printing of the chemical vapor deposition precursor vinyltrimethylsilane copper(I) hexafluoroacetylacetonate [107] followed by disproportionation at elevated temperatures yielded conducting copper patterns. A different approach relies on printing weakly concentrated aqueous catalyst ink followed by a post-processing step aimed at increasing the metal loading and electric conductivity of the initiator tracks. Typically, this approach is based on general chemistry as used in the metal plating of polymers [108], e.g. in the electroless copper plating of fiber reinforced epoxy sheets in the manufacture of printed circuit boards. Colloidal platinum inkjet printed onto Nafion and coated or surface treated poly(ethylene terephtalate) films yielded well-defined features down to 100μm after electroless copper plating [109]. Silver nanocolloids were equally printed with good resolution onto paper and inkjet transparencies [110], but not metal-plated (silver, however, does catalyze copper deposition from appropriate plating solutions [111]). Critical issues with colloids reside in the sedimentation stability of the corresponding sols, typically requiring stabilizers and limiting the metal concentration to low values, and in the associated risk of metal encapsulation reducing catalytic activity for the electroless plating process. This paper describes a convenient, inexpensive and reproducible laboratory method for the patterning of copper features on commercial polyimide film. Inkjet printing of a palladium(II) solution followed by chemical reduction and electroless copper plating results in feature dimensions down to 100μm.

6.2 Experimental

6.2.1 Ink Preparation

Palladium(II) chloride (40mg, Riedel-de Haen) and ammonium chloride (40mg) were stirred in 23.75g water for ca. 1 h until a clear yellow solution was obtained. Three drops (ca. 0.15ml) 30% hydrogen peroxide were added, followed by 1.25g 2-propanol. The resulting ink containing ca. 1mg Pd/ml showed no precipitation over a period of more than 4 months when stored at 4°C. At room temperature visible precipitation of metallic palladium occurred within 2-3 weeks. Surface tension was measured with a Sinterface Profile Analysis Tensiometer PAT1, viscosity with a Paar Physica MCR300 Modular Compact Rheometer. UV/vis measurements on dilute inks containing 0.5mg Pd/ml (20mg $PdCl_2$ and 20mg NH_4Cl in same amounts of liquids as above) were performed with a UV/VIS/NIR Spectrometer Perkin-Elmer Lambda 900.

6.2.2 Surface Treatment of Polyimide Film

The palladium ink was printed onto polyimide (PI) film (Upilex-R: poly(biphenyl dianhydride-4,4′-oxydianiline), UBE Industries Ltd., Japan) of 25 and 75μm thickness, respectively. Two wet-chemical methods were employed for rendering as-received PI film hydrophilic and receptive for Pd(II) ions.

Method A

The film was oxidatively etched in a solution of potassium permanganate (60g/l) and sodium hydroxide (30g/l) at 80°C for up to 60 min, cleaned by sonication in water, immersed in 10M potassium hydroxide at room temperature for 2 h and finally rinsed with water and dried.

Method B

The film was immersed in 10M potassium hydroxide at room temperature for up to 72 h and finally rinsed with water and dried.

Best printing results (resolution, reproducibility) were obtained with method B and a treatment time of no less than 48 h. The surface topography of films was studied by scanning electron microscopy (SEM) using a LEO1530 SEM. The contact angle of water on PI films was determined with a Krüss G-1 Contact Angle Measuring Instrument.

6.2.3 Inkjet Patterning

Printing patterns were designed with Adobe Illustrator graphics software. Near-black patterns were drawn in Adobe RGB (1998) working color space with color values set to R = G = B = 10. A Hewlett Packard Deskjet 1220c printer (resolution 600x600 dpi; DIN A3 format) was used for printing using the black cartridge only ("HP45": full part number 51645G or 51645A); however, an empty tri-color cartridge ("HP78": full part number C6578D or C6578A) needed to remain installed for the printer to work properly. The foamless, spring-bag type black cartridge was emptied, rinsed with water and 5% ammonia to remove any residual original ink and finally filled with 15-30ml palladium ink. The printer driver (HP v2.0) was set to plain paper mode with the following settings: print quality best, paper type plain paper, image enhancement on, convert to grayscale off, all other settings left to default. Print color space was identical to working color space. The surface treated PI film was affixed to a supporting sheet of plain paper using Repositionable Adhesive Spray (3M ReMount) and carefully fed through the printer. The print-out was allowed to dry at ambient conditions until no more liquid ink was visible and finally baked at 60°C for 15 min. Reduction of the surface-bound palladium(II) to metallic palladium was accomplished by immersion into 0.1M sodium borohydride at room temperature for 5 min and final water rinse. After reduction, the printing pattern was just about discernible to the naked eye.

6.2.4 Electroless Copper Plating

A plating solution (adapted from [109]) was freshly prepared by dissolving sodium hydroxide (3.5g/100ml), ethylenediamine tetraacetic acid (5.1g/100ml) and copper sulfate pentahydrate (2.5g/100ml) in water, adding

aqueous 36% formaldehyde (0.4ml/100ml) and finally adjusting the pH to 12.4-12.5 by dropwise addition of concentrated sulfuric acid. Inkjet patterned PI films were immersed at 25°C for up to 60 min (typically 20 min), resulting in selective copper deposition on the printed patterns. Shiny copper lines appeared almost black when observed from the reverse side through the transparent PI film. Plating was accompanied by visible gas evolution and - for the case of extended plating duration - by occasional blister formation on the copper tracks. Average line width was determined as the ratio of surface area to length (measured with optical microscopy) on $2500\mu m$ long sections. Average line thickness was determined by measuring the surface profile with a Tencor P10 Surface Profiler at a minimum of three locations for each sample. Resistivity was measured using a 4-point method with an in-house built test fixture and a Keithley 237 High Voltage Source Measure Unit.

6.3 Results

6.3.1 Palladium Ink

An inkjet printable solution containing palladium ions was prepared by first stirring palladium chloride and ammonium chloride in water. The surface tension of this solution was virtually identical to water (72.8mN/m) and needed to be adjusted to match the value of the original ink for the printer to be used in order to attain similar jetting behavior. Surface tension reduction was accomplished by addition of a cosolvent, avoiding the use of non-volatile surfactants and their potential risk of inhibiting palladium adhesion to the printing substrate. Considering 2-propanol for the purpose, we realized that this solvent effectively reduces palladium(II) resulting in quick precipitation of the metal. In reminiscence of a common practice for revitalizing aged sensitizer solution in the art of the photographic palladiotype process [112], we found that adding a small amount of hydrogen peroxide to the solution prior to 2-propanol addition effectively stabilizes the solution against precipitation. Thus, adding three drops (ca. 0.15ml) of 30% hydrogen peroxide for 25g of final ink and 2-propanol to amount to

5% (w/w) did reduce the surface tension to 49.3mN/m, closely matching the value of the black ink of a "HP45" cartridge (47.1mN/m). The yellow clear ink had a palladium content of ca. 1mg/ml and did not precipitate over more than 4 months (maximum observation time) when stored at 4 °C. At room temperature precipitation set in after 2-3 weeks. The significantly lower viscosity ($<1 mPa \cdot s$) as compared to the "HP45" ink ($3.35 mPa \cdot s$) was not deemed critical for printing. UV/vis measurements (Figure 6.1) were taken on two ink formulations containing 0.5mg Pd/ml, one prepared as described above and one purely aqueous reference in which 2-propanol had been replaced by the equivalent amount of water.

Five minutes after preparation both samples exhibited an absorption maximum at 422nm attributable to the d-d transition of the $PdCl_2(H_2O)_2$ complex [113]. After 14 days at room temperature the maximum absorption of both solutions had shifted to 410nm at slightly reduced absorptivity, indicating hydration to $[PdCl(H_2O)_3]^+$. Thereafter, the aqueous reference remained virtually unchanged in both spectral and physical appearance up to 105 days, whereas gradual precipitation set in in the alcoholic sample. Spectra of the latter's supernatant liquid after 54 and 105 days showed a shift back towards longer wavelengths at lower absorption values. Presumably the reduced palladium ion content and concomitant increased relative chloride concentration led to anation of the monochloro back to the original dichloro complex.

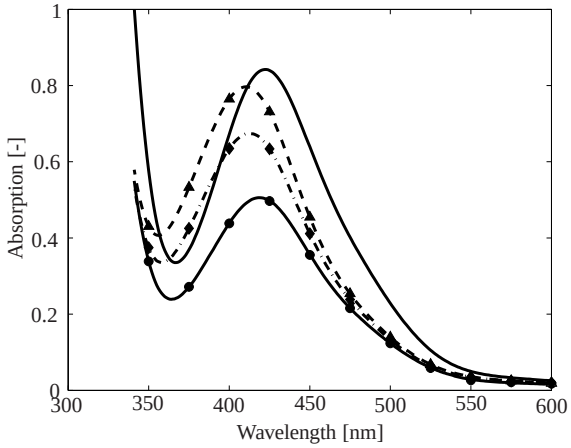

(a)

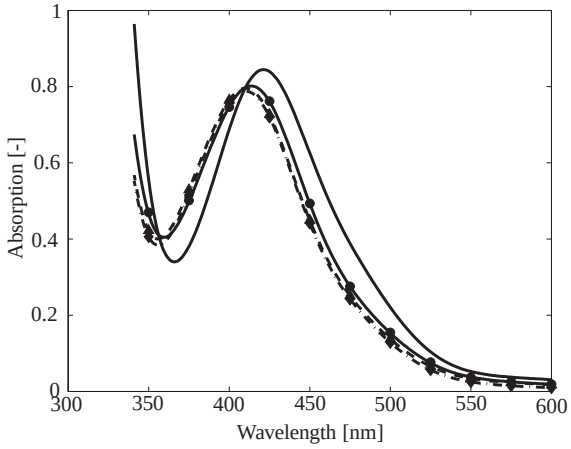

(b)

Figure 6.1: UV/vis-spectra of dilute palladium(II) solutions (0.5mg Pd/ml) after storage at room temperature: (a) in 5% aqueous 2-propanol stabilized with hydrogen peroxide; (b) in water; after 5 min (–), 14 days (▲), 54 days (♦), and 105 days (●).

6.3.2 Wet-chemical Treatment

In order to render the hydrophobic polyimide film wettable by the aqueous palladium ink, two wet-chemical methods for surface treatment were examined. Method A (adapted from [114]) comprised two steps, namely oxidative surface micro roughening by immersion in alkaline potassium permanganate solution at 80°C for up to 60 min, followed by chemical imide ring opening by exposing the pretreated film to 10M potassium hydroxide at room temperature for 2 h. Method B (adapted from [115]) consisted of the chemical imide ring opening only by immersion into 10M potassium hydroxide at room temperature for up to 72 h. SEM pictures of samples after both surface treatments are shown in Figure 6.2.

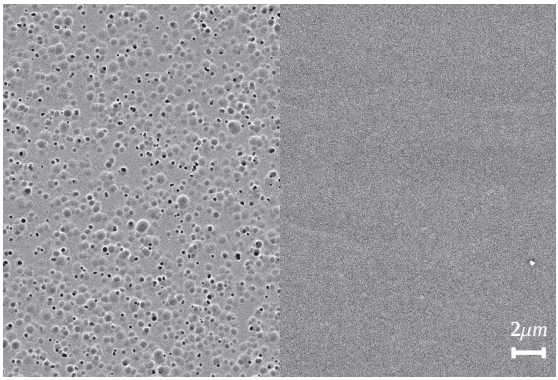

Figure 6.2: SEM pictures of polyimide films after surface treatment in $KMnO_4$–$NaOH/KOH$ (left) and KOH (right), respectively.

Method A resulted in the formation of a large number of recesses on the film surface, confirming the findings of Wang et al. [114]. The number and dimensions of recesses generally increased with the permanganate treatment time, reaching up to $1\mu m$ in diameter after 30 min. By contrast, no topographical features were observed for films treated according to method B.

Gravimetrical monitoring of the films during treatment showed a nearly linear weight loss with time up to ca. 8.2% after 60 min for method A and a nearly linear weight gain up to ca. 1.7% after 48 h for method B, respectively. The weight loss (method A) is attributed to the oxidative removal of material from the surface. On the other hand, imide ring opening (method B) results in the formation of both carboxylic acid and potassium carboxylate groups for the present case of final water rinse [115] (rinsing with hydrochloric acid would leave only carboxylic acid groups, whereas rinsing with 2-propanol would leave potassium carboxylate) and entails the uptake of one equivalent water or potassium hydroxide, respectively, for every imide ring cleaved, explaining weight gain. Measurements of the advancing contact angle of water drops on the treated film turned out to be poorly reproducible with values of 66-74° for untreated film and 21-52° for treated film. In addition, water drops on PI films treated according to method A displayed a distinct tendency to spread and grow in contact area, a phenomenon comparable to the "bleeding" of writing ink on filter paper caused by capillary forces. Spreading of drops was not observed on smooth films treated according to method B.

6.3.3 Printing and Electroless Copper Plating

Printing experiments on PI films of up to DIN A3 size (297 by 420mm) were conducted with an older HP Deskjet 1220c desktop printer, chosen mainly for the ease of refilling the corresponding foamless black cartridge. This hardware with a printhead containing 304 nozzles (diameter 28μm) allowed rapid printing of large areas. The limited control over number and size of drops available through the few adjustable parameters in the printer driver was sufficient for the present application. Adjusting the red, green and blue color values of patterns drawn in the chosen working color space (Adobe RGB (1998)) allowed additional control over the amount of ink jetted. After printing and drying of the palladium(II) ink no pattern was visible to the naked eye. Short immersion of the print-out in 0.1M sodium borohydride revealed a faint grayish deposit of metallic palladium where the ink had been jetted by the printer. Electroless copper plating at room temperature resulted in copper lines appearing within a few minutes.

Figure 6.3 shows samples of copper lines for both polyimide surface modifications described above under otherwise identical conditions (design line width 150μm, copper plating time 20 min).

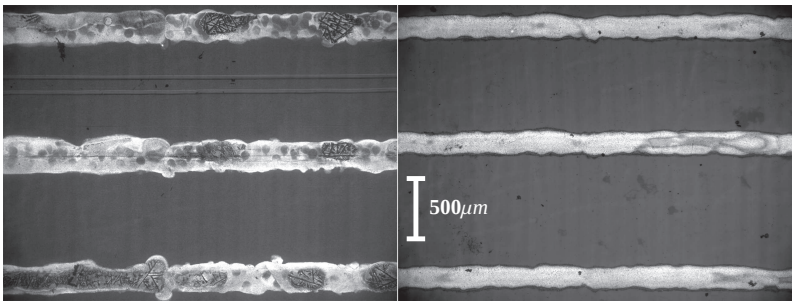

Figure 6.3: Sample copper lines printed on polyimide film after surface treatment in $KMnO_4$–$NaOH$/KOH(left) and KOH(right), respectively (design line width 150μm).

On a microscopic scale, in both cases the lines do not exhibit straight boundaries, reflecting the characteristic array of overlapping dots of inkjet droplets impacting on a surface. However, for the case of oxidative etching (method A) blurred lines were observed even on a macroscopic scale. On the other hand, hydrolytic treatment (method B) for no less than 48 h delivered crisp and reproducible features, making this the method of choice. The two-stage etching procedure (method A) had been shown [114] to increase the peel strength of electroless copper on polyimide by a factor of more than five over simple hydrolytic surface treatment (method B). In qualitative tests, we found both surface treatments to yield highly scratch resistant (fingernail) copper features that could not be peeled off with applied adhesive tape (Flashbreaker, Airtech). With the plating bath composition used, plating was accompanied by visible gas evolution and - for extended plating duration - by occasional blister formation on the deposited tracks. Presumably, hydrogen gas was being generated by recombination of adsorbed atomic hydrogen stemming from the initial formaldehyde de-

hydrogenation step [116]. The rate of copper deposition was strongly pH dependent with lower pH slowing the reaction down. Good results were obtained with the pH in the range 12.4-12.5 and a plating time of 20 min at 25°C. Generally, larger features required shorter plating time than fine lines.

Measured line width and thickness as function of plating time are depicted in Figures 6.4 and 6.5, respectively.

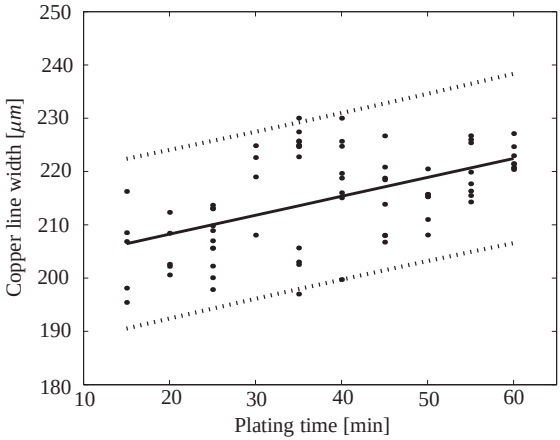

Figure 6.4: Actual copper line width as a function of electroless plating time (design line width 150μm): measured values (●), linear fit (—), and 95% prediction bounds (· · ·).

Average line width gradually increased from 206.5μm after 15 min to 222.4μm after 60 min for a design line width of 150μm, with a standard deviation of less than 5%. Plated copper thickness increased at a rate of approx. $1\mu m/h$ with measurable conductivity attained after approx. 15 min. Electrical resistance of 40mm long line sections (Figure 6.6) showed power decay with plating time, in agreement with the observed linear copper thickness development. The corresponding specific conductivities remained nearly constant at $(2.5-3)\times 10^7\, S\, m^{-1}$, representing approximately

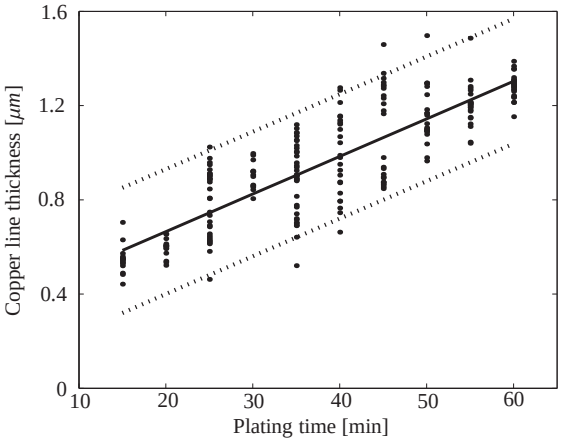

Figure 6.5: Copper line thickness as a function of electroless plating time: measured values (●), linear fit (—), and 95% prediction bounds (· · ·).

half the value of bulk copper ($5.95 \times 10^7 S\,m^{-1}$). Actual width of copper plated lines (20 min plating time) as function of design line width (Figure 6.7) lay within acceptable agreement, but prior experimental calibration was required for improved anticipation of final feature dimensions. Particularly at the lower end the observed overshoot of up to $50\mu m$ represented a significant deviation from design dimensions. The thinnest practicable and reproducibly conducting line had a width of some $130\mu m$. On single occasions, conducting lines down to $100\mu m$ could be produced. This value can be expected to be lowered by printing through smaller print nozzles, reduced ink surface tension and corresponding smaller drop volume. Nozzle diameter of typical color print heads is around $15\mu m$ for an ink surface tension of ca. 30mN/m. Modification of the present palladium ink to this value was accomplished by increasing the 2-propanol content to 20% (w/w) without incurring a reduction in precipitation stability. However, we refrained from making use of the printer's "HP78" color cartridge due to its foam based construction, making it cumbersome to handle and also

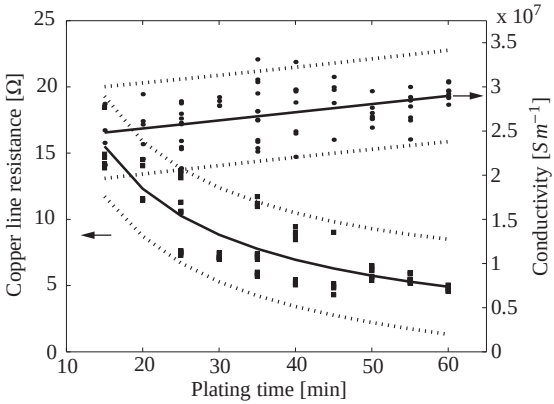

Figure 6.6: Electrical resistance of copper lines (40mm long, approximately 200μm wide) as a function of electroless plating time (left axis): measured values (■), linear fit (—), and 95% prediction bounds ($\cdots$). Corresponding specific electrical conductivity (right axis): measured values (●), linear fit (—), and 95% prediction bounds ($\cdots$).

significantly accelerating palladium precipitation. We adopted the present method for manufacturing flexible interdigitated electrode films, key components of the Active Fiber Composites used in Chapter 10. The reject rate of the geometrically complex electrodes – consisting of a multitude of individual lines – was reduced by choosing an uncritical target line width of 200μm. The electroless copper plated prints were additionally electroplated in order to further reduce track resistance (electroplating bath containing 200g/l copper sulfate pentahydrate and 100g/l concentrated sulfuric acid, galvanostatic conditions at ca. $10 mA/cm^2$) and subsequently elaborated by sandwiching a layer of unidirectional piezoceramic fibers between two aligned electrode films and impregnating the arrangement with epoxy resin.

Figure 6.8 shows one electrode film and the final AFC patch that was

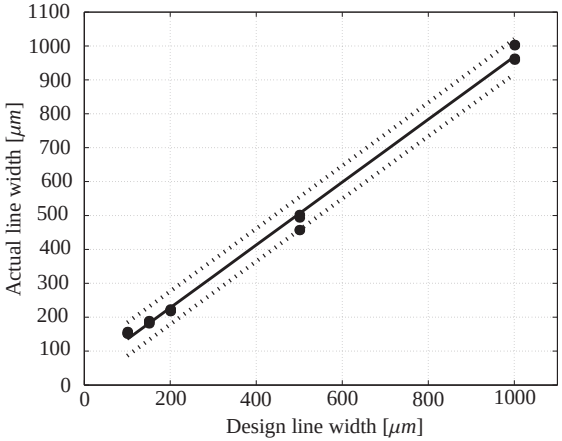

Figure 6.7: Actual copper line width obtained for given design line width: measured values (●), linear fit (—), and 95% prediction bounds (· · ·).

successfully poled and operated at voltages up to 2.4kV.

6.4 Conclusions

Hydrogen peroxide effectively stabilized a palladium(II) solution in water/2-propanol against premature precipitation, allowing inkjet printing onto potassium hydroxide treated polyimide film. After reduction with sodium borohydride the formed metallic palladium patterns were subjected to electroless copper plating yielding flexible printed circuitry with feature dimensions down to 100μm and good copper adhesion. The simple procedure and solution chemistry involved – devoid of the issues typically associated with colloidal suspension preparation and stability – combined with inexpensive printing hardware and data driven patterning, make for a convenient laboratory method for prototyping large area circuitry with moderate resolution on electrically and thermally stable polyimide. The technique was used for

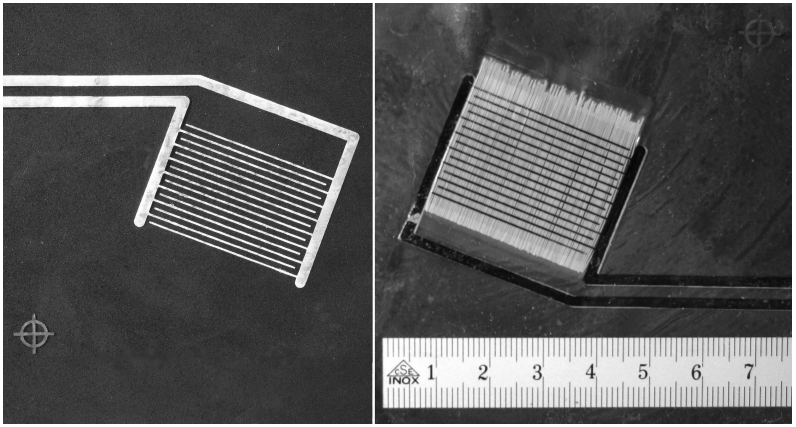

Figure 6.8: Interdigitated electrode film after final electroplating (left). Laminated active fiber composite patch (right). Unidirectional piezoceramic fibers are aligned perpendicularly to the interdigitated electrodes. Copper lines in the patch appear black when seen from the reverse side through the transparent PI film.

manufacturing all electrode films then laminated to monolithic and AFC active modules, components of the test object described in Chapter 10.

Chapter 7

Reliability Characterization of Smart Composite Laminates with AFC Inclusions

The work presented in this Chapter has been submitted with minor modifications as a paper to Composites Science and Technology:

M. Melnykowycz, A. Belloli, R. Paradies and P. Ermanni. Reliability Characterization of Smart Composite Laminates with AFC Inclusions. *Composites Science and Technology*, submitted January 2009.[1]

[1]The first and second authors contributed in equal manner to the scientific results and to the redaction of this article. The first author explicitly consents the present chapter be included into this thesis.

The current Chapter explores smart materials integration into composite materials using experimental and numerical methods to characterize the mechanical integrity issues associated with smart materials integration. Active Fiber Composite (AFC) devices and Dummy AFC (DAFC) were integrated into woven Glass (GFRP) and cross-ply Carbon Fiber Reinforced Plastic (CFRP) laminates and tested to determine the effect of integration on the laminate tensile properties. Different integration procedures including cutout, insertion, and interlacing have been considered. Experimental activities have been supported by numerical modeling of the integration configurations using ANSYS. Tsai-Wu Strength Index (TWSI) values were plotted and correlated with experimentally observed fracture patterns. Results show that mechanical integrity decreases as elements are integrated away from the midplane of CFRP and GFRP laminates. The use of CFRP cross-ply composites reduces the impact of device integration on mechanical property degradation. Actuation ability was assessed using a custom ANSYS shell element with piezoelectric capabilities. It was found that actuation ability increases as actuators are placed near the laminate surface, which imposes the largest penalty on mechanical integrity.

7.1 Introduction

Smart materials can be designed for specific sensor and actuator applications including structural health monitoring, shape control, and vibration damping and therefore have received a great deal of attention in the research community. Lead Zirconate Titanate (PZT) based materials are commonly employed as the active element in many smart materials systems due to their actuation and sensing abilities, which include the generation of high forces coupled with a fast signal response time. PZT devices are commonly manufactured as wafers, stacks, Active Fiber Composites (AFC) [12] with circular cross section fibers, and Macro Fiber Composites (MFC) [117] with rectangular cross section fibers.

Smart or adaptive material systems based on PZT elements in either wafer or fiber form are currently employed in smart skies and snowboards [118, 119], tennis racquets [120], automotive vibration sensors, flat panel

speakers [121] as well as active rotor blade [31] applications. Often polymer or fibre reinforced polymer-based materials - such as laminated composites made of Glass (GFRP) or Carbon Fiber Reinforced Plastic (CFRP) - are used in the structural design. Polymer composites are good host structure candidates in smart materials design due to their layer-wise configuration, the easy integration of sensors and actuators and the conformability during the manufacturing process.

The development of truly smart structures eventually requires the direct integration of sensors and actuators into passive structural host materials. Ideally a smart material should simultaneously serve as a structural and active component. Currently, however, smart structures are often composed of two distinctly dissimilar materials, the structural and active components. Creating material systems of two dissimilar materials invariably will lead to problems with structural integrity that need to be addressed. Few studies have addressed the integrity and performance parameters of AFC or PZT wafer devices as a component in a smart structure and the synergy between the active element and the surrounding host structure. The integration of smart devices is expected to have an effect on the mechanical performance and integrity of a structure. In particular, degradation of the strength properties is a great concern. This is of particular relevance to critical applications such as rotor blades or airplane wings where efficient structural designs with high strength to weight ratios and maximum integrity are required.

7.1.1 Integration Techniques and their Impact on the Laminate Properties

Integration may be defined as any technique used for embedding an active element into a structure or material. In a laminated composite the two basic integration techniques are "insertion" and "cutout insertion" or "embedding" (Figure 7.1). Insertion entails simply placing the device between the laminate layers, essentially sandwiching it in place. Embedding or cutout insertion involves removing laminate material, and then placing the device into the void so that the device becomes continuous with the

surrounding structure or material. Combining the two techniques leads to "interlacing". The interlacing technique involves distributing the cutout integration region through the thickness of the laminate.

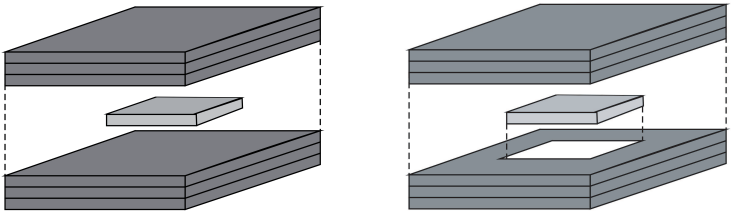

(a) (b)

Figure 7.1: Integration techniques. (a) Insertion (b) Cutout.

Past studies on smart materials integration have focused on the center or symmetric integration of PZT wafer devices in composite laminates under uniaxial loading with the active element integrated in the 0° or 90° plies. Crawley and De Luis [122] investigated the integration of PZT wafer actuators into woven composites using analytical and experimental methods and proposed design criteria for PZT actuators such as a high Young's modulus to allow stress transfer with the surrounding laminate. In static tension, the integration of PZT devices via cutout integration was found to have little effect on the Young's modulus, but a 20% decrease in the ultimate tensile strength of the integrated GFRP laminates was observed. Mall and Coleman [123] investigated the effect of PZT wafer integration on CFRP laminates under monotonic tensile and fatigue conditions and reported that with quasi-isotropic CFRP lay-ups the integration technique does not greatly affect laminate strength, reporting a difference of only 4% between the mechanical properties of composite laminates without integrated devices and those that employed the insertion and cutout integration techniques with PZT elements integrated in or adjacent to the 90° low load-bearing plies. Paget and Levin [124] performed similar work with

PZT wafers inserted in the center of CFRP laminates and only saw a 3% difference in the ultimate tensile properties between laminates with integrated PZT wafers and the reference laminates. Interlacing the laminate plies and distributing the integration region throughout the laminate thickness has been found to improve laminate integrity with integrated elements. Shingh and Vizzini determined an optimal interlacing configuration using numerical methods [125]. In a second study, Shukla and Vizzini [126] evaluated the optimum design by tensile testing of UD GFRP laminates with integrated glass slides to simulate the presence of active elements. It was reported that increasing the taper length improves load transfer but also increases the resin rich zone at the integration region. Reducing the taper length improves failure at the device interface but also degrades laminate integrity [127].

Summarizing, in a symmetric [0,90] cross ply laminate composed of unidirectional (UD) material loaded in the 0° direction, device integration in the low load-bearing 90° plies will reduce the impact of integration on laminate integrity as compared with integrating the devices into the load bearing 0° plies. However, this design philosophy can not be adopted for multi-axial loading. The development of a tool which can easily assess the impact of different integration approaches on laminate integrity would be of benefit to engineers designing smart composite laminates.

7.1.2 Prediction of the Laminate Integrity

An understanding of the failure of smart laminates is needed to design structures that fulfill the functional as well as the structural mechanical design requirements of a given application. In particular, tools and methods for determining the effect of smart materials integration on laminate integrity can be used to better characterize the trade-off between adding actuation and sensing capabilities while influencing the mechanical integrity of the structural design. Many smart material applications require service life of sensors and actuators in fatigue and cyclic environments. Separately both PZT and composite materials have shown robustness over millions of fatigue cycles. A critical point with integrating the materials together into a system is the ability to characterize damage evolution due to the mis-

match of material properties and how this impacts the initiation of damage in the laminate system. Numerically characterizing laminate integrity can be accomplished by employing failure criterion predictions for different laminate configurations with integrated smart elements. A number of failure theories are available for composite laminate materials, and are generally characterized as limit, interactive, or partially interactive [128]. The World-Wide Failure Exercise [129, 130] was conducted to assess the effectiveness of various failure criteria for predicting the behavior of composite laminates. The Tsai-Wu quadratic failure criterion [131] was shown to perform well in predicting laminate response and ultimate failure [130]. The First Ply Failure (FPF) prediction is also available, and has been found to agree with experimental results. Limitations were found for post FPF and Last Ply Failure (LPF) values [132], however it has been found to be a robust tool for engineering with composite materials. Tsai-Wu is limited in that differentiation is not established for matrix versus fiber failure in a laminate. This distinction is covered in a partially interactive criterion such as Puck [133]. However, the easy implementation and performance of Tsai-Wu makes it an ideal choice for evaluating composite smart laminate integrity and is relatively easy to integrate into a finite element program such as ANSYS[2].

The current work focuses on the mechanical evaluation of smart device integration in GFRP and CFRP laminates via experimental and numerical methods, investigating the case where the ratio of passive to active plies is lower than in previous investigations. By using a higher percentage of active layers the impact of device integration is more pronounced. Woven GFRP laminates with integrated devices were used to investigate integration in the load-bearing plies of a laminate. Devices were integrated into the 90° plies of cross-ply CFRP laminates to study the effect on low load-bearing plies. The integration position through the thickness of laminates was also considered by placing devices in the midplane or near the laminate surface. Numerically, ANSYS modeling was employed to emphasize the impact of actuator and sensor integration on the structural integrity of the passive material in relation to the smart functionality (sensor and actuator

[2] www.ansys.com

ability) of the system as a whole.

7.2 Materials

GFRP laminates were produced using Isopreg HR 320P-40 plain weave pre-impregnated (pre-preg) composite plies supplied by Isovolta[3]. CFRP laminates were manufactured using ELITREX pre-preg CFRP composite plies (EHKF 420-UD24K-40) supplied by Stesalit[4]. AFC (nominal thickness of 330μm) were produced using 250μm diameter PZT-5A fibers supplied by Smart Material Corp.[5].

7.3 Methods

7.3.1 Laminate Manufacture

Orthotropic plain weave GFRP laminates composed of 8 (insertion integration) or 9 (cutout integration) plies were manufactured using a vacuum bagging and pressing process. Plies were prepared by cutting sections of the pre-preg strips to dimensions of 30 x 30 cm. Vacuum was applied via an external pump and the GFRP plates were cured for 30 minutes at 120°C. CFRP cross-ply laminates composed of 12 plies of UD pre-preg were manufactured with a $[0, 90]_{3S}$ configuration. CFRP plies were cut to exact dimensions using a computer controlled Zünd M-1600 cutter, which allowed precise dimensioning of the cutout area for integration of DAFC and AFC. Ply arrangement was performed by hand on an aluminum tooling plate and an aluminum frame was used to contain the plies. The CFRP laminates were processed in an autoclave at 120°C for 90 minutes. Following processing, the reference (containing no AFC/DAFC) and integrated (containing AFC/DAFC) laminate plates were prepared in accordance with ASTM Standard D 3039/D 3039M-00. The specimen geometry and dimensions are shown in Figure 7.2.

[3] www.isovolta.com
[4] www.stesalit.com
[5] www.smart-material.com

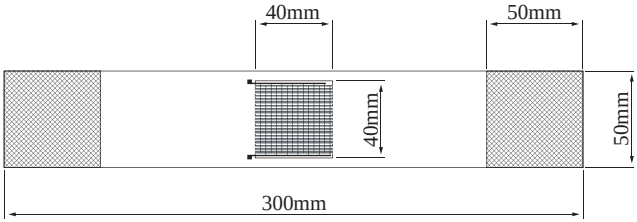

Figure 7.2: Schematic view of the laminate test specimens.

Aerolite epoxy glue was used to secure tab material to the ends of each specimen. Tensile testing was performed in accordance with ASTM Standard D 3039/D 3039M-00 using an Instron 1251 test machine with a 200kN load cell and an extensometer (50mm gage length) was used to determine strain during the test.

7.3.2 AFC/DAFC Manufacture

AFC (Figure 7.3) with dimensions of 33mm x 40mm and a nominal thickness of 0.33 mm were produced for integration into the composite laminates using a previously described method for AFC manufacture [134].

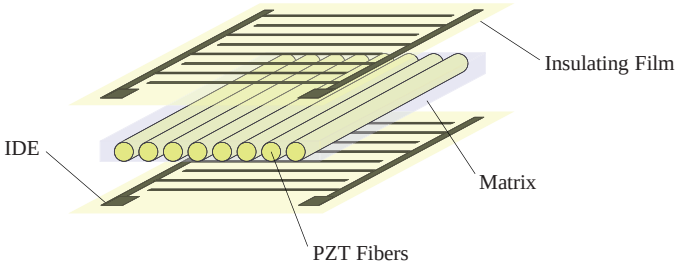

Figure 7.3: Schematic view of an Active Fiber Composite.

The DAFC (40mm x 40mm) were cut from a laminate of UD GFRP and Kapton®. Two UD GFRP plies were arranged at a +/- 20° orientation to one another to effectively match the measured longitudinal modulus of the AFC [134]. This GFRP core was sandwiched between sheets of Kapton® film and the DAFC laminate was processed in a press at 5 bar of pressure with a temperature of 120°C and maintained for 90 minutes.

7.3.3 Integration

The AFC/DAFC elements were integrated into the laminates using different integration techniques and placement positions with respect to the laminate thickness. The element position through the laminate thickness varied with respect to the midplane of the laminate. Three positions were defined: center, off center, and far off center.

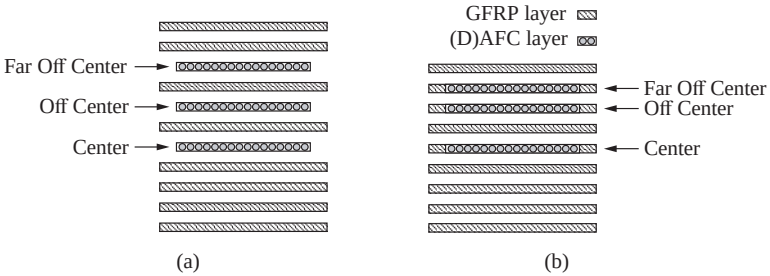

Figure 7.4: Position of the AFC/DAFC in the GFRP laminates. (a) Insertion integration procedure (8 ply laminate); (b) Cutout integration procedure (9 ply laminate). All ply angles are 0°.

This relative position was kept as constant as possible in the different materials systems even though the plies were of different thicknesses. DAFC were integrated into the woven GFRP laminates using the insertion and cutout methods (Figure 7.4) while DAFC integration in the cross-ply CFRP laminates was performed with the insertion and interlacing methods

(Figure 7.5). AFC were integrated into the GFRP laminates in the center and far off center positions using the cutout method while the AFC integration in the CFRP laminates included the inserted and interlaced methods in the far off center position. Table 7.1 summarizes the different combinations of laminate materials, integration methods, and placement positions that were tested. The symmetric configuration entailed two DAFC elements integrated using cutout (GFRP) and interlaced (CFRP) integration.

Table 7.1: Experimental programme.

Material	Integration		Device	Specimen #
GFRP	Cutout	Center	DAFC	5
			AFC	4
		Off Center	DAFC	5
		Far Off Center	DAFC	5
			AFC	4
		Symmetric	DAFC	5
	Insertion	Center	DAFC	5
		Off Center	DAFC	5
		Far Off Center	DAFC	5
CFRP	Insertion	Center	DAFC	5
		Off Center	DAFC	5
		Far Off Center	DAFC	5
			AFC	5
	Interlaced	Center	DAFC	5
		Off Center	DAFC	5
		Far Off Center	DAFC	5
			AFC	5
		Symmetric	DAFC	5

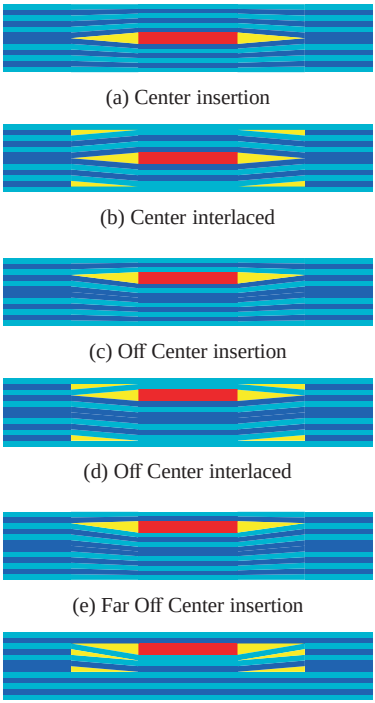

(a) Center insertion

(b) Center interlaced

(c) Off Center insertion

(d) Off Center interlaced

(e) Far Off Center insertion

(f) Far Off Center interlaced

Figure 7.5: Integration configurations for inserted and interlaced CFRP laminates. 0° plies in light, 90° plies in dark color.

7.4 Finite Element Model

The laminate geometry and different integration methods were modeled in ANSYS to assess their mechanical integrity and actuation capabilies. The layered SHELL99 element was employed, which allowed each ply angle to be easily defined. The influence of ply compaction on the ply mechanical properties was taken into account. To assess mechanical integrity, Tsai-Wu Strength Index (TWSI) values (Last Ply Failure) were computed by imposing the failure loads recorded experimentally. Experimental results and TWSI values were compared for validation of the model. FPF loads (i.e. TWSI equal 1 for any ply) were then determined for the different laminate configurations. To assess the sensing and actuation capability of the different configurations, a custom shell element with piezoelectric capabilities [135] was used to model the AFC modules. The laminate model was cantilevered at one end and actuated. Strain energy and tip deflection at the free end of the laminate were the quantities related to the different configurations. Additionally, the sensor performance could be assessed by imposing a deflection boundary condition and calculating the sensor voltage signal, proportional to the strain experienced by the piezoelectric module in the integration region.

7.5 Results and Discussion

7.5.1 Tensile Test Results

The failure load results from the GFRP laminates are graphically represented in Figure 7.6 while the CFRP laminate results are shown in Figure 7.7. These experimental results are also presented in Table 7.2 and Table 7.3 at the end of this Chapter.

As can be seen in Figure 7.6 the maximum force of the GFRP laminates decreased with the integration of DAFC in the laminate (center placement) and decreased further as the DAFC were placed far from the laminate midplane. Center placement decreased the maximum force value by about 6-9% while the off center and far off center placements showed a drop in

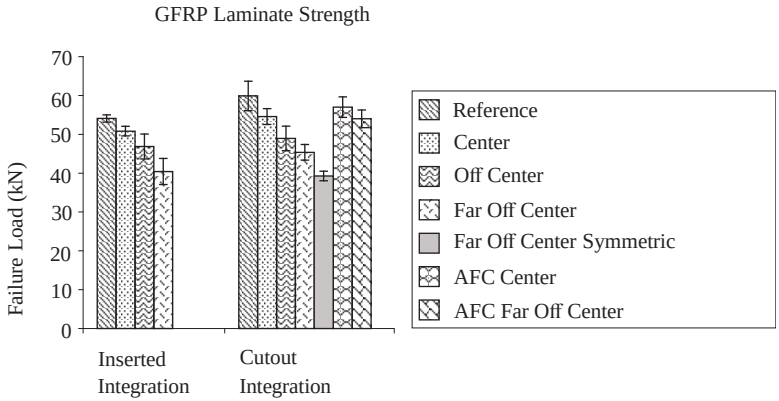

Figure 7.6: Failure load of the GFRP laminates.

strength of 13-18% and 24-25% respectively. Although a quantifiable difference is seen between cutout and insertion integration, considering the standard deviation of approx. 2-4% both integration techniques appeared to have an equivalent effect on the strength of the GFRP laminates. The higher overall maximum force exhibited by the cutout configuration is due to the additional fabric ply as opposed to the insertion configuration (Figure 7.4).

In contrast to the GFRP findings, the influence of DAFC integration on the strength of the CFRP laminates (Figure 7.7) was statistically insignificant for center and off center placement, since the decrease in maximum force was on the same order of magnitude as the standard deviation. However, the far off center placement showed a reduction in strength of 6-7%, regardless from the integration method. The maximum force values for the CFRP laminates with AFC showed a difference from between 5.5% to 11% as compared with the reference laminate.

The difference in the GFRP and CFRP behavior can be attributed to the ply arrangement of the two laminates as well as the difference in stiffness

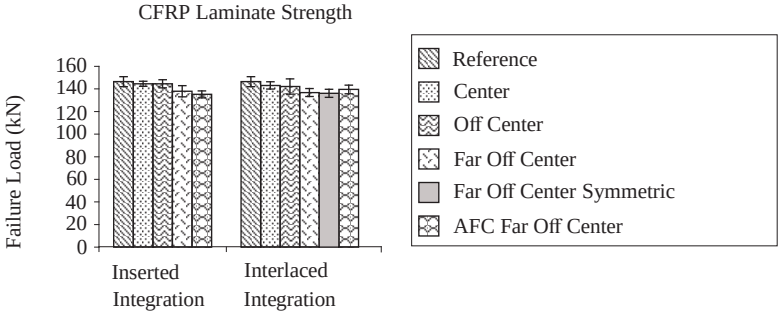

Figure 7.7: Failure load of the CFRP laminates.

between host laminate and inclusion. Integration directly affected the load bearing plies of the woven GFRP laminate, either directly via cutting in the cutout procedure or indirectly by creating angles in the plies near the edge of the integrated element. However, in the cross-ply CFRP laminates, the majority of the load was carried by the 0° plies, while only the 90° plies were affected during integration. Since the 90° plies were largely low load-bearing in this tensile configuration the effect on the strength of the laminate is small.

The strength reduction observed in the current study is similar to the values reported in the literature. Mall [136] reported no influence of PZT wafer integration on the ultimate strength of CFRP laminates, and Paget and Levin [124] reported an ultimate strength degradation of 4.5% for CFRP elements with integrated PZT elements. In the present study CFRP laminate strength decreases between 1 and 3% by integration in the center and off center positions. For the case of far off center symmetric DAFC integrated in GFRP laminates using the cutout method, a decrease of 32% in strength is observed. Results are in line with the findings from Crawley and De Luis [122], who observed a reduction of 20% in the ultimate tensile strength of $[0/90/0/90/0]_S$ GFRP laminates symmetrically inte-

grated with PZT wafers using the cutout method. The difference between the current results and those of Mall [136] could be explained considering the greater number of load bearing (0°) plies relative to the number of low load-bearing (90°) plies in the laminate as compared with the current study. The current findings combined with the literature show that the device placement through the laminate thickness is a critical design consideration concerning mechanical integrity of smart laminates.

Representative force/strain curves of the different GFRP configurations are displayed in Figure 7.8 and Figure 7.9 for each integration technique. The center placement GFRP specimens displayed a smooth loading profile. The off center specimens exhibited an extended plateau after reaching their maximum force values with both insertion and cutout integration techniques. This "yield point" corresponded with visual observations during the test of the onset of internal damage and delamination in the tensile specimens corresponding to extensive failure in the Kapton® layer of the DAFC, followed by catastrophic failure of the laminate. As can be seen from the two curves depicted in Figure 7.8 and Figure 7.9, the force for the far off center configuration decreases from the initial yield point, reaches an intermittent minimum, and then rises to a second force level where global laminate failure occurs. This behavior differs considerably from the center placement fracture behavior with DAFC inserted in the laminate's plane of symmetry where no such yield point was observed. In general, the CFRP laminates (Figure 7.10 and Figure 7.11) did not exhibit this type of loading behavior and no sign of failure in the integration region was observed prior to failure of the laminates. The AFC and the DAFC laminates show comparable failure load values for both center and far off center integration, a yield point is evident before final failure. A difference is seen in the Young's modulus data. The initial moduli are similar at low strain (below 0.03%), above this limit the modulus of the samples with integrated AFC was observed to be lower than that of the samples with DAFC. Previously published studies [137, 134] reported a tensile strain for AFC tensile specimen in the order of 0.25%. So, from a materials standpoint, beyond 0.25% damage may have ensued. If cracks developed in the AFC the stiffness of the structure would logically decrease. As seen in Figure 7.9 the initial slope appears similar, but changes beyond 0.50%, possibly indicating

damage in the AFC.

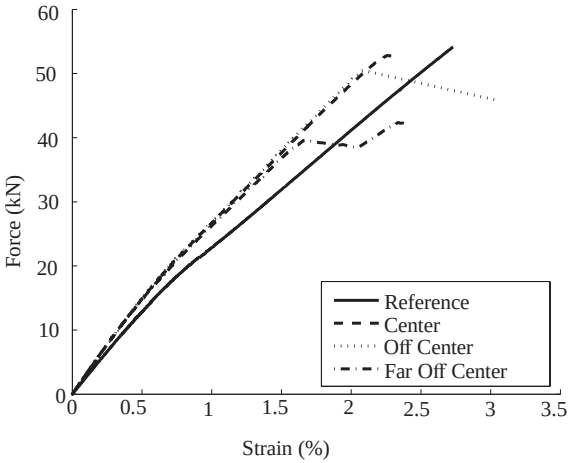

Figure 7.8: Mechanical response of GFRP laminates with DAFC using insertion integration.

7.5.2 Laminate Reliability Characterization

Although a number of mechanical characterization studies have been performed concerning the integration of PZT devices in laminate materials, tools for predicting the material system integrity have not been presented. Therefore, the laminate materials and integration configurations were modeled in ANSYS, and laminate integrity was characterized by calculating the TWSI values for the experimentally observed failure forces, and comparing the results with the experimental fracture patterns.

In Figure 7.12 the TWSI values (computed for the maximum force experimentally observed) are plotted for the integration region of the woven GFRP laminate with the inclusion inserted in the middle 0° ply of the com-

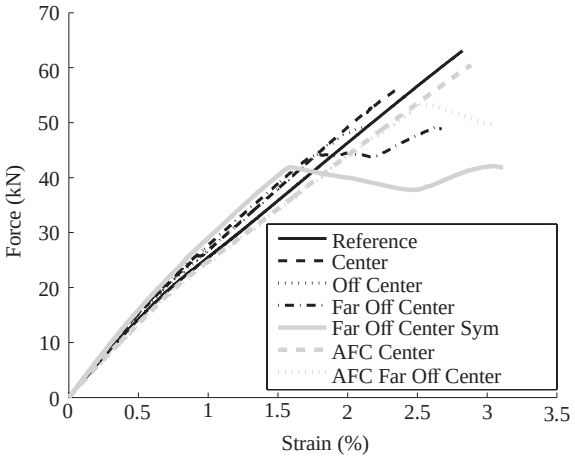

Figure 7.9: Mechanical response of GFRP laminates with DAFC and AFC using cutout integration.

posite. Higher values can be noticed near the lateral edges, which corresponds closely to the observed fracture patters. Is was noted during testing that failure occurred in the Kapton® layer prior to failure of the laminate. This explains the overcritical TWSI values computed for the maximum force. Again, the rather homogeneous TWSI values over the integration area are endorsed by the fairly uniform separation noticed across the entire Kapton® interface.

Conversely, the far off center fracture pictures display a more non-uniform pattern, with evidence of shearing and tearing within the Kapton® layer of the integration region. This behavior is comparable with the TWSI plot shown in Figure 7.13, where the model results show critical TWSI values concentrated at the edges perpendicular to the loading direction. A cross pattern is observed for both the numerical results and the experimental fracture, with evident tearing of the Kapton® layer.

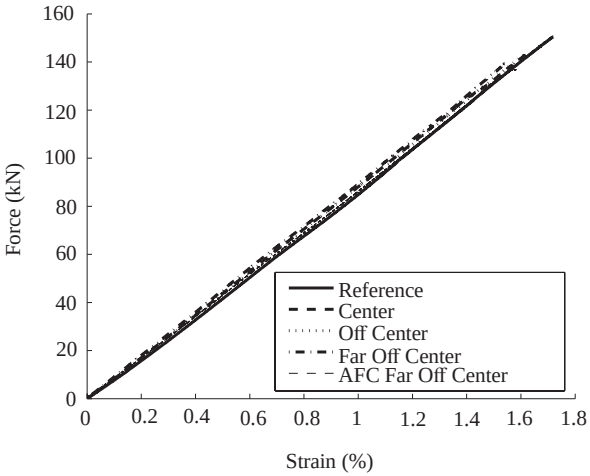

Figure 7.10: Mechanical response of CFRP laminates with DAFC and AFC using insertion integration.

Figure 7.14 depicts the TWSI plot for the top ply of the CFRP model with a far off center interlaced configuration. Stress concentrations are seen at the edges of the integration region, with failure being less likely in the center of the same integration region. These numerical results closely follow the observed fracture patterns, where sharp fracture lines can be recognized at the edges of the integration region.

The comparison between the TWSI plots and the experimental fracture patterns show that the modeling approach is accurately predicting the point of failure in the laminates.

7.5.3 Smart Functionality Characterization

To characterize the laminate integrity in relation to the smart functionality of the system, the FPF values were calculated for the laminates with

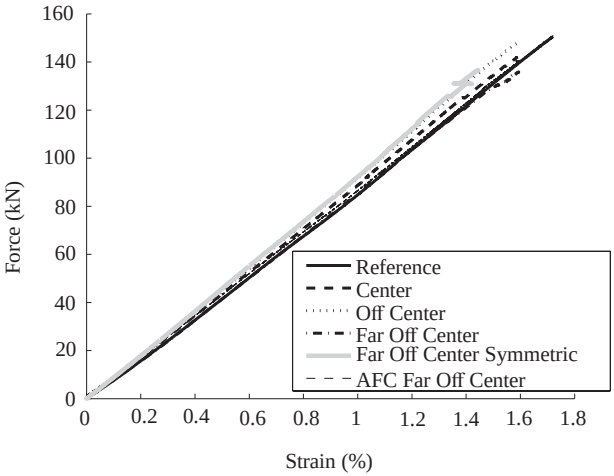

Figure 7.11: Mechanical response of CFRP laminates with DAFC and AFC using interlaced integration.

varying AFC position, and compared with the actuation and sensing ability of the laminates. The total strain energy of the cantilevered specimen induced by the actuated piezoelectric ceramic module was defined as the measure of actuation ability. This allows a direct comparison between center, off center and far off center configurations. Tip deflection is given as an additional quantity for off center and far off center configurations. Conversely, imposing a deflection at the tip and computing the voltage across the electrodes of the PZT module allowed the strain sensor function to be characterized. The modeling results are compiled in Figure 7.15 and Figure 7.16, and additionally presented in Table 7.4. The modeling results are normalized with respect to the performance of the far off center symmetric configurations in each laminate set.

Maximum strain energy and maximum tip deflection due to actuation and maximum sensor signal are realized when the actuator is placed as

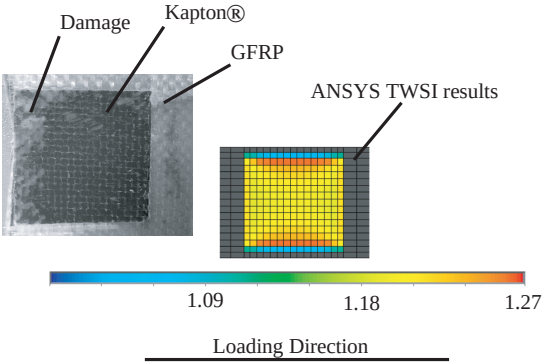

Figure 7.12: TWSI results for the integration region and DAFC post failure pattern. The configuration is GFRP inserted center.

far as possible from the midplane of the laminate. Laminate integrity was found to be highest when the actuator was integrated in the middle of the laminate thickness. However, this placement position gives little ability to actuate the laminate. Beam deflection actuation is only possible when the actuator is placed away from the plane of symmetry of the laminate.

Compared to cutout integration, insertion integration in GFRP laminates gives higher actuation capability at a comparable integrity decrease. The additional fabric in the cutout configuration (Figure 7.4) leads to a laminate with larger bending stiffness as opposed to the inserted configuration. For CFRP, the interlaced integration promises a lower affect on the integrity at comparable actuation capability compared to the inserted integration. Symmetric configurations show highest actuation capability while not further deteriorating laminate integrity. For CFRP, the symmetric con-

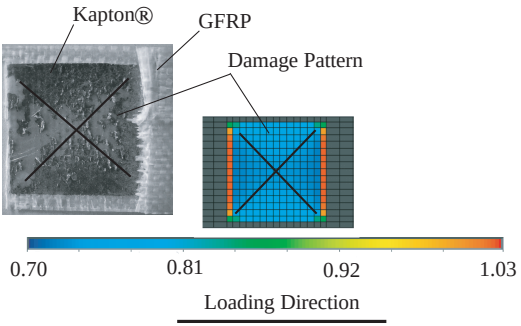

Figure 7.13: TWSI results for the integration region and DAFC post failure pattern. The configuration is GFRP inserted far off center.

figuration even shows a small integrity increase compared to the single far off center integration. In general, a larger affect of integration on FPF properties can be noted for the investigated fabric GFRP laminate compared to the cross-ply CFRP laminates.

Summarizing, additional actuation and sensing functionality and structural integrity were found to be two opposing design considerations. One will increase at the expense of the other. This illustrates the challenge in smart materials research, where one has to balance the different design needs to create a robust active material system.

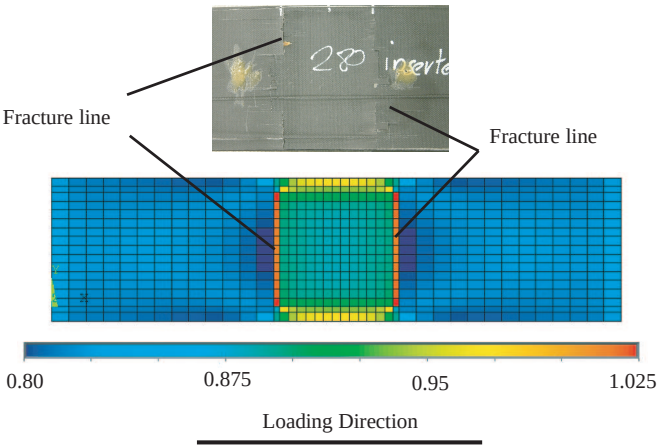

Figure 7.14: TWSI results for the top 0° ply. The configuration is CFRP interlaced far off center.

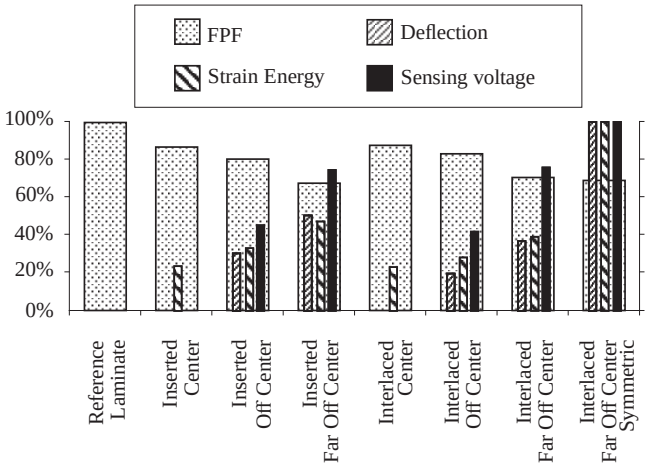

Figure 7.15: ANSYS results for GFRP laminates: relative FPF, deflection, strain energy and sensing voltage values.

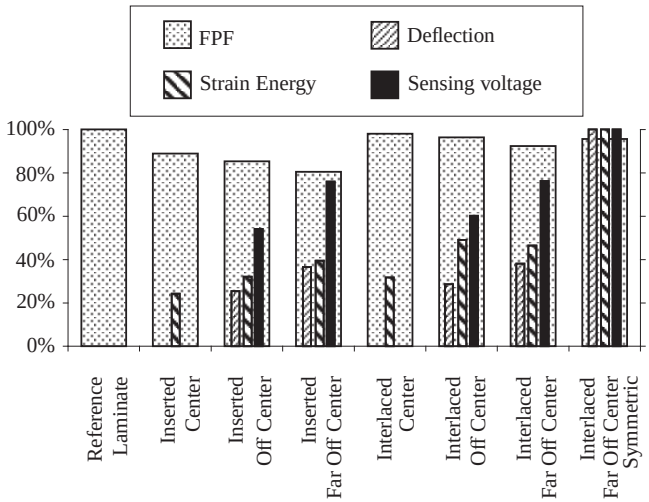

Figure 7.16: ANSYS results for CFRP laminates: relative FPF, deflection, strain energy and sensing voltage values.

Table 7.2: Experimental results from different GFRP integration configurations. Five specimen for each configuration were tested.

	Maximum force			Young's modulus		
	Mean [kN]	Δ	StDev [kN]	Mean [GPa]	Δ	StDev [GPa]
GFRP						
Reference Laminate Inserted	54.09	-	0.94 (1.74%)	25.57	-	0.20 (0.78%)
Inserted Center	50.83	-6.02%	1.22 (2.41%)	26.36	+3.09%	0.37 (1.42%)
Inserted Off Center	46.88	-13.33%	3.21 (6.84%)	26.23	+2.57%	0.20 (0.75%)
Inserted Far Off Center	40.43	-25.24%	3.35 (8.29%)	28.11	+9.91%	0.15 (0.55%)
Reference Laminate Cutout	59.89	-	3.78 (6.32%)	25.15	-	0.30 (1.19%)
Cutout Center	54.57	-8.89%	2.05 (3.75%)	25.69	+2.15%	0.51 (1.99%)
Cutout Off Center	48.96	-18.26%	3.16 (6.48%)	25.07	-0.29%	0.33 (1.32%)
Cutout Far Off Center	45.37	-24.26%	2.03 (4.90%)	26.50	+5.38%	0.51 (1.93%)
Cutout Far Off Center Sym	40.45	-32.46%	1.25 (3.09%)	28.20	+12.13%	0.30 (1.07%)
Cutout AFC Center	57.21	-4.48%	2.24 (3.91%)	22.71	-9.68%	0.51 (2.27%)
Cutout AFC Far Off Center	53.93	-9.96%	2.05 (3.80%)	23.05	-8.35%	0.28 (1.22%)

Table 7.3: Experimental results from different CFRP integration configurations. Five specimen for each configuration were tested.

	Maximum force			Young's modulus		
	Mean [kN]	Δ	StDev [kN]	Mean [GPa]	Δ	StDev [GPa]
CFRP						
Reference Laminate	146.44	-	4.47 (3.05%)	70.88	-	3.77 (5.32%)
Inserted Center	144.57	-1.28%	2.19 (1.52%)	68.01	-4.05%	1.95 (2.86%)
Inserted Off Center	144.57	-1.28%	3.63 (2.51%)	69.30	-2.23%	3.02 (4.36%)
Inserted Far Off Center	137.96	-5.79%	4.95 (3.59%)	67.58	-4.65%	2.74 (4.06%)
Inserted AFC Far Off Center	135.22	-7.66%	3.07 (2.27%)	67.57	-4.67%	2.70 (4.00%)
Interlaced Center	143.07	-2.30%	3.24 (2.26%)	69.31	-2.21%	0.98 (1.42%)
Interlaced Off Center	142.17	-2.92%	6.72 (4.73%)	70.46	-0.59%	2.12 (3.01%)
Interlaced Far Off Center	136.80	-6.58%	6.64 (4.85%)	72.54	+2.35%	1.71 (2.35%)
Interlaced AFC Far Off Center	139.58	-4.69%	3.82 (2.74%)	69.79	-1.53%	3.30 (4.73%)

Table 7.4: FPF values, sensing and actuation capability of different integration configurations. Numerical results from ANSYS modeling.

	FPF [kN]	Δ FPF	Deflection [μm]	Strain Energy [%]	Sensing voltage [%]
GFRP					
Reference Laminate	58.4	-	-	-	-
Inserted Center	50.8	-13.0%	-	23.66	0.00
Inserted Off Center	47.1	-19.3%	9.4	33.19	45.34
Inserted Far Off Center	39.6	-32.2%	15.6	47.30	74.56
Cutout Center	51.3	-12.2%	-	31.71	0.00
Cutout Off Center	48.7	-16.6%	6.1	49.02	60.16
Cutout Far Off Center	41.4	-29.1%	11.4	46.43	76.18
Cutout Far Off Center Symmetric	40.4	-30.8%	30.9	100.00	100.00
CFRP					
Reference Laminate	56.1	-	-	-	-
Inserted Center	49.9	-11.1%	-	24.23	0.00
Inserted Off Center	47.9	-14.6%	1.6	32.06	54.07
Inserted Far Off Center	45.2	-19.4%	2.3	39.43	75.93
Interlaced Center	55.1	-1.8%	-	23.15	0.00
Interlaced Off Center	54.1	-3.6%	1.8	28.27	41.26
Interlaced Far Off Center	51.9	-7.5%	2.4	39.26	75.91
Interlaced Far Off Center Symmetric	53.7	-4.3%	6.3	100.00	100.00

7.6 Conclusions

The work presented in this Chapter investigated the integration of piezoelectric ceramic sensors and actuators into glass and carbon fiber composite laminates. Compared to previous contributions, which largely focused on the integration of PZT wafer actuators in either GFRP or CFRP laminates with a high ratio of passive to active plies, this work offers a more comprehensive picture. Experimental work was coupled with numerical modeling of laminate designs to characterize the mechanical reliability of smart laminates as balanced against their smart functionality. This study focused on the integration of AFC actuators and included variation of device placement through the laminate thickness as well as covering different integration methods, including insertion, cutout and interlacing.

In this study, laminate reliability and beam actuation capability were found to be opposing design considerations. Laminate reliability was highest when elements were integrated into the center of the composite laminates, while actuation ability was best realized when elements were positioned near the laminate surface, which lead to the most significant degradation in the mechanical strength properties of both the GFRP and CFRP laminates. The penalty associated with integration on laminate integrity could be mitigated by integrating devices in the low load-bearing laminate plies, such as the 90° plies of a CFRP cross-ply laminate. The fracture and failure patterns observed experimentally correlated with TWSI plots of numerical results.

It was found that the best trade-off between mechanical reliability and smart functionality can be realized using interlaced far off center symmetric integration in cross-ply laminates. In general, interlacing was shown to increase FPF values by distributing the inclusion discontinuity throughout the laminate.

Part IV

Structural Vibration Control via Shunted Piezoelectric Ceramic Modules

Chapter 8

Structural Vibration Control via R–L Shunted Active Fiber Composites

The work presented in this Chapter can be found with minor modifications as a publication in the scientific literature as:

A. Belloli, D. Niederberger, S. Pietrzko, M. Morari and P. Ermanni. Structural Vibration Control via *R-L* Shunted Active Fiber Composites. *Journal of Intelligent Material Systems and Structures*, 18(3):275-287, 2007.

This chapter presents a successful extension of passive *R–L* shunt damping to piezoelectric ceramic elements working in direct 3-3 mode and a performance comparison to elements working in indirect 3-1 mode. A new circuit topology is implemented to synthesize the very large inductances required by the low inherent piezoelectric device capacitance at relatively low frequencies. This allows for efficient tuning of the *R–L* circuit to the

structure resonance frequency to be damped. The vibration suppression performance of monolithic piezoelectric ceramic actuators and active fiber composites is compared in this study. For this purpose, different actuators are bonded on aluminum cantilever plates. An integrated FE model is implemented for the prediction of structure resonance frequencies, optimum values for electrical components, and the resulting vibration suppression performance. The passive structure, bonded active patch, and shunted electrical network are analyzed within the same FE model. Active fiber composite patches working in the direct 3-3 mode show equivalent specific damping performance compared to conventional monolithic 3-1 actuated patches. Issues related to the sensitivity of *R–L* shunts to variations in environmental and operational conditions are discussed in this study. In short, monolithic actuators operating on the 3-1 piezoelectric effect seem to be the best for use in *R–L* shunting.

8.1 Introduction

Different methods are used to decrease peak vibration amplitudes of lightweight structures. A common approach is to increase the level of damping over a broad frequency range through passive, surface damping treatments (e.g., in the form of free or constrained layers of viscoelastic material). The main drawbacks of this method are the additional mass and large temperature dependence of material properties. Low frequency vibrations can be effectively damped by bonding or embedding piezoelectric elements on the structure without significantly changing its dynamic properties or increasing mass. Active systems [138, 139, 140, 141] require associate electronics for piezoelectric elements acting as sensors, whereas complex amplifiers are needed for driving the actuators. An alternate method of vibration control uses a passive electrical network attached across the terminals of a piezoelectric transducer. This is referred to as shunt damping [142, 143, 144, 145, 20] . Among different electrical shunt networks – described in more detail in the next section – a resonant shunt consisting of an inductor and a resistor (*R–L* shunt) achieves very good vibration suppression for one structure resonance [142]. Adachi et al. [49] extended

shunt damping to piezoelectric elements working in the direct 3-3 mode. They found the damping enhancement performance of macro-fiber composite (MFC) actuators to be superior to that of conventional monolithic actuators operating on the indirect 3-1 effect. However, their statement rests on results obtained with different shunt circuits (floating simulated inductor for the MFC actuator and grounded simulated inductor for the monolithic 3-1 actuator). Comparing the vibration suppression performance using the grounded simulated inductor for both devices, the conventional 3-1 actuator outperformed the MFC actuator. In this work the use of *R–L* shunts is extended to active fiber composites (AFC). Just like MFC, AFC represent a promising solution in applications where their anisotropic actuation or high conformability is indispensable for extending the design space. They show great potential toward integration in complex, double curved composite structures. Lower mass density makes them suitable for large surface covering. The vibration suppression performance of different piezoelectric actuators with shunted *R–L* circuits is compared both numerically and experimentally. A fully integrated FE model predicts the dynamic response of open and shunt damped systems. The need for an adaptation of the tuning inductance L is experimentally assessed by investigating the inherent piezoelectric capacitance as a function of temperature.

8.2 Shunt Control Damping

The general method of shunt control damping takes advantage of the relatively strong electromechanical coupling exhibited by commercially available piezoelectric ceramics. As the piezoelectric element – bonded on or embedded in a structure – strains, a portion of the mechanical vibration energy is converted into electrical energy, which can be treated in a network of electrical elements connected to the piezoelectric ceramic patch (Figure 8.1).

Six basic shunt circuit configurations are known from the literature. Resistive shunts with a single resistor [142] dissipate energy through Joule heating, showing an effect similar to structural damping. Owing to the poor power factor, limited vibration suppression performances can be achieved.

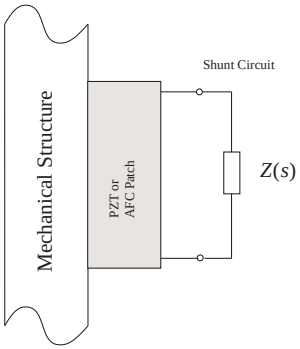

Figure 8.1: Schematic of a piezoelectric patch with shunted circuit.

Resonant shunts [142] build *L–C–R* circuits with the inherent piezoelectric capacitance, and behave in a similar fashion to mechanical vibration absorbers. Capacitive shunts [146, 147, 148] are often used in tunable mechanical vibration absorbers, because they change the effective stiffness of the piezoelectric element. The inherent piezoelectric capacitance can be neutralized by negative capacitor shunts [149], which achieve efficient broadband vibration suppression performance. The main drawbacks of this technology are difficult tuning and instability for small variations in environmental or operation conditions. Enhanced vibration suppression performance in the presence of environmental and operation condition changes can be achieved by means of active piezoelectric shunts [150]. However, they require a parametric model of the system and external power supply. Switched shunts [151, 152], where either an *R* or *R–L* network is switched to the piezoelectric element, feature rapid response to the instantaneous condition of the system and do not require such high inductor values as inductive shunts. An easy-to-implement solution of switched shunts is presented in [153] and [20]. A very small amount of power is required to drive the switch, because MOSFETs are used. This power is supplied by a second piezoelectric element. For a detailed review on vibration damping

using shunted piezoelectric materials, the interested reader is referred to Fleming [21] and Niederberger [20]. In this Chapter, the vibration suppression performance of electrical *R–L* networks shunted to different piezoelectric ceramic elements is investigated. The *R–L* shunt used consists of a serial inductor with a resistor as shown in Figure 8.2.

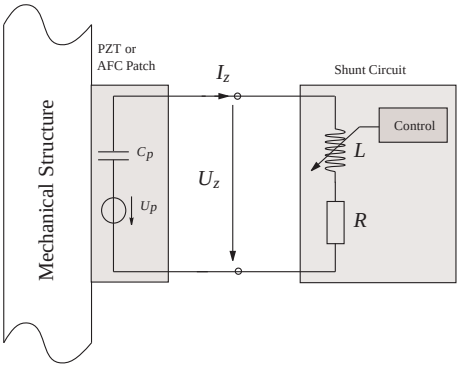

Figure 8.2: Adaptive *R-L* shunted piezoelectric patch.

According to Hagood and von Flotow [142], optimal vibration suppression is achieved for

$$L^* = \frac{1}{\omega_n^2 \left(1 + K_{ij}^2\right) C_p} \text{ and } R^* = \frac{\sqrt{2}\frac{K_{ij}}{1+K_{ij}^2}}{C_p \omega_n}, \tag{8.1}$$

where ω_n denotes the structure resonance frequency to be damped, K_{ij} the generalized electromechanical coupling coefficient for the desired mode (defined in Equation 8.3), and C_p the inherent piezoelectric capacitance. This shunt has been previously used to reduce the vibration of rotor blades in helicopters [31], turbo machine blades [154], and for sport equipments like snowboards [155]. It was also successfully applied to increase the sound transmission loss of structures [156, 157] or to damp aircraft structures [158]. The vibration suppression performance of *R–L* shunts is very

sensitive to parameter variations, such as temperature, structural load, or piezoelectric coefficients.

8.3 Experimental

8.3.1 Investigated Actuators

Five different piezoelectric ceramic actuator patches covering the same active area ($45.97 \times 20.57\, mm^2$) were investigated. Strain actuators consisting of a 0.254 mm thick, monolithic piezoelectric ceramic wafer – exploiting both the indirect 3-1 and the stronger direct 3-3 piezoelectric effect – were supplied by Midé Corp.[1]. They are schematically represented in Figure 8.3 (a) and (b).

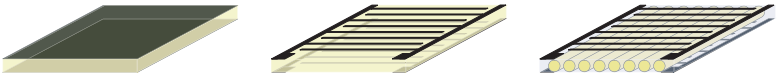

a) b) c)

Figure 8.3: Investigated piezoelectric actuators. a) *QP*10*N*, operating on the indirect 3-1 effect , b) *QP*10*Ni* and c) AFC, both operating on the stronger direct 3-3 effect.

As an alternative actuator system, AFC were investigated [89, 61, 47, 90]. Active fiber composites are composed of piezoelectric ceramic fibers and epoxy resin [93]. Interdigitated electrodes (IDEs) are used for poling and to direct the electrical field along the longitudinally oriented fibers (Figure 8.3 (c)). Just as the monolithic wafer operating on 3-3 effect, AFC achieve greater actuation energy density by exploiting the d_{33} piezoelectric charge coefficient along the fibers. The response behavior of AFC can be tailored by changing the ratio between electrode spacing p and fiber diameter d and the ratio between electrode width w and electrode spacing p. Previously published works [90, 60, 159] show actuation improvements

[1] Midé Technology Corp., 200 Boston Ave., Medford, MA 02155 USA, www.mide.com

for larger p/d ratios. Bent and Pizzochero [47] also report higher coupling coefficient, k_{33}, which is expected to be beneficial for passive damping applications. In this study, three different configurations were investigated for shunt damping. AFC Type A is the standard AFC configuration manufactured at EMPA. The configuration AFC Type B presents a larger *p/d* ratio for enhanced coupling coefficient. AFC Type C features a larger *w/p* ratio for maximum device capacitance. The different AFC configurations are summarized in Table 8.1.

Table 8.1: Fiber diameter *d*, electrode width *w*, and electrode spacing *p* for different AFC configurations.

Configuration	d [μm]	w [μm]	p [μm]
AFC Type A	255	200	1100
AFC Type B	255	150	1750
AFC Type C	255	200	600

All AFC configurations present an active piezoelectric volume of $\approx$ 150 mm^3, compared to $\approx$ 240 mm^3 for the monolithic wafers.

8.3.2 Capacitance Investigation

The *R–L* shunts are known to be very sensitive to variations in environmental or operation conditions. The *L–C* circuit gets de-tuned [160] as the inherent piezoelectric capacitance changes as a function of temperature [161] and aging or for changing structure resonance frequencies. As a result, vibration suppression performance dramatically drops. This could be the case for space applications (-200 to 200°C), brakes (0–100°C), or even skis (-30 to 15°C). In order to assess their sensitivity to varying operation conditions, the inherent capacitance values of the different piezoelectric elements were investigated as a function of temperature. The aluminum plates with bonded piezoelectric ceramic elements were conditioned in a Thermicon P oven from Heraeus Instruments. Capacitance and resistance values of the piezoelectric ceramic elements were measured as a function

of frequency (range 100 Hz–10 kHz) and temperature (range 20–100°C) using an impedance/gain-phase analyzer HP4194A from Hewlett Packard. The piezoelectric ceramic elements were short-circuited during heating, in order to avoid pyroelectric voltages.

8.3.3 Vibration Suppression Investigation

Experimental Setup

The vibration suppression experiments were carried out on a rectangular cantilever aluminum plate as shown in Figure 8.4 (dimensions are reported in Table 8.2, material properties in Table 8.3).

Table 8.2: Experimental setup: dimensions and locations.

b	100 mm
l	250 mm
t	3 mm
x_p	50 mm
y_p	133 mm
b_p	25.4 mm
l_p	50.8 mm
e	13 mm
m	245 mm

Table 8.3: Material properties for the AlSi1MgMn aluminum alloy.

AlSi1MgMn		
Density	ρ [kg/m^3]	2700
Young's Modulus	E [GPa]	69
Poisson ratio	ν [–]	0.33

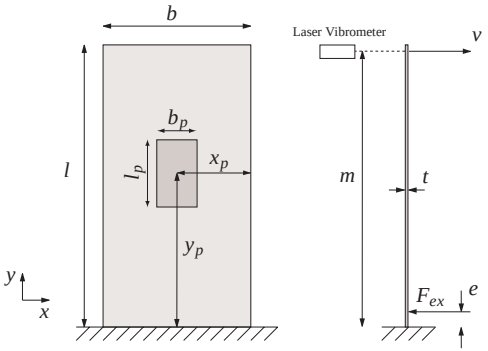

(a)

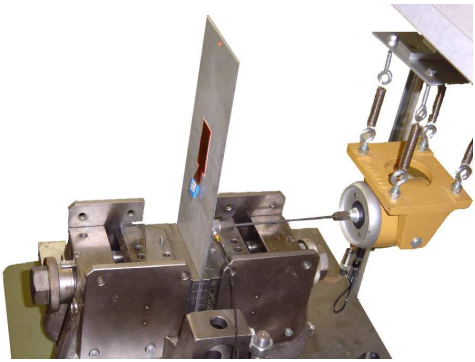

(b)

Figure 8.4: Experimental setup: cantilever plate with bonded piezoelectric ceramic patch; excitation and measurement locations.

According to the supplier [2], piezoelectric low-field properties of the used PZT5A1 ceramic material (also known as Navy Type II) are (measured in monolithic wafers):

$$\begin{aligned} d_{33} &= 440\text{pm/V} \\ d_{31} &= -185\text{pm/V} \\ d_{15} &= 560\text{pm/V} \end{aligned}$$

The optimum bonding location for the five different patches was determined by maximizing the deformation energy due to the single-signed bending strain in the active patch area [162]. All actuators feature equivalent active areas and similar thickness, thus experiencing the same strain distributions. The structure was excited by an electromechanical shaker V201/3 from LDS[3] whereas the structure tip velocity was measured with a laser Doppler vibrometer PSV-200 from Polytec[4].

Shunt Control Circuit

As the inherent piezoelectric capacitance of AFC and monolithic patches operating on the 3-3 effect is very small, and the desired tuning frequency is fairly low, very large inductance values L^* are needed for tuning the R–L shunt circuit (Equation 8.1). Conventional virtual inductors [163, 164] are not able to synthesize such a huge inductance with sufficient low serial resistance because they cannot drive the very small piezoelectric capacitance accurately enough. This was observed in Sato et al. [165], where a vibration reduction of only 0.45 dB was obtained with an R–L shunted piezoelectric ceramic fiber composite patch. In order to efficiently extend the use of R–L shunts to piezoelectric ceramic elements working in 3-3 mode, the synthetic impedance circuit [166] shown in Figure 8.5 has been chosen. The desired impedance transfer-function defined by $U_z(s)/I_z(s) = Z(s)$ is

[2] Smart Material Corp., 4721 White Tail Lane, Sarasota, FL 34238 USA, www.smart-material.com

[3] Ling Dynamic Systems Ltd., Baldock Road, Royston, Hertfordshire SG8 5BQ GB, www.lds-group.com

[4] Polytec GmbH, Polytec-Platz 1, D-76337 Waldbronn, www.polytec.com

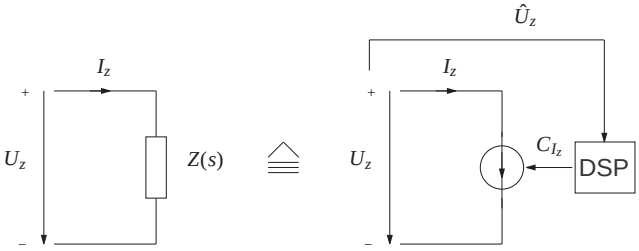

Figure 8.5: Synthetic Impedance Circuit.

implemented by measuring the voltage $U_z(s)$ and controlling the terminal current $I_z(s)$. With this configuration, an arbitrary electrical network $Z(s)$ can be synthesized. The digital signal processor (DSP) controlling the current source is implemented with the xPC-target system of MATLAB[5]. The topology of the electrical shunt network and its parameters can therefore easily and quickly be changed.

Vibration Suppression Performance

For evaluating the vibration suppression capability of different piezoelectric ceramic patches, the transfer function from a disturbance force $F_{ex}(s)$ generated by the shaker to the velocity of the structure tip $v(s)$ was measured:

$$G_v(s) = \frac{v(s)}{F_{ex}(s)}. \tag{8.2}$$

In addition, the plate was harmonically excited at the resonance frequency of the second bending mode. At time 1s excitation was switched off and the vibration decay for the open and shunt damped system was compared.

[5]The MathWorks, Inc., 3 Apple Hill Drive, Natick, MA 01760-2098 USA, www.mathworks.com

8.4 Modeling

The design of load carrying structures with bonded or embedded sensors and actuators requires adequate tools for predicting their static and dynamic behavior. An approach for modeling structures containing piezoelectric ceramic actuators using commercially available FE packages was presented by Reaves and Horta [167]. Côté et al. [168] proposed a simplified multilayer tri-dimensional model based on the analogy between thermal and piezoelectric strains. Complex geometry and non-uniform electrical field distributions in piezoelectric ceramic elements working in 3-3 mode require hierarchical modeling for efficient simulation. Shunted electrical networks can be integrated in the model by means of new analysis capabilities offered by FE packages.

8.4.1 Actuator's Effective Properties

The conventional monolithic strain actuators operating on the indirect 3-1 effect are composed of a single piezoelectric ceramic wafer with metal electrodes sputtered on both surfaces. The electrical field distribution inside the piezoelectric material is uniform and perpendicular to the electrodes. Such actuators can easily be modeled as a single volume having defined material properties. Actuators working in the 3-3 mode, by contrast, present a non-uniform electrical field distribution inside the piezoelectric material. Furthermore, AFC are composed of piezoelectric ceramic fibers and epoxy resin. Interdigitated electrodes are used both for poling and for actuation of the piezoelectric ceramic material. This leads to regions with opposed polarization between the electrodes and to the so-called 'dead zones' underneath the electrodes. In order to minimize computational requirements, monolithic 3-3 and AFC patches were modeled as a series of volumes presenting alternating material properties. Effective properties account for reduced polarization and actuation inside the piezoelectric material as well as for the relative contributions of piezoelectric ceramic fibers and epoxy resin. Either analytical or numerical methods can be applied on representative volume elements (RVE, see Figure 4.1) for determination of the effective properties.

In his PhD thesis, Bent [61] proposed an analytical model as summation of parallel and series additions of two-phase materials. The resulting uniform fields model (UFM) is a generalization of the well known "rule of mixtures" and assumes the uniformity of the electrical and mechanical fields in each single phase. The UFM simplifies the complex geometry of the RVE, thus not taking into account the electrical field distortion under the electrode fingers. In the present study, FE models of the respective RVE allowed for visualization of the electrical field variations in the single phases. This is of special interest in the "dead zone" under the electrode finger, where the actuation is supposed to be very small or completely absent. In addition, FE models considered the fiber diameter, the fiber volume fraction, and the contact angle between electrode finger and piezoelectric fiber, characteristic of AFC. Needed quantities were determined by means of micrographic imaging technology. AFC were cut at different angles and observed under the optical microscope, as described in Chapter 4 and shown in Figure 4.3.

The effective properties were determined by applying four different load cases to the RVE, each with different electrical and mechanical boundary conditions (Table 8.4). Resulting reaction forces and electrical displacements were evaluated to obtain effective stiffness coefficients, effective piezoelectric clamped stress coefficients, and effective dielectric coefficients.

8.4.2 Integrated FE Model

In this study, the damping performance of the different patches is predicted by an integrated FE analysis. SOLID 45, eight-node 3D structural elements were used to model the passive structure; SOLID 5, eight-node 3D coupled field elements were used for the piezoelectric material. The shunt circuit was implemented using CIRCU 94 elements. The actuators' capacitance was first predicted by a static analysis. The charge collected on the electrodes divided by the applied voltage yielded the capacitance of the different piezoelectric elements. Modal analysis was then carried out in order to extract the resonance frequencies for open and short circuit regimes. Generalized electromechanical coupling coefficients for a selected n^{th} mode

Table 8.4: Load cases summary.

Case	Mechanical BC	Electrical BC on electrode	Obtained effective properties			
1	all faces clamped	V=U/2	ε_3^{eff}	e_{31}^{eff}	e_{32}^{eff}	e_{33}^{eff}
2	displ. u_1 at $x = b/2$	V=0	c_{11}^{eff}	c_{12}^{eff}	c_{13}^{eff}	e_{31}^{eff}
3	displ. u_2 at $y = t/2$	V=0	c_{12}^{eff}	c_{22}^{eff}	c_{23}^{eff}	e_{32}^{eff}
4	displ. u_3 at $z = p/2$	V=0	c_{13}^{eff}	c_{23}^{eff}	c_{33}^{eff}	e_{33}^{eff}

were determined as

$$K_{ij}^2 = \frac{(\omega_n^D)^2 - (\omega_n^E)^2}{(\omega_n^E)^2}, \tag{8.3}$$

where ω_n^D and ω_n^E are the resonance frequencies of systems with open and short circuited patch, respectively. Subscripts i and j denote the field and loading direction, respectively. Optimum values for R^* and L^* were computed according to Equation 8.1, thus tuning the R–L shunt to the second bending mode. A harmonic analysis was finally carried out for the addressed frequency spectrum. For prediction of the vibration suppression performance, the transfer function from a unit excitation force $F_{ex}(s)$ generated by the shaker to the tip displacement $X(s)$ of the structure was computed in the Laplace domain. Accordingly, the velocity of the structure is defined as

$$v(s) = s \cdot X(s). \tag{8.4}$$

8.5 Results and Discussion

8.5.1 Capacitance

The inherent capacitance values of different piezoelectric elements were measured and evaluated at the representative frequency of 250 Hz for temperatures ranging from 20 to 100°C. Matching specifications from the piezoelectric ceramic manufacturer [169], the actuator operating on the 3-1 effect shows a nearly quadratic behavior in the region of interest (Figure 8.6). On the other hand, the behavior of actuators with interdigitated electrodes working in 3-3 mode is best approximated with a third-order fit. As expected, the AFC configuration has a large influence on the resulting device capacitances. AFC Type C shows a larger capacitance than standard configuration AFC Type A whereas AFC Type B shows a smaller capacitance. The slope of the respective linear regression between 20°C and 80°C normalized with respect to capacitance value at room temperature (23°C) is taken as a relative capacitance change per °C. As summarized in

Table 8.5, AFC patches show lower relative capacitance change compared to monolithic actuators. The relative capacitance changes visibly increase for piezoelectric elements working in 3-3 mode above 80°C.

Table 8.5: Device capacitance measured at 250 Hz and room temperature; relative capacitance change per °C (linearly interpolated between 20°C and 80°C).

Patch	C_p at 23°C [nF]	Rel. ΔC_p [%/°C]
Monolithic 3 – 1	35.7	0.57
Monolithic 3 – 3	0.941	0.47
AFC Type A	0.862	0.24
AFC Type B	0.296	0.16
AFC Type C	2.44	0.16

Results reveal the need for an adaptation algorithm for the tuning inductance L, which is very sensitive to the inherent piezoelectric capacitance C_p and to the structure resonance frequency ω_n that may vary in time. A realtime tracking of the optimum inductance value can efficiently be implemented by means of the relative phase adaptation, that was shown to converge faster than former adaptation laws [170, 171], and is easier to implement. The relative phase adaptation of L is

$$\frac{dL(t)}{dt} = \beta \left(g_{LP}(t) * [v(t) \cdot I(t)] \right), \tag{8.5}$$

where $g_{LP}(t)$ represents the impulse response of a low-pass filter with a cut-off frequency below $2\omega_n$ (ω_n is the resonance frequency to be damped), β the tuning parameter, $v(t)$ the velocity on the structure where the piezoelectric patch is attached, $I_z(t)$ the current in the shunt circuit, and $*$ denotes the time domain convolution operator. For more information the reader is referred to Niederberger [160, 20].

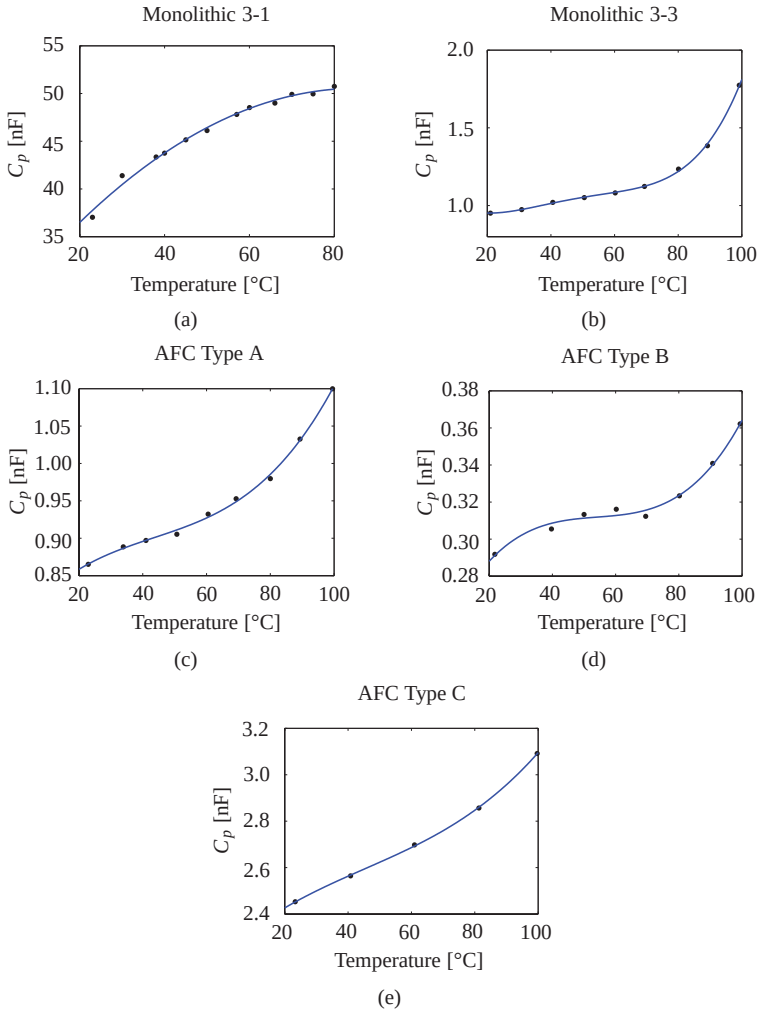

Figure 8.6: Capacitance of the different piezoelectric ceramic elements as a function of temperature: (•) measurement points, (—) second-order fitting (monolithic 3-1), and third order fitting, respectively.

8.5.2 RVE and Effective Properties

The isopotential lines in Figure 8.7 (a) exemplarily show the potential distribution in the RVE for the actuator AFC Type A. Owing to the ev-

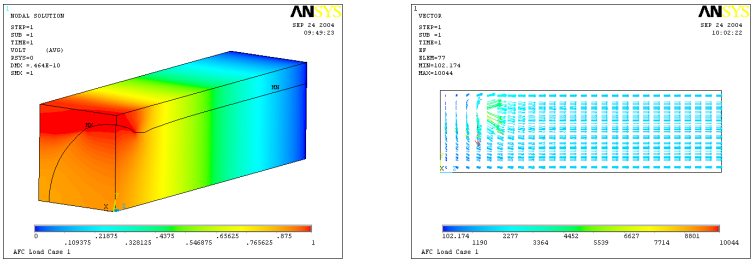

(a) (b)

Figure 8.7: (a) Potential distribution, and (b) electrical field lines in the RVE. Note the 'dead zone' under the electrode surface.

ident field distortion (see the electrical field lines in Figure 8.7 (b)), the region under the electrode is not poled in the longitudinal direction. Taking into account the resulting 'dead zone', effective stiffness coefficients, effective piezoelectric clamped stress coefficients, and effective dielectric coefficients were computed for different RVEs applying the boundary conditions described in Table 8.4 [61]. Effective stiffness coefficients include the contribution from the polyimide film and – in the case of AFC – the reduced fiber stiffness as reported by Kornmann and Huber [172]. A summary of the resulting effective material properties is given in Table 8.6.

Dominant piezoelectric stress coefficients are e_{31} for monolithic 3-1, e_{33} for monolithic 3-3 and AFC.

Table 8.6: Effective material properties for the different patches.

	QP10N	QP10Ni	AFC Type A	AFC Type B	AFC Type C
e_{31} [C/m^2]	-5.35	-0.62	-0.15	-0.15	-0.14
e_{32} [C/m^2]	-5.35	-0.19	-0.14	-0.15	-0.14
e_{33} [C/m^2]	15.78	5.60	4.13	4.17	3.90
e_{15} [C/m^2]	12.3	0	0	0	0
$\varepsilon_1^S/\varepsilon_0$	916	916	916	916	916
$\varepsilon_3^S/\varepsilon_0$	830	1060	911	853	1022
c_{11}^E [GPa]	120	56.3	16.4	16.4	16.4
c_{12}^E [GPa]	75.2	10.3	6.6	6.6	6.6
c_{13}^E [GPa]	75.1	25.4	8.49	8.50	8.47
c_{22}^E [GPa]	120	16.6	15.0	15.0	15.0
c_{23}^E [GPa]	75.1	10.2	8.33	8.34	8.31
c_{33}^E [GPa]	111	52.0	22.8	22.6	23.4
c_{44}^E [GPa]	21	21	21	21	21
c_{66}^E [GPa]	21	21	21	21	21

8.5.3 Piezoelectric Coupling and Optimum Parameters

Static analysis computed higher device capacitance values compared to the experimental results (Table 8.7). The mismatch is due to the larger electrode area of the simplified model and to the different measuring frequency. However, this does not affect the prediction accuracy of the subsequent modal and harmonic analyses. Modal analysis yielded eigenfrequencies for open, respectively short circuit regimes. Generalized electromechanical coupling coefficients for the second bending mode were determined by applying Equation 8.3.

Significantly lower generalized electromechanical coupling coefficients are predicted for plates with bonded AFC, compared to monolithic actuators. Neglecting material damping, Hagood and von Flotow [142] predicted

$$\max_{\omega} |\Phi_{TF}^{opt}(i\omega)| = \frac{\sqrt{2}}{K_{ij}\sqrt{1+K_{ij}^2}}, \tag{8.6}$$

as the maximum amplitude for the optimally *R-L* shunt damped transfer-function in the vicinity of ω_n. Best vibration suppression performance is accordingly expected for the plate with a bonded monolithic 3-1 actuator. Optimum resistance and inductance values for the *R–L* shunt were computed according to Equation 8.1. Actuators working in 3-3 mode require very large inductance values compared to the actuator working in 3-1 mode. The larger capacitance of the AFC Type C patch – achieved with a configuration featuring smaller electrode spacing and larger electrode area – somewhat mitigates the inductance requirements of the *R–L* shunt.

8.5.4 Vibration Suppression

In the first experiment, transfer-functions $G_v(s)$ from disturbance to velocity of the aluminum cantilever plate structure tip were measured. The second bending mode is efficiently damped, whereas no influence is noticed on the first bending mode (see Figure 8.8 for a representative plot of the transfer-function's magnitude over the measuring frequency range).

Table 8.7: Device capacitance; eigenfrequencies in open and short circuit regime; generalized electromechanical coupling coefficient; optimum resistance and inductance values computed for the different patches.

	QP10N	QP10Ni	AFC Type A	AFC Type B	AFC Type C
Device Capacitance [nF]	77.8	1.19	1.90	0.78	6.44
Open Circuit Frequency [Hz]	251.23	252.12	251.12	250.74	251.10
Short Circuit Frequency [Hz]	251.01	251.94	251.03	250.64	251.02
K_{ij}^2 [$\cdot 10^{-3}$]	1.73	1.43	0.70	0.75	0.63
Optimum Resistance [Ω]	478.14	28419.81	12479.92	31605.71	3490.12
Optimum Inductance [H]	5.16	335.95	211.65	519.61	62.46

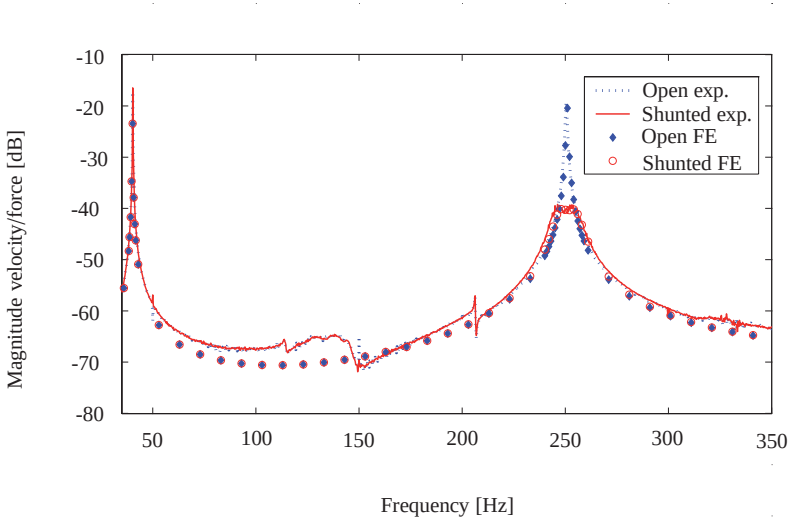

Figure 8.8: Magnitude of a representative transfer function $G_v(s)$ measured and simulated for the different patches.

More detailed results for the open and the shunt damped systems are shown in Figures 8.9, 8.10 and 8.11. Looking first at vibration reduction – a commonly accepted way to assess additional damping introduced by active or passive measures –, no significant performance difference can be appreciated between the different piezoelectric patches (Table 8.8).

On closer inspection, one realizes large variations in measured peak magnitude of transfer-functions for open systems, which can be attributed to the extremely low material damping ratio of the aluminum material used. The steepness of the resonant peak shoulders makes accurate determination of its magnitude difficult. The vibration suppression level of the optimally damped system is thus chosen as the standard of comparison.

The conventional monolithic actuator working in 3-1 mode achieves the lowest vibration level. The monolithic 3-3 actuator does not quite match the vibration suppression performance of the monolithic 3-1 actuator. Electrical field distortions lessen the effect of the larger d_{33} piezoelectric charge coefficient. AFC Type A achieves an even lower vibration suppression performance, laying some 4 dB above the monolithic 3-1 actuator. Despite showing reduced actuation efficiency [159], AFC Type C achieves equivalent vibration suppression performance when compared to AFC Type A. The above results are in line with predicted values for generalized electromechanical coupling coefficients (Table 8.7) and Equation 8.6. Accounting for their reduced active volume, AFC patches achieve the same vibration suppression performance per active unit volume as the monolithic 3-1 actuator and outperform the monolithic 3-3 actuator. Despite its somewhat higher generalized coupling coefficient, a vibration reduction of less than 3 dB could be achieved for the AFC Type B patch. The bandwidth of the implemented synthetic impedance is severely limited by the very small capacitance of the actuator, which cannot be driven accurately enough. Including a negative resistance into the shunt circuit would represent a possible solution to the problem.

The vibration suppression was successfully predicted by the integrated FE model. Excellent agreement can be observed in Figures 8.9, 8.10 and 8.11 between measured and simulated transfer-functions. Both eigenfrequencies and vibration suppression levels are accurately predicted. The implementation of *R–L* shunt circuits for piezoelectric ceramic elements working in 3-3 mode is thus nearly ideal; their falling short of expectations cannot be attributed to the synthetic impedance circuit. Moreover, harmonic analysis predicts an equivalent vibration reduction performance of the AFC Type B system compared to configurations AFC Type A and AFC Type C.

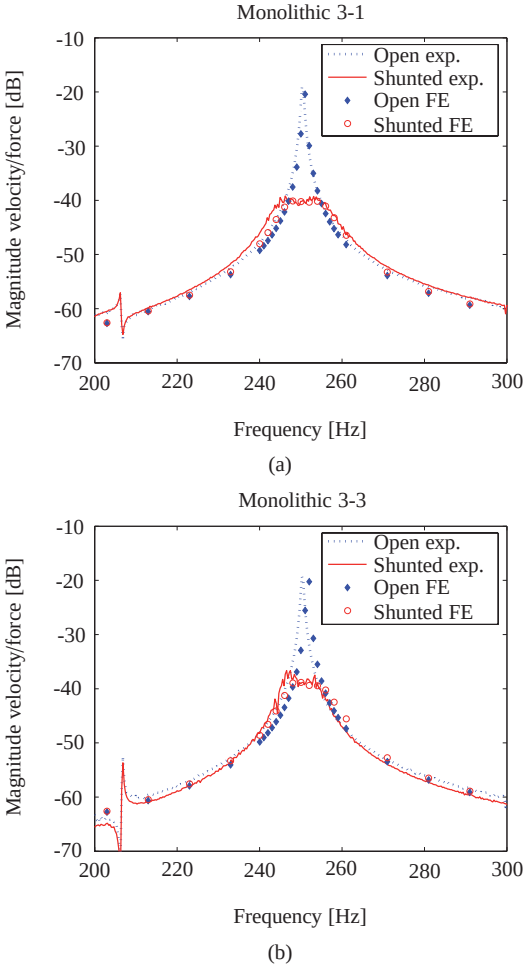

Figure 8.9: Magnitude of measured and simulated transfer-functions $G_v(s)$ from disturbance to tip velocity of the structure for the open system (⋯ and ♦, respectively) and for the shunted system (— and ○ respectively); (a) Monolithic 3-1, (b) Monolithic 3-3.

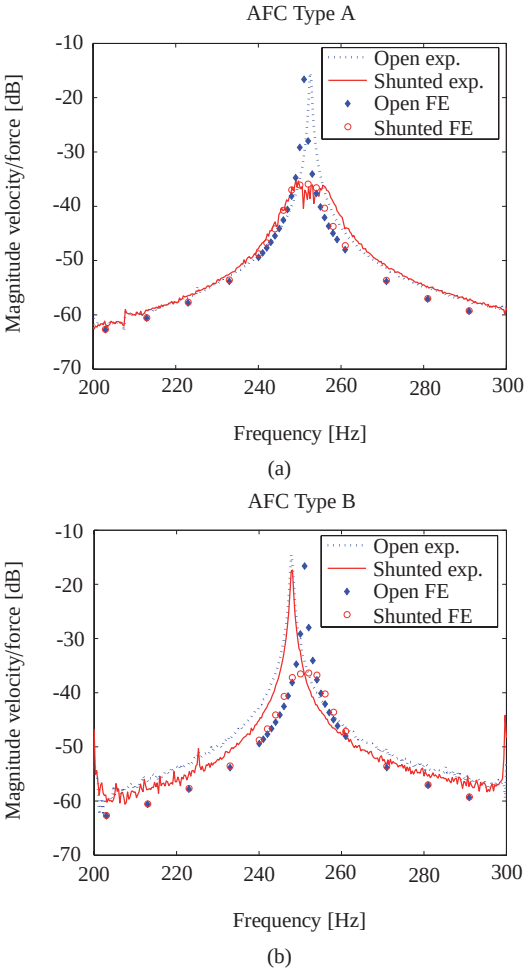

Figure 8.10: Magnitude of measured and simulated transfer-functions $G_v(s)$ from disturbance to tip velocity of the structure for the open system ($\cdots$ and ♦, respectively) and for the shunted system (— and ○ respectively); (a) AFC Type A, (b) AFC Type B.

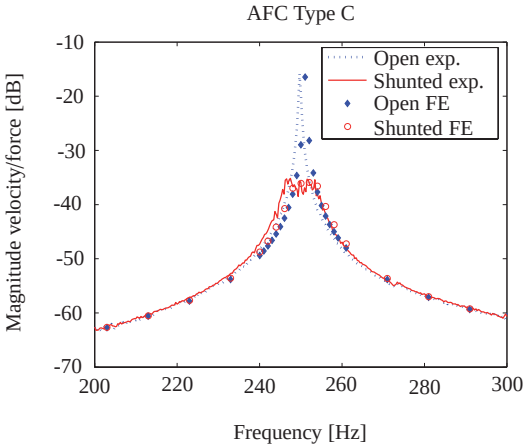

(a)

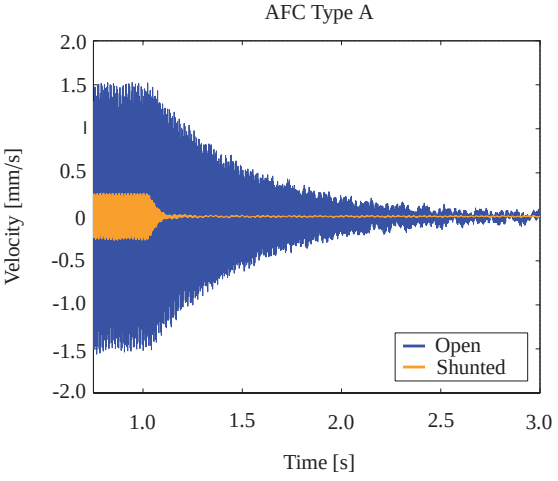

(b)

Figure 8.11: Magnitude of measured and simulated transfer-functions $G_v(s)$ from disturbance to tip velocity of the structure for the open system (··· and ♦, respectively) and for the shunted system (— and ○ respectively), AFC Type C; (b) measured sine-decay for AFC Type A for the open (—) and shunted system (—), respectively.

Table 8.8: Vibration suppression performance of different piezoelectric patches. Measured and predicted vibration reduction values, vibration levels are compared.

Patch	Actuation Mode	Active Volume [mm^3]	Vibration Reduction [dB]		Vibration Level [dB]	
			Measured	Predicted	Measured	Predicted
QP10N	3-1	236.9	20.08	20.27	-39.21	-40.09
QP10Ni	3-3	236.9	21.20	22.49	-38.67	-36.64
AFC Type A	3-3	150.3	19.77	19.40	-35.21	-35.73
AFC Type B	3-3	150.3	-	19.83	-	-36.16
AFC Type C	3-3	150.3	19.29	19.42	-35.16	-35.73

8.5.5 Damping

The damping of the second bending mode for open and shunt damped systems was measured by harmonically exciting the plate at the corresponding resonance frequency. After 1s, the excitation was switched off. The vibration decay is exemplarily presented in Figure 8.11 (b) for the aluminum plate with bonded AFC Type A patch.

8.6 Conclusions

Passive vibration damping was successfully implemented by shunting an *R-L* circuit to piezoelectric elements operating on the 3-3 effect. The need for very high inductance was overcome by implementing a synthetic impedance circuit. Characterization of the inherent piezoelectric capacitance as a function of temperature showed distinct behavior for piezoelectric ceramic elements working in 3-1 and 3-3 modes. The active fiber composite (AFC) configuration has a large influence on the resulting device capacitance values. An adaptation algorithm for tuning the inductance L is needed due to significant relative capacitance changes in the temperature range of interest. A real-time tracking of optimum inductance was implemented by means of the relative phase adaptation. Effective piezoelectric stress coefficients were computed along with effective stiffness coefficients by means of FE analysis for representative volume elements (RVEs) of different piezoelectric ceramic patches. Vibration suppression was predicted by analyzing the passive structure, the bonded active patch, and the shunted circuit within an integrated FE model. Numerical simulations showed excellent agreement with experimental results, accurately predicting both eigenfrequencies and vibration suppression levels. The proposed procedure represents an effective tool for the design and optimization of active structures. Accounting for their reduced active volume, AFC patches achieved equivalent vibration suppression performance per active unit volume as the monolithic actuator working in 3-1 mode. Simultaneously, they outperformed the monolithic 3-3 actuator. A weighty drawback of 3-3 actuated patches is their low inherent piezoelectric device capacitance. The

very large inductances required for tuning the resonant shunt to low structure eigenfrequencies have to be synthesized. An external power supply is therefore needed. Enhanced performance could be expected for active vibration control, because AFC were originally designed for high field regime applications. However, low inherent piezoelectric device capacitance is unfavorable for charge control, which is normally implemented in order to reduce hysteretic piezoelectric response. Slightly larger inherent piezoelectric capacitance values can be achieved by tailoring the AFC configuration. Above-mentioned disadvantages, along with today's prohibitive manufacturing cost for AFC limit their field of application. Summarizing, monolithic actuators operating on the 3-1 piezoelectric effect seem to be the best for use in *R-L* shunting. The present findings provided a solid basis for the selection process of the piezoelectric modules for the test object described in Chapter 10.

Chapter 9

Optimum Placement of Piezoelectric Ceramic Modules

The work presented in this Chapter can be found with minor modifications as a publication in the scientific literature as:

A. Belloli and P. Ermanni. Optimum Placement of Piezoelectric Ceramic Modules for Vibration Suppression of Highly Constrained Structures. *Smart Materials and Structures*, 16(5):1662-1671, 2007.

The vibration suppression efficiency of so-called shunted piezoelectric systems is decisively influenced by the number, shape, dimensions and position of the piezoelectric ceramic elements integrated into the structure. This chapter presents a procedure based on evolutionary algorithms for optimum placement of piezoelectric ceramic modules on highly constrained lightweight structures. The optimization loop includes the CAD software

CATIA V5, the FE package ANSYS and DynOPS, a proprietary software tool able to connect the Evolving Object library with any simulation software that can be started in batch-mode. A user-defined piezoelectric shell element is integrated into ANSYS 9.0. The generalized electromechanical coupling coefficient is used as the optimization objective. Position, dimension, orientation, embedding location in the composite lay-up and wiring of customized patches are determined for optimum vibration suppression under consideration of operational and manufacturing constraints, such as added mass, maximum strain and requirements on the control circuit. A rear wing of a racing car is investigated as the test object for complex, highly constrained geometries.

9.1 Introduction

The vibration suppression performance in both active and passive damping decisively depends on the number, shape, size and location of the used piezoelectric ceramic elements [173, 174]. The same holds for shape control, vibroacoustic control and structural health monitoring. Depending on the complexity of the structure at hand, analytic or numerical models might prove more appropriate to describe its behavior. A number of different objective functions, design variables, constraints and solution methods can be applied for the optimization of a target application.

The following section reviews a representative portion of the work performed in the last decade towards the optimal placement of sensors and actuators for vibration suppression. The papers reviewed here have been classified based on the optimization algorithm used and on the kind of structure investigated.

9.1.1 Parameter Variation

Informal optimization consisting of parameter variation studies can deliver useful insight into the optimization task, in particular if the solution space can be explored with a reasonable number of configurations. This is the case for simple structures such as beams.

While investigating the multiple mode passive vibration suppression with piezoelectric materials and resonant shunts, Hollkamp [175] estimated the generalized electromechanical coupling coefficient of a pair of piezoelectric ceramic tiles attached to a cantilevered beam at different locations. Kang *et al.* [176] optimized the placement of piezoelectric co-located sensor/actuator pairs for active vibration control of laminated beams by maximizing the structural damping index, a weighted sum of the achieved modal damping of each vibrational mode. Parametric studies were presented for the damping ratio as a function of the location of piezoelectric ceramic elements with given length and various outer-layer fiber orientations. The damping and the stiffness of the adhesive layer and the piezoceramics are taken into account.

Formal optimization techniques, on the other hand, can be classified into mathematical programming and stochastic methods.

9.1.2 Mathematical Programming

Most mathematical programming methods work locally and are very efficient given that the assumptions on continuity, differentiability and convexity of the solution space are satisfied. Aside from the convexity assumption, this is mostly the case for basic structures such as beams, plates and shells.

Beams

Li *et al.* [177] published an optimal design methodology for piezoelectric ceramic actuators/sensors and feedback gains towards the vibration suppression in flexible structures. The influence of the actuator/sensor pairs on the mass and stiffness properties of the composite structure was taken into account. The proposed composite objective function included the control performance as well as the added mass. The gradient based optimization, applied to the simple case of a beam structure, was prone to getting trapped in local optima.

Plates and Shells

Kang *et al.* [178] carried out a similar investigation on laminated plates; as in the work previously described, the optimization was carried out using the gradient method. Seeger and Gabbert [179] proposed an optimization algorithm for the optimal positioning of co-located actuator/sensor patch pairs on a simply supported plate structure. The conjugate gradient method is applied to minimize the H_2-Norm of the transfer function between an external excitation disturbance and the plate vibration amplitude. The constrained optimization algorithm uses the augmented Lagrangian function in order to avoid patch overlapping. Sun *et al.* [180] determined optimal locations of piezoelectric ceramic sensor elements discretely distributed on a rectangular plate by minimizing the observation spillover of quasi-modal sensors. This is equivalent to minimizing the maximum eigenvalue of the matrix relating the sensors' output charges to the modal coordinates. The authors formulated a similar criterion for optimal placement of the piezoelectric ceramic actuator elements based on energy and control spillover considerations. Sun and Tong [181] extended the investigation to simply supported closed- and open-form shell structures. In [182], Kim and Kim address the optimal distribution of an active piezoelectric layer on a flexible plate. A desired performance in transient vibration control is achieved at minimum control energy. Spatial design variables, previously shown to work well for the optimal distribution of viscoelastic damping layers [183], define the optimum distribution of the layer. A gradient based optimization algorithm yielded optimal material coverage for single mode and multiple mode suppression. Local optima were avoided by sequential increase of the number of spatial design variables. These are independent from the finite element mesh. Modal based correction methods were applied by Rose [184] for the placement of piezoelectric ceramic modules on a circular plate. These methods allow the negotiation of changes introduced by the piezoelectric element's mass and stiffness. The generalized electromechanical coupling coefficient was maximized by applying gradient based methods in a two-step approach. Halim and Moheimani [185] suggested a criterion for the optimal placement of co-located piezoelectric ceramic actuator/sensor pairs on a thin plate using modal and spatial controllabil-

ity. The spatial controllability was used to find the optimal placement of co-located actuator/sensor pairs for effective average vibration reduction over the entire structure, while maintaining modal controllability and observability of selected vibration modes.

Engineering design problems, however, are often of a discrete nature (e.g. the number of actuators) or present non-convex objective functions, so that the above methods are not applicable or tend to get trapped in local optima. In order to overcome these limitations, the scientific community has put significant effort into the investigation of stochastic optimization methods.

9.1.3 Stochastic Methods

Stochastic optimization methods can handle search spaces involving both discrete and continuous domains, non-convex objective functions [186], and objective functions or constraints lacking differentiability. A drawback is that stochastic search methods are often computationally expensive.

Truss Structures

Due to their discrete nature, actuator placement problems on truss structures are classic examples for the application of stochastic optimization methods.

To our knowledge, Rao and Pan [187] were the first to apply genetic algorithms to the problem of optimal actuators placement in an actively controlled two-bay truss. The dissipation energy of the active controller was maximized for a fixed number of three actuators. A strategy for determining the optimal number of actuators and their respective locations in the active vibration control of a seventy-two-bar space truss was presented by Yan and Yam [188]. The eigenvalues of the energy correlative matrix of the input control force are used to determine an optimal number of actuators for vibration control. Depending on the desired controllability level, these can be equal to or less than the number of degrees of freedom to be controlled. The corresponding optimal actuator locations are then identified by minimizing the eigenvalue sum of the correlative matrix of

the required control input energy. Using a binary-encoded genetic algorithm, Bishop and Striz [189] demonstrated the optimal placement of passive ideal viscous dampers on space trusses subjected to different loading. The kinetic and strain energy remaining in the system at the end of a full time-domain transient analysis, as well as the number of actuators, were combined to form a penalty function. Richardson and Abdullah [190] used a real-encoded genetic algorithm for optimal placement of sensors and active tendon mechanisms on high-rise civil structures. These are susceptible to vibrations due to earthquakes, hurricanes, or other abnormal loads such as explosions. The proposed method allows for the simultaneous determination of the optimal controller gains.

Even for basic structures, stochastic methods show their strength in mastering non-convex objective functions and discrete parameters, e.g. while choosing from a list of piezoelectric modules with given sizes.

Beams

Results by Gaudenzi *et al.* [191] provided insight into the problem of optimal placement, sizing, and loading of piezoelectric actuators for damping beam vibrations. A fundamental solution, formulated for a single piezoelectric actuators pair, was used in the framework of a genetic algorithm optimization. A float-encoded genetic algorithm for the integrated optimization of piezoelectric actuator and sensor locations and feedback gains for active vibration control was introduced by Zhang *et al.* [192]. According to their results, the float-encoded genetic algorithm is less likely to become trapped in local minima compared to the adaptive binary genetic algorithm and converges faster to the solution. A cantilevered beam is presented as an optimization example, for which the performance function is based on maximizing the dissipation energy of the active controller. A similar problem is tackled by Yang *et al.* [193], where the sizes of the sensors/actuators to be bonded on a cantilevered beam are selected by the genetic algorithm from a prescribed patch pool. Position and feedback gains are optimized simultaneously. Again, the maximization of the energy dissipation was selected as the optimization criterion.

Plates and Shells

The same authors later extended the method cited above to the investigation of plates and cylindrical shells [194]. Dynamic constraints, included directly in the modified real-encoded genetic algorithm, penalize overlapping piezoelectric patches. Genetic algorithms were used by Han and Lee [195] to find efficient locations for six sensors and two actuators out of ninety-nine possible sub-areas on a cantilevered composite plate. The performance criteria, used for finding the optimal locations of piezoelectric sensors and actuators and preventing spillover, consider the eigenvalues of the steady state observability and controllability grammians, respectively. Two criteria for the optimal placement of piezoelectric actuators for vibration control were suggested by Sadri *et al.* [196] using modal controllability and the controllability grammian. The number of actuators, their sizes and their optimal locations for maximum controllability of isotropic plates were determined using genetic algorithms. The authors later applied the modal controllability as a criterion for optimal placement of piezoelectric actuators for panel flutter suppression [30]. Again, the optimal locations were found by applying genetic algorithms. Quek *et al.* [197] used the classical direct pattern search method to maximize the active damping of a laminated composite plate. The starting point for the pattern search is selected based on the maxima of integrated normal strains consistent with the size of the co-located piezoelectric sensor/actuator pair used. Optimization performance indices are based on modal and system controllability. The positions of four piezoelectric patches for adaptive feed-forward control are chosen out of sixty-four candidate locations on a cantilevered aluminum plate in [198]. The maximization of the controllability grammian through genetic algorithm guarantees a minimum control force for minimizing the vibration response at three selected points of the plate. The required mode shapes and the coupling matrix relating the applied voltages and the equivalent nodal forces are computed via Finite Element Analysis, thus making the method viable for more complex structures. Inspired by the latest progress in laser cutting and micromachining techniques, Wang *et al.* [199] determined the optimal topology of both isotropic and anisotropic piezoelectric sensor/actuator pairs for torsional vibration control of a lam-

inated composite plate using a binary-encoded genetic algorithm. The checkerboard problem is prevented by connectivity analysis, making the method superior to homogenization-based methods. Optimal placements and sizes of sensors and actuators attached to an inflated torus were found by Jha and Inman [200] using a binary-encoded genetic algorithm. Performance indices were defined using modal controllability (minimum energy requirement) and observability (maximum output energy for a good signal-to-noise ratio).

Complex Structures

The behavior of more complex lightweight structures can be investigated by idealizing their components as rods, beams, plates, or shells. The formulation of the assembled model, however, can be a task beyond the engineer's means, both in terms of expertise and time constraints. Arbitrary, real-world structures are highly constrained by functional, manufacturing, or esthetic demands and often present non-convex, noisy solution spaces. This makes the use of stochastic methods in combination with modern knowledge-based CAD systems and FEA tools particularly favorable. Yan and Ghasemi-Nejahd [201] determined the optimal configuration of piezoelectric ceramic actuators/sensors embedded in an adaptive circular composite plate with one central and three edge supports. Genetic algorithms were used to find the optimal actuator configuration placement among eight possible configurations taking into account the interactions between the controller and the structure. Damaren [202] addressed the problem of actuator/sensor location of a single piezoelectric ceramic element in a spacecraft box structure having a tray-stack architecture. Contributions of the piezoelectric ceramic elements to the system's mass and stiffness were neglected. Assuming patch dimensions equal to the meshed finite element reduced the problem of optimal location for maximum injected damping into the first few modes to a discrete enumeration of a relatively small number of possibilities. One could imagine to solve the same problem without loss of generality by applying the procedure described in the present article. Our work focuses on the optimum piezoelectric ceramic element placement on real-world structures for vibration suppression via passive

shunt damping. The procedure combines a knowledge-based CAD system, a FEA tool and Evolutionary Algorithms (EA) [97] as optimization framework. As such, it represents a further step towards a comprehensive procedure for the optimization of both actuators' and sensors' locations and controller parameters under consideration of structural, weight penalty, manufacturing and economical constraints.

For the sake of conciseness, we refrain from elaborating on basic concepts of EA and confine ourselves to a brief description of the application of evolutionary optimization methods to the vibration suppression problem. The interested reader will find more detailed information on EA in [97, 203, 98, 99].

9.2 Evolutionary Optimization Methods Applied to the Vibration Suppression Problem

Figure 9.1 illustrates a general working schedule for placement optimization problems addressed with an evolutionary approach. Before evolutionary algorithms can be used for the optimization of any part with bonded or embedded piezoelectric ceramic elements, some preparatory steps have to be carried out. First, a simulation model of the active structure to be optimized is required in order to evaluate the fitness value for each individual. A CAD-model of the structure at hand is prepared using the CAD-software CATIA V5[1]. It defines the geometric shape of the structure (Figure 9.2), including the bonded or embedded piezoelectric ceramic patches. A finite element (FE) model is derived from the CAD-model and exported to ANSYS[2], the software package used to evaluate the influence of the piezoelectric ceramic modules onto the system. Shell elements are appropriate for the simulation of thin-walled lightweight structures. In the scope of the present study, SHELL 181 elements were used for the layered composite parts. Additional user-defined shell elements - developed at the Institute of

[1] www.catia.ibm.com
[2] www.ansys.com

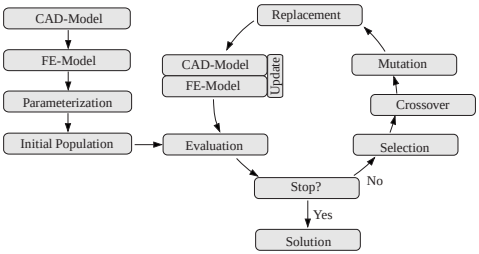

Figure 9.1: Working schedule of evolutionary algorithms applied to placement optimization problems.

Composite Structures and Adaptive Systems at DLR Braunschweig [135] - simulate the coupling behavior of the piezoelectric ceramic patches.

After defining the simulation model, the optimization process can be set up. The so-called parameterization is the key to an efficient and successful optimization. It has to be defined which parameters, e.g. shape and position of a certain piezoelectric ceramic module, are modified during the optimization process. The number of optimization parameters defines the size of the genotype and accordingly the size of the search space. A large number of parameters expands the search space and generally requires a greater number of evaluations to explore it sufficiently, before eventually converging to an optimum solution. The last task to be accomplished before starting the optimization process is the definition of the evaluation step, described in some detail in Section 9.3. Starting from a randomly initialized population, the optimization loop containing evaluation, selection, crossover, mutation, replacement and model update is iteratively run until a given stopping criterion is satisfied and an optimum design solution is found. A proprietary software tool called DynOPS (Dynamic Optimization Parameter Substitution) written in C++ copes with the complex task of managing the optimization loop. For more detailed information on DynOPS, the interested reader is referred to Wintermantel [98].

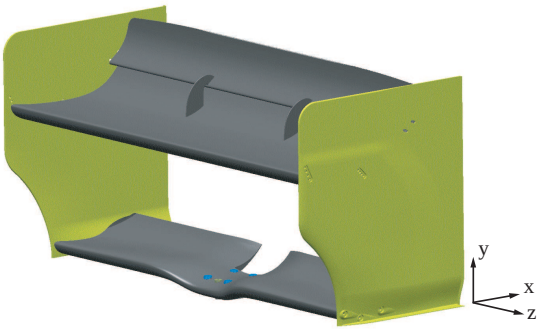

Figure 9.2: The rear wing of a racing car, investigated as the test object for complex, highly constrained geometries.

9.3 Optimization Process

Based on the FE model of the structure at hand, the optimization process is set up by defining the model parameterization and introducing a fitness formulation for rating the evaluated individuals. First, the actuators' configuration is optimized for maximum vibration suppression using an *R–L* shunt. Subsequently, an Active Fiber Composite sensor is positioned for proper operation of a switching *R–L* shunt [152, 204] and a Positive Position Feedback (PPF) control [205], respectively.

9.3.1 Actuators' Optimization

Parameterization

The parameterization links the search space (genotype) to the solution space (phenotype). The geometric shape and the lay-up of the structure to be damped are fixed. The following parameters define the positioning of the piezoelectric ceramic actuators with variable dimensions, simulta-

neously on both rear wing endplates (Figure 9.3):

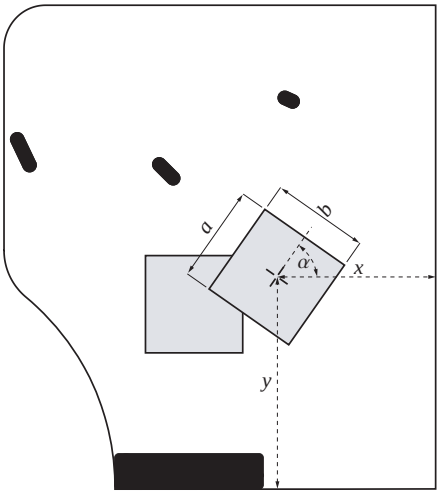

Figure 9.3: Endplate with two overlapping piezoelectric ceramic elements. The black-filled areas represent assembly inserts to be avoided by the patches.

- Patch length a
- Patch width b
- Horizontal position x
- Vertical position y
- Angle of rotation α
- Embedding location in the composite lay-up
- Patch wiring

Considering two patches, this represents a total of thirteen optimization parameters. For the presented case, the population size was chosen to be approximately four times the number of optimization parameters.

A first hard constraint is enforced directly while updating the CAD-model. Patches overlapping assembly inserts on the endplate (see the black-filled areas in Figure 9.3) or crossing the endplate's boundary are discarded. A soft constraint - penalizing the individual proportionally to the violated area - did not show any improvement in convergence behavior over the hard constraint. Skipping building and evaluation of the FE-model represents a considerable saving in computing time.

Fitness Function

Addressing the vibration suppression of a selected n^{th} mode, the optimization objective is based on the generalized electromechanical coupling coefficient K_{ij} proposed by Hagood and von Flotow [142] (see Equation 8.3). The generalized electromechanical coupling coefficient is proportional to the fraction of the system modal strain energy which is converted into electrical energy by the open-circuit piezoelectric ceramic element bonded onto or embedded into the structure. As such, it is a direct measurement of a shunted piezoelectric ceramic element's influence on a system. A number of constraints take operational and manufacturing limitations into account:

- Maximum added mass m_a
- Maximum strain $\epsilon_{z,max}$ experienced by the patches
- Required inductance value L^* for proper operation of the *R–L* and switching shunts
- Required quality factor Q for proper operation of the *R–L* and switching shunts

The tuning inductance L^*, the optimum resistance R^* (both according to [142]) and the quality factor Q are computed as

$$L^* = \frac{1}{\omega_n^2 \left(1 + K_{ij}^2\right) C_p} \text{ and } R^* = \frac{\sqrt{2}\frac{K_{ij}}{1+K_{ij}^2}}{\omega_n C_p},$$
$$Q = \frac{\omega_n L^*}{R^*}, \tag{9.1}$$

where ω_n denotes the structure resonance to be damped and C_p is the inherent piezoelectric capacitance.

The optimization objective and all constraints are mapped to a single fitness value $F(\mathbf{p})$ to rate the quality of every evaluated individual - represented by the parameter vector $\mathbf{p}$ - by building a weighted sum of the form

$$F(\mathbf{p}) = \sum_i w_i D_i(\mathbf{p}), \tag{9.2}$$

where D_i represents the rating for the objective or a specific constraint and w_i is the corresponding relative weight. The mapping is done in order to assign a fitness portion to each constraint in the interval [0,1]. Only the optimization objective is allowed to exceed this range for low quality individuals. The contribution of the single fitness portions to the overall fitness value can be controlled by defining the relative weights w_i. For the present optimization, the relative weights are left to unity. The optimization is a minimization problem where the absolute minimum of the fitness $F(\mathbf{p})$ should be found. Objective and constraint mapping functions were implemented as introduced by König [99].

Optimization Objective

The mapping function for the optimization objective, i.e. the maximization of the generalized electromechanical coupling coefficient for the selected mode, is generally formulated as

$$D_i(O) = (aO + b)^\alpha, \tag{9.3}$$

where O is the generalized electromechanical coupling coefficient to be maximized. The choice of the exponential factor $\alpha = 5$ is based on experience, and a and b are scaling factors defined by the conditions

$$\begin{aligned} D_i(O = O_{init}) &= 1 \\ D_i(O = O_{estim}) &= 0.1, \end{aligned} \tag{9.4}$$

where O_{init} represents an initial value of the design objective that should result in a fitness value of 1 (set to $1.5 \cdot 10^{-2}$ in the present case). O_{estim} is the estimated value that is expected to be reached through the optimization process corresponding to a fitness value of 0.1. In the cited case, this value is set to $8 \cdot 10^{-2}$. Figure 9.4 illustrates a portion of the mapping function for the optimization objective leading to fitness values in the interval $[0,\infty[$. Defining the mapping function for the optimization objective, O_{init} and O_{estim} influence its steepness in the range of interest and, consequently, the evolutionary pressure that the algorithm applies on the optimization objective. In several runs of the same optimization, different O_{init} and O_{estim} values had negligible influence on the optimization results, but showed distinct behavior in convergence speed. O_{init} can be estimated as the best value of the initialization generation. Should the optimization algorithm find solutions with better objectives than O_{estim}, its value can be iteratively adjusted to maintain enough evolutionary pressure on the optimization objective.

Constraints

The mapping functions of all constraints are implemented using smooth step functions to keep solutions with values falling slightly above the respective limit in the population. The definition of these mapping functions is

$$D_i(C) = \frac{1}{1 + e^{-\lambda(C(\mathbf{p}) - C_{limit} - \Delta)}}, \tag{9.5}$$

Table 9.1: C_{limit} and C_{feas_tol} values for the different constraint mapping functions.

Constraint		C_{limit}	C_{feas_tol}
m_a	[kg]	$8.7 \cdot 10^{-2}$	$8.7 \cdot 10^{-3}$
$\epsilon_{z,max}$	[-]	$1.5 \cdot 10^{-3}$	$5 \cdot 10^{-4}$
L^*	[H]	10	10
Q	[-]	10	10
VMR	[-]	1.5	-0.25

where following functions define the parameters λ and Δ:

$$\begin{aligned} \lambda &= \frac{1}{C_{feas\_tol}} \left(ln\left(\frac{1}{D_{limit}} - 1\right) - ln\left(\frac{1}{D_{feas}} - 1\right)\right) \\ \Delta &= \frac{1}{\lambda} ln\left(\frac{1}{D_{limit}} - 1\right). \end{aligned} \tag{9.6}$$

The shapes of the mapping functions were adjusted by adapting the values C_{limit} and C_{feas_tol} (Table 9.1), resulting in:

$$\begin{aligned} D_{limit} &= D_i(C = C_{limit}) = 0.01 \\ D_{feas} &= D_i(C = C_{limit} + C_{feas\_tol}) = 0.5. \end{aligned} \tag{9.7}$$

Figure 9.5 exemplarily depicts the resulting mapping function for the maximum strain upper limit constraint $\epsilon_{z,max}$. The width and steepness of the mapping functions are critical parameters for the convergence of the optimization process.

9.3.2 Sensor Optimization

After determining the actuators' configuration showing the largest generalized electromechanical coupling coefficient K_{ij} under consideration of all constraints, the sensor configuration is optimized for proper operation of

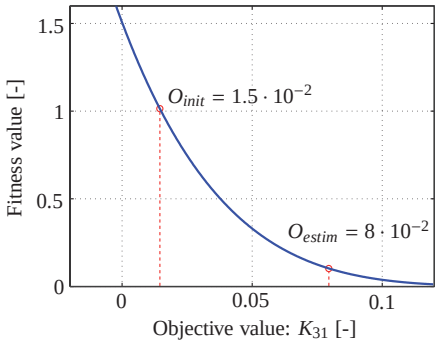

Figure 9.4: Mapping function for the optimization objective.

the switching *R–L* shunt, i.e. co-local actuator-sensor configuration [20]. This also holds for a Positive Position Feedback (PPF) controller [205].

Parameterization

Again, the geometric shape and the lay-up of the structure to be damped are fixed. The best actuators' configuration resulting from the previous optimization is adopted. In fact, this can be assumed to be optimal for both the *R–L* and the switching *R–L* shunts. The sensor itself is positioned by variation of:

- Horizontal position x
- Vertical position y
- Angle of rotation α

Sensor length (31mm) and width (20mm) are fixed due to manufacturing reasons. The sensor is embedded under the outer skin layer.

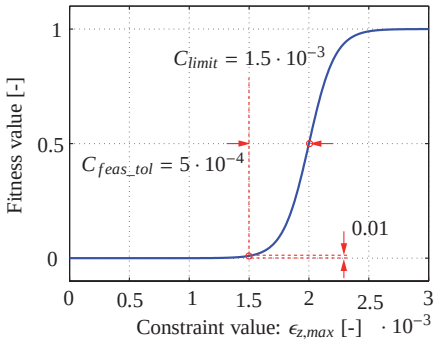

Figure 9.5: Mapping function for the maximum strain upper limit constraint $\epsilon_{z,max}$.

Fitness Function

Harmonic analysis yields the phase response of both actuator (φ_a) and sensor (φ_s) voltage signals. The Average Phase Deviation (*APD*) in the vicinity of the eigenfrequency addressed was taken as the design objective:

$$APD = \frac{\sum_{\omega=\omega_n-\Delta\omega}^{\omega=\omega_n+\Delta\omega} (\varphi_s(\omega) - \varphi_a(\omega))}{m} \cdot 100 \tag{9.8}$$

where $\Delta\omega$ is the frequency range of interest around ω_n and m is the number of samples. The initial and the estimated values of the design objective are set to 1.5 and 0, respectively.

For proper operation of the autonomous switching *R–L* shunt, the voltage magnitude delivered by the sensor module should be larger than that produced by the actuators. Accordingly, the following constraints were considered:

- Ratio *VMR* between the magnitude of the sensor's and actuators' voltage signals at $\omega = \omega_n$

Table 9.2: Optimizations' facts.

	Actuators	Sensor
# of parameters	13	3
Population size	50	8
# of generations	165	25
Cross-over probability	0.8	0.8
Mutation probability	0.4	0.4

- Maximum strain $\epsilon_{z,max}$ experienced by the sensor

Again, the sensor module was not allowed to overlap regions including inserts. Table 9.2 summarizes the number of parameters, population size, number of generations until convergence, and probabilities used for the cross-over and mutation operators.

9.4 Optimization Results

9.4.1 Actuators' Optimization

An actuator pair is searched that maximizes the generalized electromechanical coupling coefficient under consideration of a number of constraints, listed in Section 9.3.1. The best configuration found by the optimization engine is presented in Figure 9.6, with both monolithic actuators working in the indirect 3-1 mode and being galvanically coupled on each endplate. Table 9.3 summarizes the proposed parameter values and the resulting performance. The added mass is approximately 1% of the original rear wing mass. Figures 9.9 to 9.11 illustrate the evolution of the fitness value $F(\mathbf{p})$, the design objective K_{31} and the maximum strain constraint $\epsilon_{z,max}$, respectively. In a first search phase, the algorithm rapidly finds a number of configurations with increasing performance and moves the patches to a region of higher strains, finding a local optimum that only slightly violates the maximum strain constraint (see Figure 9.11). After several generations, an

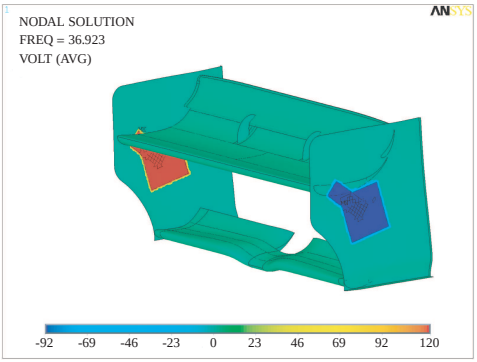

Figure 9.6: Voltage distribution for the 1^{st} vibration mode. The electrodes are galvanically coupled on each endplate.

individual is found through mutation in another region of the search space, whose configuration performs better despite experiencing higher strains. Again, the algorithm seeks its way towards a new local optimum, moving within a noisy solution space showing large variations in maximum strain.

Another mutation delivers the optimum configuration for the optimization run discussed here, finding an individual with lower mass that experiences lower maximum strain while showing enhanced piezoelectric coupling. Despite the rather complex geometry and boundary conditions, the orientation of the larger actuator with respect to the fiber direction of the adjacent unidirectional layers (12° to the y-axis) closely matches the results for maximum modal damping reported by Kang *et al.* [176]. The optimization run was stopped after 165 generations. Further slight improvements can be expected by computing a larger number of generations.

As discussed in this example, the evolutionary procedure presented in this article is robust against getting trapped into local minima. It is assumed that a sufficient number of evaluations would lead to a solution near the overall optimum. However, to the knowledge of the authors there exists no mathematical proof for convergence of the solution to a global minimum.

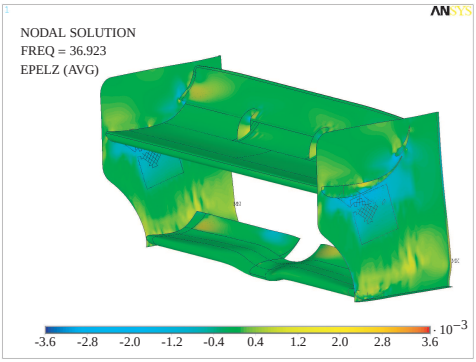

Figure 9.7: Strain distribution for the 1^{st} vibration mode.

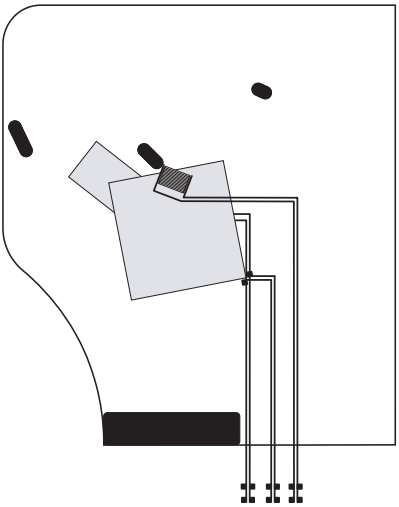

Figure 9.8: Endplate showing the best configuration found by the optimizer.

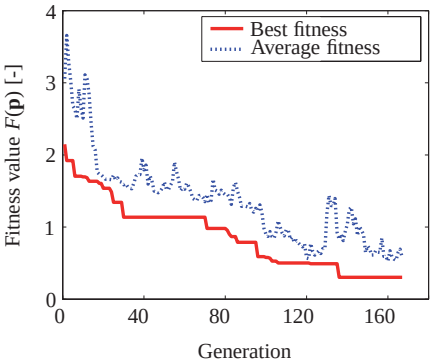

Figure 9.9: Convergence plot of the fitness value $F(\mathbf{p})$.

9.4.2 Sensor's Optimization

Given the optimum actuator pair found in the previous section, a co-local sensor is searched. The sensor configuration showing minimum Average Phase Deviation in the vicinity of the eigenfrequency addressed is found near the upper middle insert. Despite experiencing relatively low strains, the AFC sensor working in 3-3 mode delivers a voltage signal, the magnitude of which is approximately 1.5 times larger than the actuators' one (see Table 9.3).

Figure 9.8 shows the actuators and sensor placement on the endplate. The partially overlapping actuators are embedded between different laminate layers in a region of relatively high strains (see Figure 9.7) and accurately avoid the inserts regions. The sensor is embedded in the opposite skin of the sandwich part.

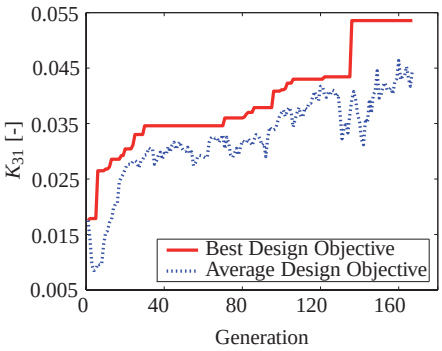

Figure 9.10: Convergence plot of the generalized electromechanical coupling coefficient K_{31}.

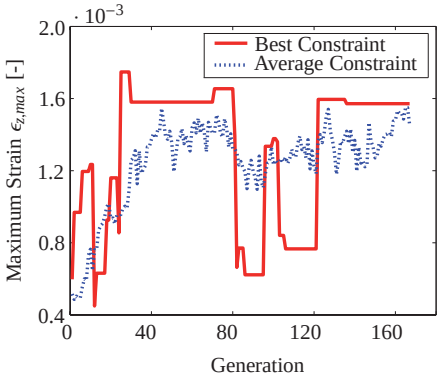

Figure 9.11: Convergence plot of the maximum strain constraint $\epsilon_{z,max}$.

Table 9.3: Optimizations' results. Values in parenthesis were defined as fixed.

		1^{st} actuator	2^{nd} actuator	Sensor
Patch length a	[mm]	51	136	(31)
Patch width b	[mm]	133	137	(20)
Horizontal position x	[mm]	300	246	251
Vertical position y	[mm]	281	239	300
Angle of rotation α	[°]	142	102	69
Embedding location		ply 1/2	ply 2/3	(ply 1/2, opposite side)
Patch wiring		galvanically coupled		-
Coupling coefficient K_{31}	[-]	$7.10 \cdot 10^{-2}$		-
Optimum inductance L^*	[H]	6.92		-
Optimum resistance R^*	[Ω]	160.87		-
Optimum quality factor Q	[-]	9.99		-
Added mass m_a	[kg]	$5.77 \cdot 10^{-2}$		$1.53 \cdot 10^{-3}$
Maximum strain $\epsilon_{z,max}$	[-]	$1.53 \cdot 10^{-3}$		$3.82 \cdot 10^{-4}$
APD	[°]	$4.79 \cdot 10^{-3}$		
VMR	[-]	1.52		

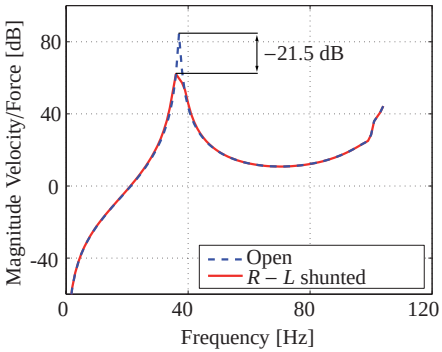

Figure 9.12: Magnitude of the transfer-function from disturbance to velocity of the endplate tip: open and shunted systems, respectively.

9.4.3 Vibration Suppression

For prediction of the vibration suppression performance of the $R^* - L^*$ shunted optimum actuator pair, the transfer-function from a unit excitation (applied on the endplate in correspondence to the rear wing's center of mass) to the endplate tip displacement was computed in the Laplace domain as described in Chapter 8. Results for the open and the shunt damped rear wing are shown in Figure 9.12. A vibration suppression of the first vibration mode by approximately 21.5 dB can be expected.

9.5 Conclusions

In this Chapter an approach is presented for optimum placement of piezoelectric ceramic elements for vibration suppression of real-world, highly constrained structures. The optimization procedure includes a knowledge-based CAD-model, an FE-model and an Evolutionary Algorithm optimization loop controlled by the proprietary software tool DynOPS. A user-defined layered shell element with piezoelectric capabilities was integrated in the commercial FE-package ANSYS for simulation of the composite structure's dynamic response. The generalized electromechanical coupling coefficient was computed as the design objective. Additional constraints were then added to form a unique fitness value. The model parameterization allows for the investigation of an arbitrary number of patches with variable dimensions, position, orientations, embedding location in the composite lay-up and wiring between the different patches. A rear wing of a race car was investigated as a test object for the proposed optimization procedure. Two monolithic actuators and an AFC sensor were successfully placed for optimum vibration suppression using *R–L* and switching *R–L* shunts. The results were experimentally verified as described in Chapter 10.

The FE-model can be enhanced to take into account the influence of the chosen active/passive controller on the composite structure. Material and geometrical variations of both the host structure and the piezoelectric elements can easily be included as optimization parameters. Additional constraints such as control energy, influence of embedded elements on the structure's mechanical behavior, manufacturing or economical issues can also be mapped to a single fitness value. The computational requirements, however, could then be the limiting factor.

Chapter 10

Test Object: Integration of Smart Technologies in a Rear Wing of a Racing Car for Structural Vibration Control

In this last Chapter the methods and technologies developed as reported in the previous Chapters were applied to a test object. The suppression of structural vibrations by means of piezoelectric ceramic elements and passive electrical networks was investigated and tested on a rear wing of a racing car. Their performance was compared to the performance of an active PPF controller. In the scope of the study, the natural frequency of the test object was increased by use of HM graphite fibers. Embedding strategies, encapsulation techniques and wiring concepts for customized prototype sensors and actuators, described in Chapters 6 and 7, were successfully applied. The positions for two monolithic actuators and one AFC

sensor were optimized as described in Chapter 9. The FE model, however, didn't model the rear wing assembly accurately enough to predict the actual strain distribution of the natural mode. The electromechanical coupling of the actuators is therefore insufficient to suppress the related vibration, be it by active of passive means. A sub-optimal vibration suppression is, however, achieved for the flutter mode of the endplate's trailing edge. The passive *R–L* shunt reduces the vibration by 12.5 dB or 76% and the active PPF controller achieves a vibration suppression of 17 dB or 86%. The reported performance was achieved with an additional mass of less than 1%. It is advised to investigate the drag reduction potential of such a vibration suppression.

10.1 Test Object

After evaluation of different parts, the rear wing of a racing car was selected as the test object for this study. The relatively inexpensive manufacturing of smart endplates as well as the stand-alone character of the part were decisive arguments for the selection. The very low natural frequency represents an additional scientific challenge.

10.1.1 Identification

The test object was identified in order to gather useful information about eigenfrequencies, eigenmodes and strain distribution. Experiments were carried out both on a lab test bed at the Centre of Structure Technologies at ETH Zurich and on a 7-post rig that can simulate the dynamic loads on a race track. A Laser Doppler Scanning Vibrometer (LSV), accelerometers and strain gages were used. Experimental findings were compared to numerical results from an FE analysis. Table 10.1 reveals an excellent agreement between numerical and experimental results for selected, relevant eigenfrequencies and eigenmodes. These are presented in Figure 10.1. The first mode is likely to be excited by roughness and curbs of the race track. The remaining modes could be aerodynamically relevant. The displacement amplitude response of the rear wing is depicted in Figure 10.2

(a) for side excitement and Figure 10.2 (b) for front excitement, respectively.

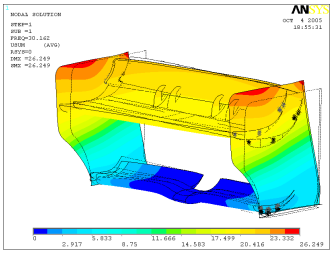

(a) 1^{st} mode

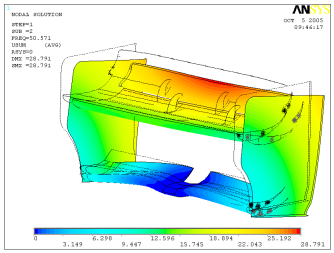

(b) 2^{nd} mode

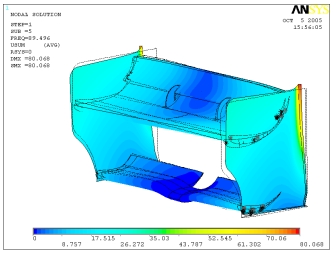

(c) 5^{th} mode

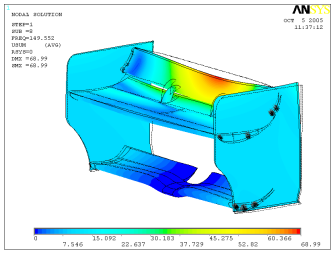

(d) 8^{th} mode

Figure 10.1: Displacement vector sum of selected relevant modes: (a) First vibration mode at 30.16 Hz, (b) Second vibration mode at 50.57 Hz, (c) Fifth vibration mode at 89.5 Hz, (d) Eighth vibration mode at 149.5 Hz.

Measurement on the 7-post rig confirmed the first vibration mode to be dominant for the rear wing mounted on the racing car. The acceleration amplitude response in Figure 10.2 (c) clearly shows the corresponding peak at 26.4 Hz. The strain gauges revealed a maximum strain during a simulated lap of approximately 0.02% on the lower mainplane and 0.01%

on the endplate, respectively.

Summarizing, the first vibration mode at approximately 28.5 Hz was found to be dominant for the rear wing displacement amplitude. This mode can be addressed by embedding shunted piezoelectric ceramic elements in the endplates, thus keeping manufacturing costs at a minimum. The strain distribution during operation is not expected to be critical.

10.1.2 Natural Frequency Increase

The lower the eigenfrequency, the larger the inductance required for tuning the shunt circuit to the mode to be damped (see Equation 8.1). For this reason, the advantage of using stiffer graphite fibers (Table 10.2) for laminating the endplates is self-evident. According to numerical results, the replacement of high tensile (HT) fibers by high modulus (HM) fibers is expected to increase the natural frequency by 19%, and reduce the required inductance by 36%.

Experimental testing showed an increase in rear wing's natural frequency from 28.5Hz to 35.5Hz (+24.6%) by replacing HT with HM graphite fibers for laminating the endplates (see velocity and displacement amplitude response in Figure 10.3). This reduced the inductance value required to tune the system to the natural frequency by 36%. Moreover, due to the use of HM graphite fibers, the trailing edge's flutter mode on the endplates has higher average relative velocity and displacement contributions compared to the natural mode . This was not the case for the original rear wing, where the natural mode was dominant.

Table 10.1: Numerical and experimental results for relevant vibration modes. Measurement carried out with the LSV.

Mode No.	Numerical Frequency [Hz]	Experimental Frequency [Hz]	Mode Shape
1	30.16	28.52	Parallelogram
2	50.57	50.61	Nodding around longitudinal wing axis
5	89.50	81.17	Flutter of top rear corner
8	149.55	163.30	Flap bending
9	179.93		

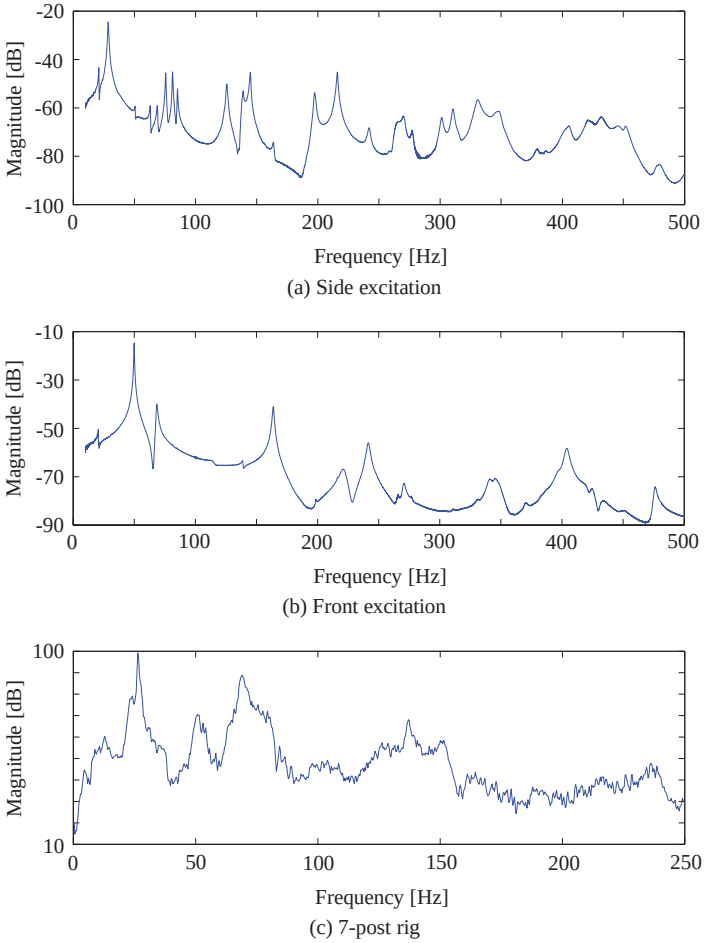

Figure 10.2: Response of the rear wing. (a) Input: electromechanical shaker at CoM, right endplate - Output: Displacement amplitude averaged over left endplate; (b) Input: electromechanical shaker at leading edge of upper mainplane - Output: Displacement amplitude averaged over flap; (c) Input: 7-post rig - Output: Acceleration amplitude response of the rear wing endplate's top rear corner.

Table 10.2: Expected natural frequency increase using high modulus graphite fibers, based on FEM-based modal analysis of the rear wing.

	HT fibers	HM fibers
Fibers of UD layers	T1000	M55J
Fibers of woven layers	T800	M46J
Predicted natural frequency [Hz]	30.16	37.26
Red. in required inductance	-	-36%

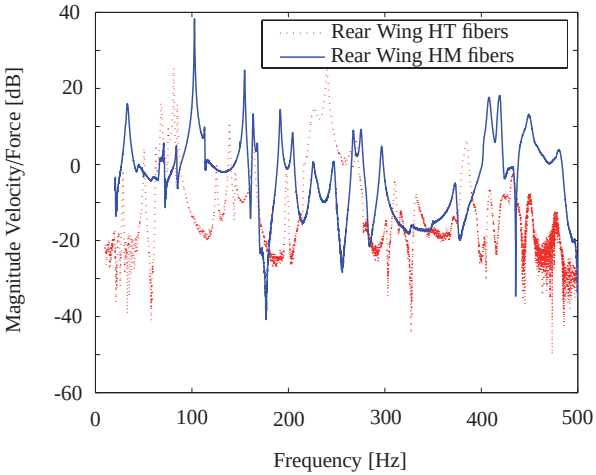

(a) Velocity

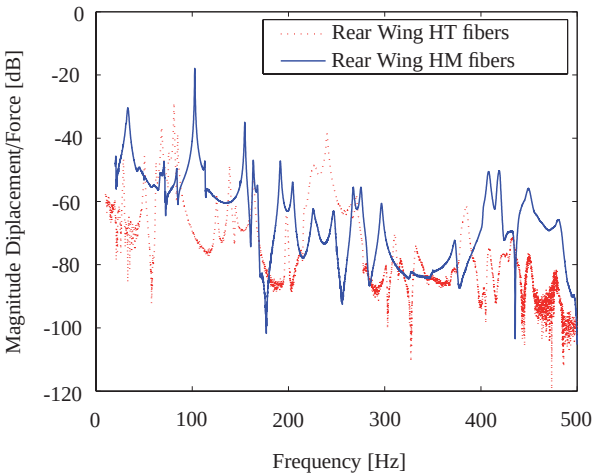

(b) Displacement

Figure 10.3: (a) Velocity amplitude response of the rear wing mounting original (HT fibers) and modified (HM fibers) endplates, respectively. (b) Displacement amplitude response of the rear wing mounting original (HM fibers) and modified (HM fibers) endplates, respectively (Input: CoM, left endplate; Output: rear upper corner right endplate).

10.2 Sensors and Actuators

10.2.1 Selection

Based on the findings in Chapter 8, conventional monolithic actuators working on the indirect 3-1 piezoelectric effect were preferred for their larger capacitance and ease of manufacturing. In order to guarantee activation of the switching shunt's MOSFETs, Active Fiber Composites were selected as sensors. Indeed, the interdigitated electrode configuration will deliver higher voltage per strain unit compared to the conventional actuators.

Among the large number of piezoelectric ceramic wafer available on the market, VIBRIT 1334 from Argillon GmbH[1] was selected for its relatively high dielectric constant, the excellent coupling coefficient, the reasonably high Curie temperature and the rather low risk of mechanical depolarization (see [206] for a detailed description of the ceramic selection process). Piezoelectric ceramic fibers for AFC manufacturing were supplied by Smart Material, Corp. They performed best according to the investigations described in Chapter 3.

10.2.2 Optimum Dimensions and Placement

In Chapter 9 a procedure based on evolutionary algorithms was developed for optimum placement of piezoelectric ceramic modules on real-world, highly constrained lightweight structures. Position, dimensions, orientation and embedding depth of customized piezoelectric ceramic modules were determined for optimum vibration suppression performance considering a number of operational and manufacturing constraints. The best configuration found by the optimization engine is presented in Figure 9.6 with two actuators galvanically coupled on each endplate. The added mass is approximately 1% of the original rear wing mass.

Applying the same optimization loop, position and orientation of an AFC sensor were optimized for co-local conditions, i.e. the sensor voltage signal and the actuator voltage signal are in phase in the vicinity of the eigenfrequency addressed. Figure 10.4 (a) shows the actuators and sensor

[1] Argillon GmbH Piezoproducts, Bahnhofstr. 43, 96257 Redwitz, Germany

placement on the endplate, including the wiring for external control and the single piezoelectric ceramic wafers.

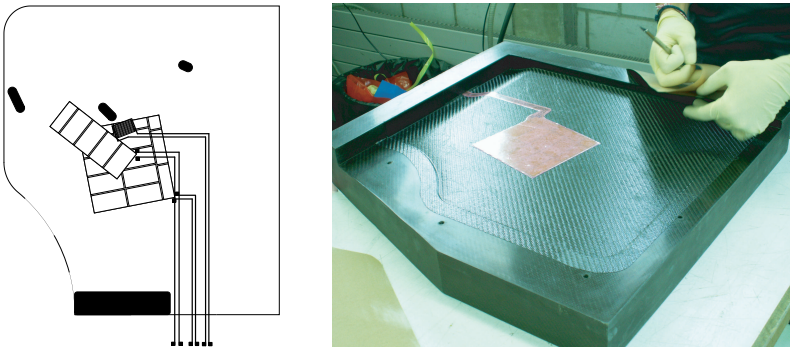

(a) (b)

Figure 10.4: (a) Optimum placement of two actuators and one sensor on the endplate. (b) The piezoelectric ceramic elements were embedded at optimum locations in the original laminate using the simple insertion technology. Single ceramic wafers were galvanically coupled and encapsulated in polyimide films for electrical insulation, ease of handling and damage protection.

10.2.3 Manufacturing

An encapsulation technology [207] developed at DLR Braunschweig was selected that protects the brittle ceramic modules against harmful tension and electrically insulates them from the surrounding, conducting graphite fibers. The metal sputtered electrodes are covered by a thin copper mesh that ensures contact even in case of local mechanical failure of the ceramic wafer. Both the ceramic wafer and the copper mesh are surrounded by epoxy matrix and polyimide foils.

Due to the higher thermal coefficient of the embedding compound, the

ceramic modules are pre-loaded during cooling after curing of the matrix system. This ensures an elongation at break of about 0.4%. The maximum recommended working strain is 0.2%.

AFC are composed of piezoelectric ceramic fibers surrounded by epoxy matrix. The electric charge generated by the direct piezoelectric effect is collected by interdigitated electrodes printed on polyimide films. Varying the electrode spacing as described in Chapter 5, one can tune the sensor's sensitivity.

10.2.4 Embedding

The influence of embedded active elements on the mechanical behavior of the hosting laminate structure was investigated in Chapter 7, both numerically and experimentally for a cross-ply graphite/epoxy laminate. All embedding configurations were found to decrease the laminate's ultimate strength. The interlaced configuration distributes the disturbance over the whole laminate thickness, thus showing the smallest influence (see Table 10.3). The inserted configuration showed a slightly larger decrease in laminate ultimate strength and causes the smallest manufacturing effort. Despite showing largest influence on the laminate properties, the cut-out configuration potentially allows the integration of multiple active elements in the same section. The endplate being composed almost exclusively of layers oriented in vertical direction, the piezoelectric ceramic modules were successfully embedded in the endplate's skins by simple insertion (Figure 10.4 (b)).

10.2.5 Wiring

The wiring of the piezoelectric ceramic modules is a critical issue for their efficient embedding in the laminate host structure. A novel method for conductor printing using a commercial ink-jet printer was developed as presented in Chapter 6. This simple, reproducible, inexpensive technology allows for moderate resolution (approx. 200μm) copper patterning on the high performance substrate polyimide. Thus, the polyimide films provide for both the ceramic encapsulation and its wiring.

Table 10.3: Influence of different embedding strategies on the laminate's ultimate strength.

Configuration	Ultimate Strength Reduction	Advantages	Disadvantages
Cut Out	(-25%)	Constant thickness, ease of placement	Layer cuts, costly, time consuming
Simple Insertion	-10%	No layer cuts, inexpensive, time-efficient	Difficult placement, resin-rich regions
Interlaced	-6%	Optimum disturbance distribution, constant thickness	Costly, time-consuming

10.3 Shunt Circuits

Three different shunt circuits were built for suppressing the structural vibration of the rear wing. Table 10.4 gives an overview of the main advantages and drawbacks specific to each different control strategy. The interested reader finds detailed information on shunt control in Niederberger [20] and Fleming [21].

10.3.1 *R-L* Shunt Circuit

Passive coils were winded for external control of the embedded piezoelectric ceramic actuators. Being relatively bulky, they make fine tuning of the *R–L* shunt difficult. Virtual inductors based on a single OpAmp [206] were implemented as shown in Figure 10.5 for flexible shunt circuit prototyping.

10.3.2 Switching Shunt Circuit

A switching shunt [204, 152] was considered for a completely autonomous control approach. In order to integrate the control circuit in the structural part, the circuit components' sizes were reduced [206] as to fit in the endplate's honeycomb core. SMD components were soldered on the printed circuit shown true to scale in Figure 10.6 (a). Smallest ferromagnetic cores were selected, whereas the coils themselves were winded using a copper wire 50μm in diameter (see Figure 10.6 (b)).

10.3.3 Positive Position Feedback Control Circuit

An active Positive Position Feedback (PPF) control circuit [205] was implemented for performance comparison with the passive shunts described in the previous sections.

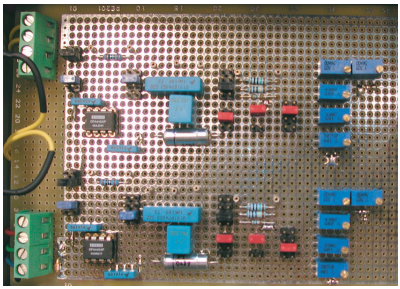

(a)

Figure 10.5: View of the virtual inductor circuits.

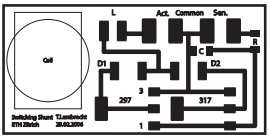

(a)

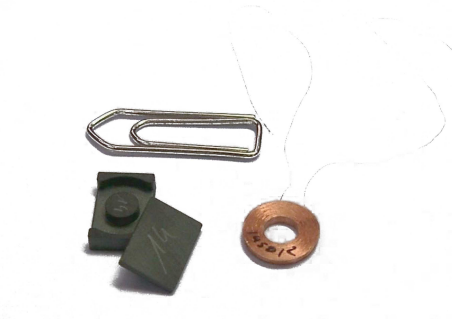

(b)

Figure 10.6: Switching shunt circuit (true to scale): (a) Printed circuit for SMD components, left is a slot for the coil (b) Coil windings and core.

Table 10.4: Comparison of different control strategies.

Control strategy	Type	Strengths	Drawbacks
$R-L$ shunt	Passive	Good performance Stability guaranteed	Gets *easily* detuned
Switching $R-L$ shunt	Passive	Robust Stability guaranteed	Moderate performance Sensor required
PPF controller	Active	High performance	Sensor, bulky amplifier required Risks of spillover and instability

10.4 Vibration Suppression

10.4.1 Cantilever CFRP plate

As a preparatory step, a first comparison between the three control strategies (1) *R–L* shunt, (2) switching *R–L* shunt and (3) PPF control was carried out on a cantilever CFRP plate with embedded co-located monolithic actuator and AFC sensor. This preliminary investigation also tested the embedding strategy and showed the piezoelectric ceramic modules to survive the laminate curing cycle without any evident damage. The first eigenmode at 48.5Hz was addressed. The resonant *R–L* shunt achieved a vibration suppression of 11 dB or 72% (Figure 10.7 (a)). The large inductance had to be synthesized using the virtual inductor described in Section 10.3. As depicted in Figure 10.7 (b), the autonomous but less efficient switching *R–L* shunt showed a vibration suppression of 5.3 dB or 45%. The miniaturized coil depicted in Figure 10.6 was successfully employed. Not surprisingly, the active PPF controller achieved the best vibration suppression performance of 30.4 dB or 97%. The experimental results are summarized in Table 10.5.

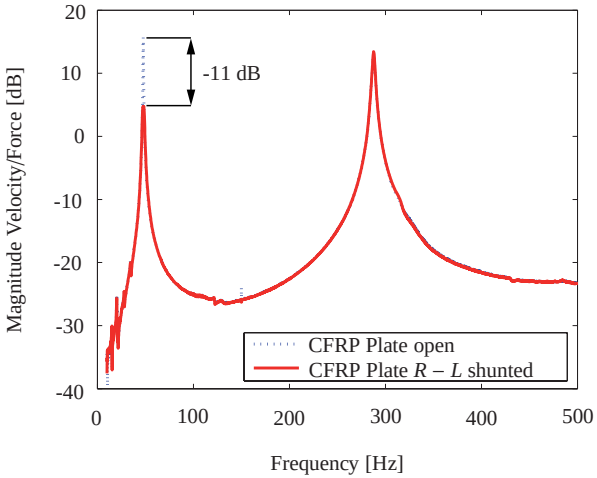

(a) $R - L$ Shunt

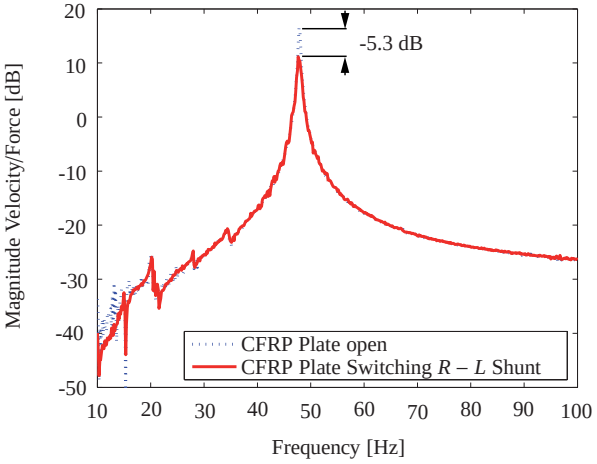

(b) Switching $R - L$ Shunt

Figure 10.7: Velocity amplitude response of the cantilevered CFRP plate with embedded piezoelectric ceramic modules. (a) Open system (···) and $R - L$ shunted system (—), respectively. Vibration suppression for the 1^{st} mode (at 48.5Hz): 11 dB (72%). (b) Open system (···) and switched $R - L$ shunted system (—), respectively. Vibration suppression 5.3 dB (45%).

Table 10.5: Vibration suppression performance of the passive $R-L$ shunt, of the passive switching $R-L$ shunt and of the active PPF controller, respectively. Natural mode of the cantilevered CFRP plate at 48.5Hz. Inherent piezoelectric capacitance $0.28\mu F$.

Control strategy	Type	Inductance [H]	Resistance [Ω]	Vibration suppression [dB]
$R-L$ shunt, R_{opt}	Passive	37.69	332.89	-11.0 (72%)
Switching $R-L$ shunt	Passive	4.12	81.47	-5.3 (45%)
PPF controller	Active			-30.4 (97%)

10.4.2 Rear Wing

The optimization algorithm placed the piezoelectric ceramic modules for optimum vibration suppression of the 1^{st} mode. Tuning the large actuator to the natural mode at 35.5 Hz required an inductance value of 7.83H for the *R–L* shunt. Despite the large voltage increase, indicating optimal tuning, no vibration suppression could be achieved due to the insufficient electromechanical coupling. The discrepancy between numerical and experimental results can most probably be explained with the insufficient accuracy of the numerical model. At the interface region, upper mainplane and endplates were assumed to be coupled along the contour of the mainplane profile. The corresponding strain distribution ϵ_z is depicted in Figure 10.8 (a). The simplification was justified by the pre-stress of the assembly and delivered very accurate eigenvalues for the low frequency range. In reality, we have to deal with a contact problem that strongly influences the eigenmodes and thus the strain distribution. As opposite configuration, the strain distribution ϵ_z for a free contour is visualized in Figure 10.8 (b). Mainplane and endplates can separate and penetrate each other.

On the other hand, the trailing edge's flutter mode on the endplates (at 103.5 Hz, Figure 10.9 (a)) could be successfully damped. Even with suboptimal placement of the piezoelectric ceramic modules, the resonant *R–L* shunt achieved a vibration suppression of 12.5 dB or 76%. Figure 10.9 (b) shows the antiresonance induced by an optimally tuned *R–L* shunt network and the characteristic plateau of an optimally damped system. The active PPF controller recorded a vibration suppression of 17.0 dB or 86% (Figure 10.10 (b)). This falling short of expectations is due to the not perfectly co-local placement of sensor and actuator. For this same reason, and due to the limited performance reported in Section 10.4.1, the switching *R–L* shunt was not implemented.

The reported vibration suppression performances were achieved with the large piezoelectric ceramic module embedded in the right endplate alone connected to the *R–L* shunt and to the PPF controller, respectively. The experimental results for the trailing edge's flutter mode on the endplate are summarized in Table 10.6.

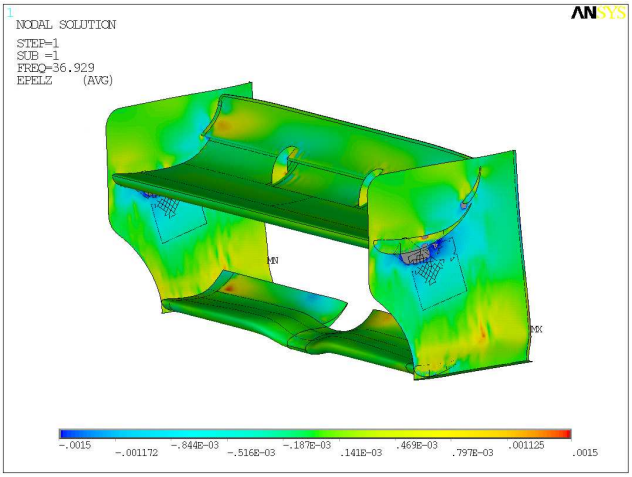

(a) Contour constrained

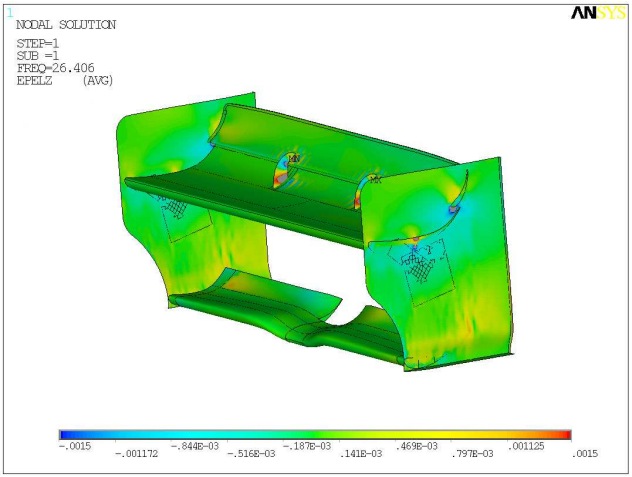

(b) Contour not constrained

Figure 10.8: Rear wing mounting modified endplates (HM fibers), strain distribution ϵ_z. (a) Interface between upper mainplane and endplates constrained along the contour of the mainplane profile. (b) Interface between upper mainplane and endplates *not* constrained along the contour of the mainplane profile.

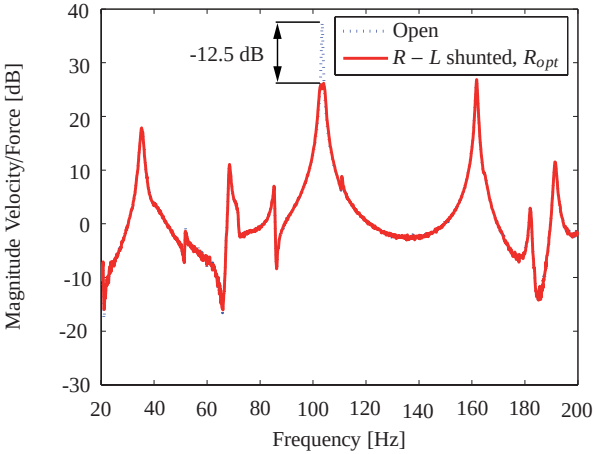

(a) $R - L$ shunt

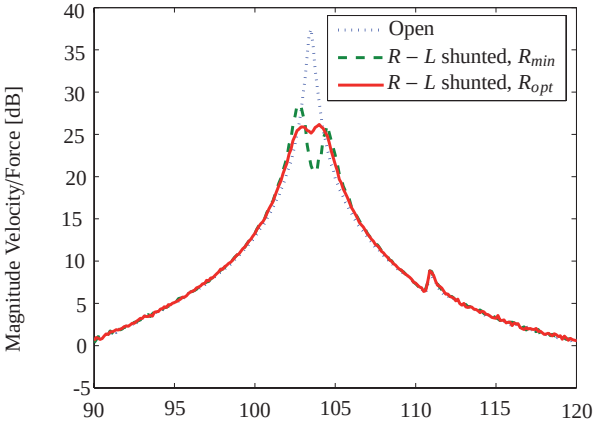

(b) $R - L$ shunt, R_{min} and R_{opt}

Figure 10.9: Rear wing mounting modified endplates (HM fibers). (a) Velocity amplitude response of the open system (···) and $R - L$ shunted system (—), respectively. Vibration suppression for the endplate trailing edge's flutter mode: 12.5 dB (76%). (b) Velocity amplitude response around the eigenfrequency at 103.5 Hz. Notice the optimally tuned $R - L$ shunted system (- - -, vibration suppression: 16.4 dB, 85%) and the optimally damped $R - L$ shunted system (—, vibration suppression: 12.5 dB, 76%). (Input: CoM, left endplate; Output: rear upper corner right endplate).

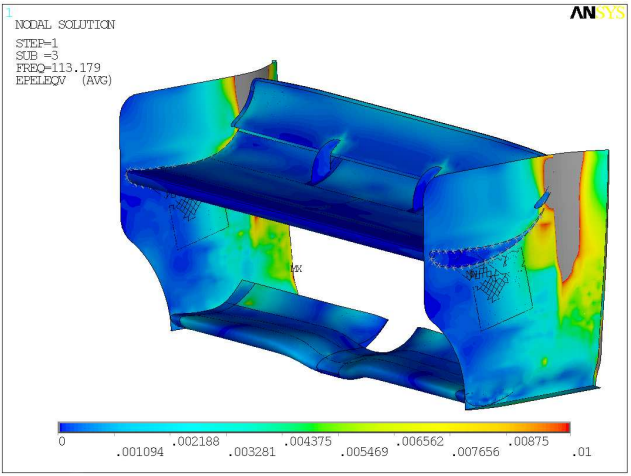

(a) Strain distribution

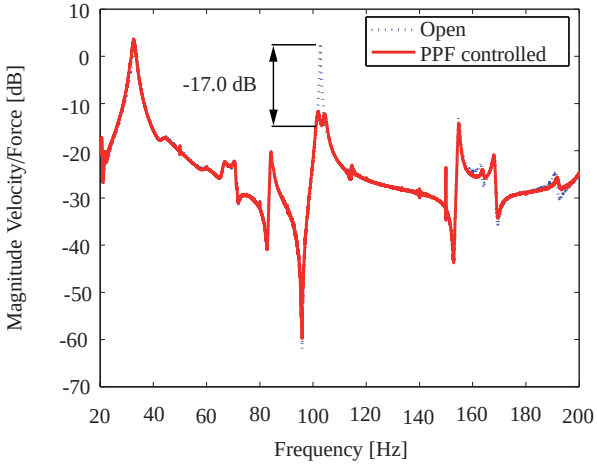

(b) PPF control

Figure 10.10: (a) Von Mises strain distribution for the endplate trailing edge's flutter mode at 103.5 Hz. (b) Velocity amplitude response of the modified rear wing for the open system (···) and PPF-controlled system (—, vibration suppression: 17 dB, 86%), respectively. Only the large piezoelectric ceramic module embedded in the right endplate was connected to the electrical network (Input: CoM, left endplate; Output: middle point upper edge right endplate).

Table 10.6: Vibration suppression performance of the passive $R-L$ shunt and active PPF controller, respectively. Trailing edge's flutter mode of the endplates at 103.5Hz. Inherent piezoelectric capacitance $3.14\mu F$.

Control strategy	Type	Inductance [mH]	Resistance [Ω]	Vibration suppression [dB]
$R-L$ shunt, R_{min}	Passive	730.24	1.48	-16.4 (85%)
$R-L$ shunt, R_{opt}	Passive	745.72	7.52	-12.5 (76%)
PPF control	Active			-17.0 (86%)

10.5 Conclusions

The methods and technologies developed as reported in the previous Chapters were successfully verified on a test object.

After selection of the rear wing of a racing car, its dynamic response was simulated numerically and identified experimentally; the natural frequency of the test object was increased by use of HM graphite fibers in order to mitigate the requirements on the inductance of the *R–L* shunt.

Dimensions, locations and orientations of piezoelectric ceramic elements were determined for optimum vibration suppression performance under consideration of a number of operational and manufacturing constraints. Appropriate piezoelectric ceramic wafers and fibers were encapsulated in electroded polyimide films for mechanical protection and electrical insulation from the carbon fiber laminate in which they were embedded.

Three different shunt circuits were built for suppressing the structural vibration of the rear wing, namely a passive resonant *R–L* shunt, an autonomous switching *R–L* shunt, and an active PPF control circuit.

Contrary to expectations, the vibration of the first mode - likely to be excited by roughness and curbs of the race track - could not be successfully suppressed due to the insufficient accuracy of the numerical model in predicting the strain distribution and subsequent misplacement of the piezoelectric ceramic modules for maximum electromechanical coupling. On the other hand, a flutter mode at the endplate's trailing edge was effectively damped that could be aerodynamically relevant. The passive *R–L* shunt reduces the vibration by 12.5 dB or 76% and the active PPF controller achieves a vibration suppression of 17 dB or 86%. In this context, a significant performance enhancement of the *R–L* shunt can be expected for optimally placed piezoelectric ceramic elements. The performance of the active PPF controller, in addition, can be significantly enhanced by having a properly co-located sensor. For the implementation of switching *R–L* shunt and PPF control strategies, it is therefore recommended to use

a single rectangular actuator. This simplifies the task of ensuring co-local conditions between actuator and sensor. The reported performance was achieved with an additional mass of less than 1%.

It is advised to investigate the drag reduction potential of such a vibration suppression.

Chapter 11

Conclusions and Prospects

The main achievements of this thesis are enabling methods and techniques for the implementation of structural vibration suppression of real-world composite systems via shunted piezoelectric systems.

11.1 Summary

A long way took us from the material characterization of single active components up to the assembly and operation of a complex smart system.

A novel characterization procedure for the ferroelectric characterization of single piezoelectric fibers gave insight into their material properties. Butterfly and hysteresis loops and force-displacement curves were measured for three different commercially available fibers and fibers under development at Empa Duebendorf. The observed response was correlated to the respective microstructural properties and fibers were identified for manufacturing AFC then embedded into the test object.

The response of Active Fiber Composites was investigated both numerically and experimentally. An optimization routine based on evolution-

ary algorithms assessed the potential for performance enhancement. Only marginal improvements could be achieved with respect to the requirements imposed to active components for use in structural vibration control.

Another step towards proper integration of sensors and actuators into load-carrying composite structures was taken by developing a laboratory method for prototyping large area circuitry with moderate resolution on electrically and thermally stable polyimide. The technique was used for manufacturing all electrode films then laminated to monolithic and AFC active modules, components of the test object. Numerical and extensive experimental investigations quantified the impact of their inclusion onto GFRP and CFRP laminate strength. The best trade-off between mechanical reliability and smart functionality can be realized using active modules symmetrically embedded into CFRP cross-ply laminates using the interlaced integration technique. The encapsulation of piezoelectric ceramic wafers allowed for larger modules, perfect insulation and ease of handling.

The vibration suppression performance of both monolithic actuators and AFC was predicted by analyzing the passive structure, the bonded active patch, and the shunted circuit within an integrated multi-field FE model. Numerical simulations showed excellent agreement with experimental results, accurately predicting eigenfrequencies, eigenmodes and suppression levels. AFC patches achieved equivalent vibration suppression performance per active unit volume as the monolithic actuators. A weighty drawback is, however, their low inherent piezoelectric device capacitance. Monolithic actuators operating on the 3-1 piezoelectric effect were therefore found to be the best for use in *R-L* shunting. AFC, however, could be used as sensors with orthotropic properties or to control switching shunts.

Monolithic actuators and AFC sensors were successfully placed for optimum vibration suppression using *R-L* and switching *R-L* shunts. The optimization approach includes a CAD-model, an FE-model and evolutionary algorithms and proved a valuable tool in finding optimum solutions for real-world, highly constrained structures.

A test object verified all methods and techniques summarized above. Vibrations on a rear wing structure could be successfully suppressed by shunting actuators and sensors embedded into the wing's laminate to *R-L* circuits, respectively to a PPF controller.

When methods of analysis and design presented in the present thesis will hopefully help allowing rapid development of smart structures and systems, a number of issues remain open and were emphasized by the challenges encountered during the project. These are briefly presented in the next Section.

11.2 Prospects

In general, future research needs are identified in the severe limitations imposed to smart systems development by the functional and structural properties of current piezoelectric materials, as well as in aspects such as reliability, robustness, and costs of the smart system.

Material scientists will have a leading part in shaping the future of smart composite systems. Both functional and mechanical properties of currently available piezoelectric ceramic materials represent a bottleneck for their successful development. For vibration suppression, high coupling factors and inherent piezoelectric capacitance are desired. A far larger problem is the brittleness of current piezoelectric ceramic materials, which make their handling and integration into a real smart system a challenging task.

Awaiting for materials with enhanced properties, mechanical engineers can obviate such limitations by integrating the piezoelectric ceramic modules into composite sensor and actuator systems, which can show very different mechanical properties compared to their components. Examples thereof are the research on Active Fiber Composites or the work on

piezoelectric ceramic modules at DLR. A promising approach for sensors and actuators with enhanced mechanical properties is the manufacturing of monolithic ceramic modules, which were thermally, electrically or mechanically prestressed. Preliminary results show an increase in maximum tensile strain up to 0.5%, raising hope that active components will soon reach maximum strains comparable with those of the hosting composite structures.

Reliability of smart systems is, of course, of concern for any real application. Additional functionality will inevitably increase the complexity of the system and the probability of a disturbance. In general, smart systems will have to be fail-safe and designed in a way that failure can be immediately detected. Redundancy of given components might also be a way for increasing the availability of the system. Extensive investigations within this thesis showed inclusion of sensors and actuators into composite structures to be detrimental to their mechanical properties. Thinner sensors and actuators are expected to alleviate the problem. It is therefore advised to invest into manufacturing routes for thinner piezoelectric ceramic modules and processing of thinner insulating material including wiring and contacting.

Another issue awaiting to be investigated is the impact of such inclusions on the fatigue behavior of the hosting composite structure. A proper adhesion between the encapsulation material of the active modules and the composite laminae minimizes their delamination risk. Plasma, corona discharge or wet-chemical treatments are available techniques for the surface treatment of polyimide films to be laminated with graphite prepreg sheets. Preliminary peel test investigations have shown the adhesion enhancement through the techniques mentioned above to differ significantly if applied to virgin polyimide films or to polyimide films that previously underwent wet-chemical treatment for printing copper circuitry as described in Chapter 6. It is advised to investigate the chemical interactions between (modified) polyimide and epoxy resins and carry out extensive experimental peel testing in order to identify the best treatment combination for optimum adhesion.

Modeling of the dynamic response of the structure at hand once again emerged as a key feature within the development of complex smart systems. The discrepancy in strain distribution between numerical model and reality described in Chapters 9 and 10 is just another example that no optimization procedure can deliver more realistic results as the model it is running. The level of detail of the model, on the other hand, directly impacts the computational time required for evaluation. An appropriate level of detail and, whenever possible, an experimental validation of the numerical results are preconditions for increasing the success rate in smart systems development. Future work in this field should include a validated virtual simulation environment for the development and optimization of damping solutions.

A smart system with highest performance under laboratory conditions will be of little use in real applications, unless showing a given robustness to changing external conditions, discrepancies between simulation model and reality, and alterations of the system itself. In the case of vibration suppression, these might be changes in boundary or environmental conditions (such as temperature or humidity), material aging or added mass (e.g. due to dirt accumulating on the surface), all affecting the system frequency and vibration modes. The adaption laws for the control algorithm developed and used within the project PiezoDamp provide valuable means for coping with changing system frequency; for future real applications, the number, the dimensions and the placement of sensors and actuators should also be determined considering the robustness requirement of the system. Repeatability of the system performance will also be an issue to address when planning manufacturing and serial production of smart systems.

Referring to the test object, finally, the suppression of structural vibrations itself is not the ultimate goal. Much more interesting is the potential reduction in aerodynamically induced drag related to the same vibration suppression. Preliminary results in the wind tunnel showed the ability of the proposed technology to significantly damp structural vibrations excited by the aerodynamic flow. There was no evidence of a direct effect on the

induced drag, because the drag contribution of the endplates is negligible compared to the overall rear wing drag. As per expert opinions, however, a reduction in structural vibration is generally expected to have positive impact on the aerodynamically induced drag. Thus, prior to developing such systems, a proper understanding of the fluid-structure interaction is needed.

We believe that the time is ripe for innovation by means of which smartness in structures can come about through development of new materials with required properties and new designs that allow integration of multiple functions of sensing, diagnosing, and actuating structures, leading to vastly enhanced structural integrity. In the scope of the present thesis, enabling methods and techniques were developed and verified within a laboratory environment. Our findings will provide scientific fundament for a number of applications.

For a smart system to achieve advantages over conventional ones in real applications, however, the system has to prove to be superior under consideration of all boundary conditions defined for the intended field of application. Focusing on vibration suppression, the use of smart systems might generally target three different goals: to extend the operation range of the system; to extend service life compared to the conventional system, assuming the same load-carrying structure; to design and operate a lighter structure that fulfills the same operational and service life requirements as the conventional system. In all cases the advantages have to justify the larger investment costs. In other words, before getting to a true innovation, a good idea has to be accepted by the market. Future work in this field thus cannot afford to neglect aspects such as overall system reliability, manufacturability, required control energy and life cycle costs.

List of Figures

List of Tables

Bibliography

[1] B. Jaffe, W. R. Cook, and H. Jaffe. *Piezoelectric Ceramics*, volume 3 of *Non-Metallic Solids*. Academic Press, London, 1971.

[2] R. E. Hummel. *Electronic Properties of Materials*. Springer, New York, 3rd edition, 2001.

[3] G. Engdahl. *Handbook of Giant Magnetostrictive Materials*. Academic Press, London, 1st edition, 2000.

[4] V. Brailovski, S. Prokoshkin, P. Terriault, and F. Trochu. *Shape Memory Alloys: Fundamentals, Modeling and Applications*. Université du Québec, Ecole de Technologie Supérieure, 2003.

[5] C. Youyi and K. Otsuka. *Shape Memory Alloys*. International Academic Publishers, August 2002.

[6] T. Hao. *Electrorheological Fluids*. Elsevier, November 2005.

[7] R. Tao, editor. *Electro-Rheological Fluids and Magneto-Rheological Suspensions - Proceedings of the 7th International Conference*, Honolulu, Hawaii, July 1999.

[8] Y. Bar-Cohen. *Electroactive Polymer (EAP) Actuators as Artificial Muscles - Reality, Potential and Challenges*, volume PM98. SPIE Press, 1st edition, March 2001.

[9] Y. Saito, H. Takao, T. Tani, T. Nonoyama, K. Takatori, T. Homma, T. Nagaya, and M. Nakamura. Lead-free piezoceramics. *Nature*, 432:84–87, November 2004.

[10] D. D. Shin, D. Lee, K. P. Mohanchandra, and G. P. Carman. Thin film shape memory alloy motor for a compact kinetic energy missile. In 13^{th} *International Conference on Adaptive Structures and Technologies*, Potsdam, October 2002.

[11] G. Kovacs, S. M. Ha, S. Michel, R. Pelrine, and Q. Pei. Study on core free rolled actuator based on soft dielectric EAP. In *SPIE - Electroactive Polymer Actuators and Devices (EAPAD) 2008*, volume 6927, San Diego (CA), March 2008.

[12] A. A. Bent, N. W. Hagood, and J. P. Rodgers. Anisotropic actuation with piezoelectric fiber composites. *Journal of Intelligent Material Systems and Structures*, 6(3):338–349, May 1995.

[13] P. Wierach. Low profile piezo actuators based on multilayer technology. In 17^{th} *International Conference on Adaptive Structures and Technologies*, Taipei, Taiwan, October 2006.

[14] P. Lochmatter, G. Kovacs, and P. Ermanni. Design and characterization of shell-like actuators based on soft dielectric electroactive polymers. *Smart Materials and Structures*, 16(4):1415–1422, August 2007.

[15] W. I. Kordonski, A. D. Matsepuro, V. N. Makatun, Z. A. Novicova, and S. A. Demchuk. Electrorheological fluid composite structures. European Patent 1993924457, April 1996, withdrawn 1998.

[16] F. Weber, G. Feltrin, and M. Motavalli. Passive damping of cables with MR dampers. *Material and Structures*, 38(279):568–577, July 2005.

[17] F. Weber, H. Distl, P. Huber, O. Nuetzel, and M. Motavalli. Design implementation and field test of the adaptive damping system of the Franjo Tudjman bridge nearby Dubrovnik, Croatia. In

IABSE Symposium, Improving Infrastructure Worldwide, Weimar, Germany, September 19-21 2007.

[18] K. Halter, A. Sickinger, L. Zysset, and S. Siegmann. Low pressure wire arc and vacuum plasma spraying of NiTi shape memory alloys. In *ITSC International Thermal Spray Conference - Advancing the Science and Applying the Technology*, pages 589–595, Orlando (FL), 2003.

[19] S. Siegmann, K. Halter, and B. Wielage. Vacuum plasma sprayed coatings and freestanding parts of Ni-Ti shape memory alloy. In *ITSC International Thermal Spray Conference*, pages 357–361, Essen, Germany, 2002.

[20] D. Niederberger. *Smart Damping Materials using Shunt Control*. PhD thesis, ETH Zurich. Diss. ETH No. 16043, 2005.

[21] A. J. Fleming. *Synthesis and Implementation of Sensor-less Shunt Controllers for Piezoelectric and Electromagnetic Vibration Control*. PhD thesis, School of Electrical Engineering and Computer Science, University of Newcastle, Callaghan, N. S. W. 2308, Australia, February 2004.

[22] D. Niederberger, A. J. Fleming, S. O. R. Moheimani, and M. Morari. Adaptive multi-mode resonant piezoelectric shunt damping. *Smart Materials and Structures*, 13(5):1025–1035, October 2004.

[23] L. F. Campanile and O. Mierheim. Three-dimensional structural and aeroelastic analysis of morphing airfoils. In 16^{th} *International Conference on Adaptive Structures and Technologies*, pages 61–68, Paris, October 2005.

[24] D. Ramrakhyani, G. A. Lesieutre, M. Frecker, and S. Bharti. Aircraft structural morphing using tendon-actuated compliant cellular trusses. *Journal of Aircraft*, 42(6):1615–1621, November-December 2005.

[25] K.-J. Lu and S. Kota. Design of compliant mechanisms for morphing structural shapes. *Journal of Intelligent Material Systems and Structures*, 14(6):379–391, June 2003.

[26] A. Daniele, S. Salapaka, M. V. Salapaka, and M. Dahleh. Piezoelectric scanners for atomic force microscopes: Design of lateral sensors, identification and control. In *Proceedings of the American Control Conference*, pages 253–257, San Diego (CA), June 1999.

[27] M. Birchmeier, A. J. Brunner, R. Paradies, and J. Dual. Experimental characterization of active fiber composites used as piezoelectric transducers for emitting and receiving lamb waves in plate-like structures. In *ATEM07: International Conference on Advanced Technology in Experimental Mechanics*, Fukuoka, Japan, September 2007.

[28] R. Steinhausen, T. Hauke, W. Seifert, H. Beige, W. Watzka, S. Seifert, D. Sporn, S. Starke, and A. Schönecker. Finescaled piezoelectric 1-3 composites: Properties and modeling. *Journal of the European Ceramic Society*, 19(6-7):1289–1293, June 1999.

[29] R. J. Meyer, S. Yoshikawa, and T. R. Shrout. Processing and properties of 15-70 MHz 1-3 PZT fiber/polymer composites. *Materials Research Innovations*, 3(6):324–331, October 2000.

[30] A. M. Sadri, J. R. Wright, and R. J. Wynne. LQG control design for panel flutter suppression using piezoelectric actuators. *Smart Materials and Structures*, 11(6):834–839, December 2002.

[31] N. A. J. Lieven. Piezo-electric actuation of helicopter rotor blades. In D. J. Inman, editor, *SPIE Smart Structures and Materials - Damping and Isolation*, volume 4331, pages 432–442, Newport Beach, CA, March 2001.

[32] Y. K. Yong, S. S. Aphale, and Moheimani S. O. R. Design, identification, and control of a flexure-based XY stage for fast nanoscale positioning. *IEEE Transactions on Nanotechnology*, 8(1):46–54, January 2009.

[33] D. Gorinevsky, G. A. Gordon, S. Beard, A. Kumar, and F.-K. Chang. Design of integrated SHM system for commercial aircraft applications. In 5th *International Workshop on Structural Health Monitoring*, Stanford (CA), September 2005.

[34] H.-S. Lee and S.-B. Choi. Control and response characteristics of a magneto-rheological fluid damper for passenger vehicles. *Journal of Intelligent Material Systems and Structures*, 11(1):80–87, January 2000.

[35] M. J. Chrzan and J. D. Carlson. MR fluid sponge devices and their use in vibration control of washing machines. In D. J. Inman, editor, *SPIE Smart Structures and Materials - Damping and Isolation*, volume 4331, pages 370–378, Newport Beach (CA), March 2001.

[36] A. Pohl, H. Rosenfeldt, E. Wendt, and K. Buesing. Hydraulic displacement machine. United States Patent 6149391, November 2000.

[37] S. Dong. *Development and control of variable resistance exercise device with magnetorheological fluids*. PhD thesis, University of Delaware, 2005.

[38] W. I. Kordonski, D. Golini, S. Hogan, and A. Sekeres. System for abrasive jet shaping and polishing of a surface using magnetorheological fluid. United States Patent 5971835, October 1999.

[39] D. J. Ellam, W. A. Bullough, and S. M. Chen. Comparison of ERF clutch designs. In *Electrorheological Fluids and Magnetorheological Suspensions - Proceedings of the* 10th *International Conference on ERMR 2006*, pages 396–402, Lake Tahoe, June 2006.

[40] H. J. Song, S. B. Choi, Y. S. Jeon, and N. M. Wereley. Vibration control of engine mount using ER fluid and piezoelectric actuator. In *Electrorheological Fluids and Magnetorheological Suspensions - Proceedings of the* 10th *International Conference on ERMR 2006*, pages 733–740, Lake Tahoe, June 2006.

[41] Y. Bar-Cohen. EAP as artificial muscles - capabilities, potentials and challenges. In *Robotics 2000 and Space 2000*, Albuquerque (NM), February - March 2000.

[42] D. P. Garg, M. A. Zikry, and G. L. Anderson. Current and potential future research activities in adaptive structures: an ARO perspective. *Smart Materials and Structures*, 10(4):610–623, August 2001.

[43] R. B. Cass. Fabrication of continuous ceramic fiber by the viscous suspension spinning process. *American Ceramic Society Bulletin*, 70(3):424–429, 1991.

[44] F. Meister, D. Vorbach, F. Niemz, and T. Schulze. Functional high-tech-cellulose materials by the ALCERU® process. *Materialwissenschaft und Werkstofftechnik*, 34(3):262–266, March 2003.

[45] H. B. Strock, M. R. Pascucci, M. V. Parish, A. A. Bent, and T. R. Shrout. Active PZT fibers, a commercial production process. In M. R. Wuttig, editor, *SPIE Smart Structures and Materials - Smart Materials Technologies*, volume 3675, pages 22–31, Newport Beach, CA, March 1999.

[46] W. A. Smith. Modeling 1-3 composite piezoelectrics: Hydrostatic response. *IEEE Transactions on Ultrasonic, Ferroelectrics, and Frequency Control*, 40(1):41–49, January 1993.

[47] A. A. Bent and A. E. Pizzochero. Recent advances in active fiber composites for structural control. In J. Jacobs and J. Jacobs, editors, *SPIE Smart Structures and Materials - Industrial and Commercial Applications of Smart Structures Technologies*, volume 3991, pages 244–254, Newport Beach, CA, March 2000.

[48] G. Goddu, D. McDowell, and B. S. Bingham. Adaptive control of radiated noise from a cylindrical shell using active fiber composite actuators. In J. H. Jacobs, editor, *SPIE Smart Structures and Materials - Industrial and Commercial Applications of Smart Structures Technologies*, volume 3991, pages 95–102, Newport Beach, CA, March 2000.

[49] K. Adachi, G. Park, and D. J. Inman. Passive damping augmentation using macro-fiber composite actuators. In J. Shaw and M. Frecker, editors, *ASME International Mechanical Engineering Congress & Exposition (IMECE)*, volume 67, pages 71–78, New Orleans, LA, November 2002.

[50] A. Belloli, D. Niederberger, S. Pietrzko, M. Morari, and P. Ermanni. Structural vibration control via *R-L* shunted active fiber composites. *Journal of Intelligent Material Systems and Structures*, 18(3):275–287, March 2007.

[51] C. B. Sawyer and C. H. Tower. Rochelle salt as a dielectric. *Physical Review*, 35(3):269–273, February 1930.

[52] L. J. Nelson, C. R. Bowen, R. Stevens, M. Cain, and M. Stewart. High field behaviour of piezoelectric fibre composites. In D. C. Lagoudas, editor, *SPIE Smart Structures and Materials - Active Materials: Behavior and Mechanics*, volume 5053, pages 544–555, San Diego, CA, March 2003.

[53] L. J. Nelson, C. R. Bowen, R. Stevens, M. Cain, and M. Stewart. Evaluation of high field responses of fine scale piezoelectric fibers. *Integrated Ferroelectrics*, 63(1):41–47, 2004.

[54] M. Stewart, M. G. Cain, and D. A. Hall. Ferroelectric hysteresis measurement and analysis. Technical Report CMMT (A) 152, National Physical Laboratory, Teddington UK, 1999.

[55] B. Dickens, E. Balizer, A. S. DeReggi, and S. C. Roth. Hysteresis measurements of remanent polarization and coercive field in polymers. *Journal of Applied Physics*, 72(9):4258–4264, November 1992.

[56] C. J. Dias and D. K. Das-Gupta. Hysteresis measurements on ferroelectric composites. *Journal of Applied Physics*, 71(10):6317–6321, November 1993.

[57] S. Yoshikawa, U. Selvaraj, P. Moses, J. Witham, R. Meyer, and T. Shrout. $Pb(Zr, Ti)O_3$ [PZT] fibers - fabrication and measurement methods. *Journal of Intelligent Material Systems and Structures*, 6(2):152–158, March 1995.

[58] P. Bystricky. Ceramic piezoelectric fibers: Correlating single fiber properties with active fiber composite performance. In N. M. Wereley, editor, *SPIE Smart Structures and Materials - Smart Structures and Integrated Systems*, volume 3985, pages 552–559, Newport Beach, CA, March 2000.

[59] G. Sorge, T. Hauke, and M. Klee. Electromechanical properties of thin ferroelectric $Pb(Zr_{0.53}Ti_{0.47})O_3$-layers. *Ferroelectrics*, 163(1):77–88, January 1995.

[60] L. J. Nelson, C. R. Bowen, R. Stevens, M. Cain, and M. Stewart. Modelling and measurement of piezoelectric fibres and interdigitated electrodes for the optimisation of piezofibre composites. In D. C. Lagoudas, editor, *SPIE Smart Structures and Materials - Active Materials: Behavior and Mechanics*, volume 5053, pages 556–567, San Diego, CA, March 2003.

[61] A. A. Bent. *Active Fiber Composite for Structural Actuation*. PhD thesis, MIT-Department of Aeronautics and Astronautics, Cambridge, MA, January 1997.

[62] D. Berlincourt and H. H. A. Krueger. Properties of piezoelectricity ceramics. Tp-226, Morgan Electro Ceramics.

[63] M. Wegener and S.. Bauer. Microstorms in cellular polymers: A route to soft piezoelectric transducer materials with engineered macrosopic dipoles. *ChemPhysChem*, 6(6):1014–1025, June 2005.

[64] V. Geiser. Flexible electrets from particle-stabilized foams. Master's thesis, ETH Zurich, 2006.

[65] J. Heiber, A. Belloli, F. Clemens, and P. Ermanni. Ferroelectric characterization of single PZT fibers. *Journal of Intelligent Material Systems and Structures*, 20(4):379–385, March 2009.

[66] U. Selvaraj, A. V. Prasadarao, S. Komarneni, K. Brooks, and S. Kurtzet. Sol-gel processing of $PbTiO_3$ and $Pb(Zr_{0.52}Ti_{0.48})O_3$. *Journal of Materials Research*, 7(4):992–996, April 1992.

[67] Y. Kobayashi, T. Y. Um, J. Qiu, J. Tani, and H. Takahashi. Fabrication of piezoelectric ceramic fibers by extrusion of PZT powder and PZT sol mixture. In *SPIE Smart Structures and Materials - Active Materials: Behavior and Mechanics*, volume 4333, pages 314–321, Newport Beach, March 2001.

[68] Y. Wang, S. Serrano, and J. J. Santiago-Aviles. Electrostatic synthesis and characterization of $Pb(Zr_xTi_{1-x})O_3$ micro/nano-fibers. In *Materials Research Society Symposium Proceedings*, volume 702, pages 359–364, 2001.

[69] J.-W. Kim and J. G. Heinrich. Influence of processing parameters on microstructure and ferroelectric properties of PZT-coated SiC fibers. *Journal of the European Ceramic Society*, 25(9):1637–1645, June 2005.

[70] J. D. French, G. E. Weitz, J. E. Luke, R. B. Cass, B. Jadidian, P. Bhargava, and A. Safari. Production of continuous piezoelectric ceramic fibers for smart materials and active control devices. In J. M. Sater, editor, *SPIE Smart Structures and Materials - Industrial and Commercial Applications of Smart Structures Technologies*, volume 3044, pages 406–412, May 1997.

[71] D. Vorbach, F. Niemz, G. Helke, L. Seffner, and A. Schönecker. Mit dem Lyocell-Verfahren hergestellte piezokeramische Fasern - Eigenschaften und Einsatzmöglichkeiten. In *Adaptronic Kongress*, Berlin, April 2001.

[72] T. Gesang, H. Knaebel, U. Maurieschat, A. Hartwig, T. Riesenbeck, H. Schaefer, A. Battermann, J. Perl, A. Gau, A. Schoenecker, and L. Seffner. Comparison of adaptronic microsystems based on piezoelectric fibers for general use or for the utilization in prepreg FRP. In A.-M. R. McGorwan, editor, *SPIE Smart Structures and Materials:*

Industrial and Commercial Applications of Smart Structures Technologies, volume 4698, pages 325–332, San Diego, March 2002.

[73] H.-J. Gesemann and R. Gesemann. Analysenverfahren zur Ermittlung des PbO-Gehaltes in PZT-Keramiken. *Hermsdorfer Technische Mitteilungen*, 18(50):1600–1601, 1978.

[74] J. D. French and R. B. Cass. Developing innovative ceramic fibers. *American Ceramic Society Bulletin*, 77(5):61–65, May 1998.

[75] M. Wegmann, J. Heiber, F. Clemens, T. Graule, D. Hülsenberg, and K. Schuster. Forming noncircular cross-section SiO_2 glass fibers. *Glass Science and Technology*, 78(2):69–75, 2005.

[76] A. C. Dent, L. J. Nelson, C. R. Bowen, R. Stevens, M. Cain, and M. Stewart. Characterisation and properties of fine scale PZT fibres. *Journal of the European Ceramic Society*, 25(12):2387–2391, May-June 2005.

[77] A. Belloli, J. Heiber, F. Clemens, and P. Ermanni. Novel characterization procedure for single piezoelectric fibers. *Journal of Intelligent Material Systems and Structures*, 20(3):355–363, February 2008.

[78] J. Heiber, F. Clemens, U. Helbig, A. de Meuron, C. Soltmann, T. Graule, and D. Hülsenberg. Properties of $Pb(Zr,Ti)O_3$ fibres with a radial gradient structure. *Acta Materialia*, 55(19):6499–6506, November 2007.

[79] J. Heiber, F. Clemens, T. Graule, and D. Hülsenberg. Thermoplastic extrusion to highly-loaded thin green fibers containing $Pb(Zr,Ti)O_3$. *Advanced Engineering Materials*, 7(5):404–408, May 2005.

[80] M. Hammer and M. J. Hoffmann. Sintering model for mixed-oxide-derived lead zirconate titanate ceramics. *Journal of the American Ceramic Society*, 81(12):3277–3284, December 1998.

[81] R. E. Chinn. *Preparation and Analysis of Ceramic Microstructures*. Materials Park: ASM International, 2002.

[82] S. Cheng, I. K. Lloyd, and M. Kahn. Modification of surface texture by grinding and polishing lead zirconate titanate ceramics. *Journal of the American Ceramic Society*, 75(8):2293–2296, August 1992.

[83] H. Krischner. *Einführung in die Röntgenfeinstrukturanalyse*. Vieweg, Braunschweig, 1990.

[84] J. C. Fernandes, D. A. Hall, M. R. Cockburn, and G. N. Greaves. Phase coexistence in PZT ceramic powders. *Nuclear Instruments and Methods in Physics Research Section B: Beam Interactions with Materials and Atoms*, 97(1-4):137–141, May 1995.

[85] P. Loebmann, U. Lange, W. Glaubitt, F. Hutter, and D. Sporn. Powders, fibers, thin films and aerogels: Sol-gel-derived piezoelectric materials. *Key Engineering Materials*, 224-226:613–618, 2002.

[86] G. H. Haertling. Hot-pressed lead zirconate-titanate ceramics containing bismuth. *The American Ceramic Society Bulletin*, 43(12):875–879, December 1964.

[87] B. Jaffe, R. S. Roth, and S. Marzullo. Properties of piezoelectric ceramics in the solid solution series lead titanate - lead zirconate - lead oxide: Tin oxide and lead titanate - lead hafnate. *Journal of Research of the National Bureau of Standards*, 55(5):239–254, November 1955.

[88] G. H. Haertling and W. J. Zimmer. An analysis of hot-pressing parameters for lead zirconate - lead titanate ceramics containing two atom percent bismuth. *American Ceramic Society Bulletin*, 45(12):1084–1089, December 1966.

[89] A. A. Bent and N. W. Hagood. Development of piezoelectric fiber composites for structural actuation. In 34^{th} *AIAA/ASME/ASCE/AHS Structures, Structural Dynamics and Materials Conference*, La Jolla, CA, April 1993. AIAA Paper no. 93-1717.

[90] G. A. Rossetti, A. E. Pizzochero, and A. A. Bent. Recent advances in active fiber composites technology. In 12^{th} *IEEE International Symposium on the Application of Ferroelectrics*, volume 2, pages 753–757, 2001.

[91] B. Castelli. Modeling and characterization of active fiber composites. Master's thesis, ETH Zurich, July 2003.

[92] IEEE standard on piezoelectricity. Technical Report ANSI/IEEE Std 176-1987, American National Standards Institute, September 1987.

[93] X. Kornmann, C. Huber, and H.-R. Elsener. Piezoelectric ceramic fibers for active fiber composites: a comparative study. In A. M. Baz, editor, *SPIE Smart Structures and Materials - Smart Structures and Integrated Systems*, volume 5056, pages 330–337, San Diego, CA, March 2003.

[94] N. Pini, A. Belloli, H. R. Schubach, E. Hack, M. Barbezat, and P. Ermanni. Characterisation of active fibre composites with polypyrrole finger electrodes. In 17^{th} *International Conference on Adaptive Structures and Technologies*, Taipei, Taiwan, October 2006.

[95] N. Goudemand. *3D-3C Speckle Interferometry: Optical Device for Measuring Complex Structures*. PhD thesis, ETH Zurich. Diss. ETH No. 15961, 2005.

[96] N. Pini. *Development and Processing of Novel Active Fibre Composites*. PhD thesis, ETH Zurich. Diss. ETH No. 16904, October 2006.

[97] P. J. Bentley. *Evolutionary Design by Computers*. Morgan Kaufmann Publishers, San Francisco, CA, 1999.

[98] M. Wintermantel. *Design-Encoding for Evolutionary Algorithms In the Field of Structural Optimization*. PhD thesis, ETH Zurich. Diss. ETH No. 15323, 2004.

[99] O. König. *Evolutionary Design Optimization: Tools and Applications*. PhD thesis, ETH Zurich. Diss. ETH No. 15486, 2004.

[100] P. Calvert. Inkjet printing for materials and devices. *Chemistry of Materials*, 13(10):3299–3305, October 2001.

[101] B.-J. de Gans, P. C. Duineveld, and U. S. Schubert. Inkjet printing of polymers: State of the art and future developments. *Advanced Materials*, 16(3):203–213, February 2004.

[102] J. Z. Wang, Z. H. Zheng, H. W. Li, W. T. S. Huck, and H. Sirringhaus. Dewetting of conducting polymer inkjet droplets on patterned surfaces. *Nature Materials*, 3(3):171–176, March 2004.

[103] H. Sirringhaus, T. Kawase, R. H. Friend, T. Shimoda, M. Inbasekaran, W. Wu, and E. P. Woo. High-resolution inkjet printing of all-polymer transistor circuits. *Science*, 290(5499):2123–2126, December 5499.

[104] C. W. Sele, T. von Werne, R. H. Friend, and H. Sirringhaus. Lithography-free, self-aligned inkjet printing with sub-hundred-nanometer resolution. *Advanced Materials*, 17(8):997–1001, April 2005.

[105] S. B. Fuller, E. J. Wilhelm, and J. M. Jacobson. Ink-jet printed nanoparticle microelectromechanical systems. *Journal of Microelectromechanical Systems*, 11(1):54–60, February 2002.

[106] N. R. Bieri, J. Chung, S. E. Haferl, D. Poulikakos, and C. P. Grigoropoulos. Microstructuring ny printing and laser curing of nanoparticle solutions. *Applied Physics Letters*, 82(20):3529–3531, May 2003.

[107] G. G. Rozenberg, E. Bresler, S. P. Speakman, C. Jeynes, and J. H. G. Steinke. Patterned low temperature copper-rich deposits using inkjet printing. *Applied Physics Letters*, 81(27):5249–5251, December 2002.

[108] I. McDonald. *Electroplating Engineering Handbook*, chapter 14, pages 438–460. Van Nostrand Reinhold Company, New York, 1984.

[109] P. Shah, Y. Kevrekidis, and J. Benziger. Ink-jet printing of catalyst patterns for electroless metal deposition. *Langmuir*, 15(4):1584–1587, February 1999.

[110] S. Magdassi, Bassa A., Y. Vinetsky, and A. Kamyshny. Silver nanoparticles as pigments for water-based ink-jet inks. *Chemistry of Materials*, 15(11):2208–2217, April 2003.

[111] H. Tabei, S. Nara, and K. Matsuyama. Method for forming a printed circuit by photolysis of silver salt of organic acid. *Journal of the Electrochemical Society*, 121(1):67–69, January 1974.

[112] M. J. Ware. An investigation of platinum and palladium printing. *The Journal of Photographic Science*, 34(5-6):13–25, September-December 1986.

[113] L. I. Elding. Palladium(ii) halide complexes. i. stabilities and spectra of palladium(ii) chloro and bromo aqua complexes. *Inorganica Chimica Acta*, 6(4):647–651, December 1972.

[114] Z. Wang, A. Furuya, K. Yasuda, H. Ikeda, T. Baba, M. Hagiwara, S. Toki, S. Shingubara, H. Kubota, and T. Ohmi. Adhesion improvement of electroless copper to a polyimide film substrate by combining surface microroughening and imide ring cleavage. *Journal of Adhesion Science and Technology*, 16(8):1027–1040, July 2002.

[115] W. Yu and T.-M. Ko. Surface characterizations of potassium-hydroxide-modified upilex-s® polyimide at an elevated temperature. *European Polymer Journal*, 37(9):1791–1799, September 2001.

[116] I. Ohno, O. Wakabayashi, and S. Haruyama. Anodic oxidation of reductans in electroless plating. *Journal of the Electrochemical Society*, 132(10):2323–2330, October 1985.

[117] R. B. Williams, B. W. Grimsley, D. J. Inman, and W. K. Wilkie. Manufacturing and mechanics-based characterization of macro fiber composite actuators. In J. Shaw and M. Frecker, editors, *ASME International Mechanical Engineering Congress & Exposition (IMECE)*, volume 67, pages 79–89, New Orleans (LA), November 2002. ASME.

[118] H. Lammer. Use of adaptive materials and the effects achievable in sporting goods like the Is18 and the ski Ic300 by Head Sport AG. In *Adaptronics Congress*, Wolfsburg, April 2003.

[119] E. Bianchini, R. L. Spangler, and T. Pandell. Use of piezoelectric dampers for improving the feel of golf clubs. In N. M. Wereley, editor, *SPIE Smart Structures and Materials - Smart Structures and Integrated Systems*, volume 3668, pages 824–834, Newport Beach, CA, March 1999.

[120] W. Zirngibl. Influence of special material on the acute/chronic epicondylitis radials (tennis elbow) with the Head Intelligence System. In 4^{th} *Congress of Prophylactic Orthopedics*, Munich, April 2003.

[121] Vibration X, http://vibration-x.com/.

[122] E. F. Crawley and J. De Luis. Use of piezoelectric actuators as elements of intelligent structures. *AIAA Journal*, 25(10):1373–1385, October 1987.

[123] S. Mall and J. M. Coleman. Monotonic and fatigue loading behavior of quasi-isotropic graphite/epoxy laminate embedded with piezoelectric sensor. *Smart Materials and Structures*, 7(6):822–832, December 1998.

[124] C. A. Paget and K. Levin. Structural integrity of composites with embedded piezoelectric ceramic transducers. In N. Wereley, editor, *SPIE Smart Structures and Materials - Smart Structures and Integrated Systems*, volume 3668, pages 306–313, Newport Beach, CA, March 1999.

[125] D. A. Singh and A. J. Vizzini. Structural integrity of composite laminates with interlaced actuators. *Smart Materials and Structures*, 3(1):71–79, March 1994.

[126] D. R. Shukla and A. J. Vizzini. Interlacing for improved performance of laminates with embedded devices. *Smart Materials and Structures*, 5(2):225–229, April 1996.

[127] J. P. Hansen and A. J. Vizzini. Fatigue response of a host structure with interlaced embedded devices. *Journal of Intelligent Material Systems and Structures*, 11(11):902–909, November 2000.

[128] I. M. Daniel and O. Ishai. *Engineering Mechanics of Composite Materials*. Oxford University Press, New York, 2^{nd} edition, 2005.

[129] P. D. Soden, M. J. Hinton, and A. S. Kaddour. A comparison of the predictive capabilities of current failure theories for composite laminates. *Composites Science and Technology*, 58(7):1225–1254, July 1998.

[130] M. J. Hinton, A. S. Kaddour, and P. D. Soden. A comparison of the predictive capabilities of current failure theories for composite laminates, judged against experimental evidence. *Composites Science and Technology*, 62(12-13):1725–1797, September-October 2002.

[131] S. W. Tsai and E. M. Wu. A general theory of strength for anisotropic materials. *Journal of Composite Materials*, 5(1):58–80, January 1971.

[132] A. Kuraishi, S. W. Tsai, and K. K. S. Liu. A progressive quadratic failure criterion, part B. *Composites Science and Technology*, 62(12-13):1683–1695, September-October 2002.

[133] A. Puck. *Festigkeitsanalyse von Faser-Matrix-Laminaten*. Carl Hanser, Wien, 1996.

[134] M. Melnykowycz, X. Kornmann, C. Huber, M. Barbezat, and A. J. Brunner. Performance of integrated active fiber composites in

fiber reinforced epoxy laminates. *Smart Materials and Structures*, 15(1):204–212, February 2006.

[135] R. Zemčík, R. Rolfes, M. Rose, and J. Tessmer. High-performance 4-node shell element with piezoelectric coupling. In C. A. Mota Soares *et al.*, editor, *II ECCOMAS Thematic Conference on Smart Structures and Materials*, Lisbon, July 2005.

[136] S. Mall. Integrity of graphite/epoxy laminate embedded with piezoelectric sensor/actuator under monotonic and fatigue loads. *Smart Materials and Structures*, 11(4):527–533, August 2002.

[137] V. K. Wickramasinghe and N. W. Hagood. Material characterization of active fiber composites for integral twist-actuated rotor blade application. *Smart Materials and Structures*, 13(5):1155–1165, October 2004.

[138] A. Preumont. *Vibration Control of Active Structures - An Introduction*. Kluwer Academic Publishers, Dordrecht, The Netherlands, 1997.

[139] S. A. Elliott and P. J. Nelson. Active noise control. *IEEE Signal Processing Magazine*, 10(4):12–35, 1993.

[140] C. R. Fuller, S. J. Elliott, and P. A. Nelson. *Active Control of Vibration*. Academic Press Limited, 24-28 Oval Road, London, 1996.

[141] C. C. Sung and C. Y. Chiu. Control of sound transmission through thin plate. *Journal of Sound and Vibration*, 218(4):605–618, 1998.

[142] N. W. Hagood and A. von Flotow. Damping of structural vibrations with piezoelectric materials and passive electrical networks. *Journal of Sound and Vibration*, 146(2):243–268, April 1991.

[143] M. S. Tsai and K. W. Wang. On the structural damping characteristics of active piezoelectric actuators with passive shunt. *Journal of Sound and Vibration*, 221(1):1–22, March 1999.

[144] J. Tang and K. W. Wang. Active-passive hybrid piezoelectric networks for vibration control: Comparisons and improvement. *Smart Materials and Structures*, 10(4):794–806, August 2001.

[145] S. O. R. Moheimani, A. J. Fleming, and S. Behrens. On the feedback structure of wideband piezoelectric shunt damping systems. *Smart Materials and Structures*, 12(1):49–56, February 2003.

[146] G. A. Lesieutre. Vibration damping and control using shunted piezoelectric materials. *The Shock and Vibration Digest*, 30(3):187–195, May 1998.

[147] C. L. Davis and G. A. Lesieutre. An actively tuned solid-state vibration absorber using capacitive shunting of piezoelectric stiffness. *Journal of Sound and Vibration*, 232(3):601–617, May 2000.

[148] R. Rusovici, J. J. Dosch, and G. A. Lesieutre. Design of a single-crystal piezoceramic vibration absorber. *Journal of Intelligent Material Systems and Structures*, 13(11):705–712, November 2002.

[149] S.-Y. Wu. Method for multiple mode shunt damping of structural vibration using a single PZT transducer. In L. P. Davis, editor, *SPIE Smart Structures and Materials - Passive Damping and Isolation*, volume 3327, pages 159–168, San Diego, CA, March 1998.

[150] A. J. Fleming and S. O. R. Moheimani. Synthesis of optimal piezoelectric shunt impedances for structural vibration control. In K. W. Wang, editor, *SPIE Smart Structures and Materials - Damping and Isolation*, volume 5386, pages 516–527, San Diego, CA, March 2004.

[151] D. J. Warkentin and N. W. Hagood. Nonlinear piezoelectric shunting for structural damping. In M. E. Regelbrugge, editor, *SPIE Smart Structures and Materials - Smart Structures and Integrated Systems*, volume 3041, pages 747–757, San Diego, CA, June 1997. SPIE.

[152] L. R. Corr and W. W. Clark. Energy dissipation analysis of piezoceramic semi-active vibration control. *Journal of Intelligent Material Systems and Structures*, 12(11):729–736, November 2001.

[153] D. Niederberger, M. Morari, and S. Pietrzko. A new control approach for switching shunt damping. In K. W. Wang, editor, *SPIE Smart Structures and Materials - Damping and Isolation*, volume 5386, pages 426–437, San Diego, CA, March 2004.

[154] C. J. Cross and S. Fleeter. Shunted piezoelectrics for passive control of turbomachine blading flow-induced vibrations. *Smart Materials and Structures*, 11(2):239–248, April 2002.

[155] E. Bianchini, R. Spangler, and C. Andrus. The use of piezoelectric devices to control snowboard vibrations. Technical report, Active Control eXperts, Inc., and K2 Corporation, 1998.

[156] M. Ahmadian and K. M. Jeric. Effect of shunted piezoelectric materials on increasing sound transmission loss. In D. J. Inman, editor, *SPIE Smart Structures and Materials - Damping and Isolation*, volume 4331, pages 273–280, Newport Beach, CA, March 2001.

[157] M. Ahmadian, K. M. Jeric, and D. J. Inman. An experimental analysis of the benefits of shunted piezoceramics for damped and undamped structures. In D. J. Inman, editor, *SPIE Smart Structures and Materials - Damping and Isolation*, volume 4331, pages 281–293, Newport Beach, CA, March 2001.

[158] T. W. Nye, R. A. Ghaby, G. R. Dvorsky, and J. K. Honig. The use of smart structures for spacecraft vibration suppression. 44th IAF International Congress, Graz, Austria, August 1993.

[159] A. Belloli, B. Castelli, X. Kornmann, C. Huber, and P. Ermanni. Modeling and characterization of active fiber composites. In A. B. Flatau, editor, *SPIE Smart Structures and Materials - Smart Structures and Integrated Systems*, volume 5390, pages 78–88, San Diego, CA, March 2004.

[160] D. Niederberger, M. Morari, and S. Pietrzko. Adaptive resonant shunted piezoelectric devices for vibration suppression. In A. M. Baz, editor, *SPIE Smart Structures and Materials - Smart Structures*

and Integrated Systems, volume 5056, pages 213–224, San Diego, CA, March 2003.

[161] H. Hanselka. Adaptronik und Fragen zur Systemzuverlässigkeit. *ATP, Automatisierungstechnische Praxis*, 44(2):40–49, February 2002.

[162] A. Belloli, D. Niederberger, X. Kornmann, P. Ermanni, M. Morari, and S. Pietrzko. Vibration control via shunted embedded piezoelectric fibers. In K. W. Wang, editor, *SPIE Smart Structures and Materials - Damping and Isolation*, volume 5386, pages 528–537, San Diego, CA, March 2004.

[163] A. Antoniou. Realisation of gyrators using operational amplifiers and their use in RC-active network synthesis. *Proc. IEE*, 116(11):1838–1850, 1969.

[164] W.-K. Chen. *Passive and Active Filters*. John Wiley and Sons, Inc., New York, 1986.

[165] H. Sato, Y. Shimojo, and T. Sekiya. Fabrication and vibration suppression behavior of metal core-piezoelectric fibers in CFRP composite. In *SPIE's International Symposium on Photonics Fabrication Europe, Transducing Materials and Devices*, volume 4946, Brugge, Belgium, October 2002.

[166] A. J. Fleming, S. Behrens, and S. O. R. Moheimani. Synthetic impedance for implementation of piezoelectric shunt-damping circuits. *IEE Electronics Letters*, 36(18):1525–1526, August 2000.

[167] M. C. Reaves and L. G. Horta. Test cases for modeling and validation of structures with piezoelectric actuators. Technical Report AIAA Report 2001-1466, NASA Langley Research Center, Hampton, VA, 2001.

[168] F. Côté, P. Masson, and N. Mrad. Dynamic and static assessment of piezoelectric embedded composites. In L. P. Porter, editor, *SPIE Smart Structures and Materials - Smart Structures and Integrated*

Systems, volume 4701, pages 316–325, San Diego, CA, March 2002.

[169] Morgan-Matroc. *Piezoelectric Ceramics Data Book for Designers*. Morgan Matroc Ltd., Thornhill, Southampton, Hampshire SO19 7TG, UK, 1987.

[170] R. A. Morgan and K. W. Wang. A multi-frequency piezoelectric vibration absorber for variable frequency harmonic excitations. In D. J. Inman, editor, *SPIE Smart Structures and Materials - Damping and Isolation*, volume 4331, pages 130–140, Newport Beach, CA, March 2001.

[171] A. J. Fleming and S. O. R. Moheimani. Adaptive piezoelectric shunt damping. In V. S. Rao, editor, *SPIE Smart Structures and Materials - Modeling, Signal Processing, and Control*, volume 4693, pages 556–567, San Diego, CA, March 2002.

[172] X. Kornmann and C. Huber. Microstructure and mechanical properties of PZT fibres. *Journal of the European Ceramic Society*, 24(7):1987–1991, June 2004.

[173] S. L. Padula and R. K. Kincaid. Optimization strategies for sensor and actuator placement. Technical Report NASA/TM-1999-209126, April 1999.

[174] M. I. Frecker. Recent advances in optimization of smart structures and actuators. *Journal of Intelligent Material Systems and Structures*, 14(4-5):207–216, April/May 2003.

[175] J. J. Hollkamp. Multimodal passive vibration suppression with piezoelectric materials and resonant shunts. *Journal of Intelligent Material Systems and Structures*, 5(1):49–57, January 1994.

[176] Y. K. Kang, H. C. Park, W. Hwang, and K. S. Han. Optimum placement of piezoelectric sensor/actuator for vibration control of laminated beams. *AIAA Journal*, 34(9):1921–1926, September 1996.

[177] Y. Li, J. Onoda, and K. Minesugi. Simultaneous optimization of piezoelectric actuator placement and feedback for vibration suppression. *Acta Astronautica*, 50(6):335–341, March 2002.

[178] Y. K. Kang, H. C. Park, and B. Agrawal. Optimization of piezoceramic sensor/actuator placement for vibration control of laminated plates. *AIAA Journal*, 36(9):1763–1765, September 1998.

[179] F. Seeger and U. Gabbert. Optimal placement of distributed actuators for a controlled smart elastic plate. *Proceedings in Applied Mathematics and Mechanics*, 2(1):262–263, March 2003.

[180] D. Sun, L. Tong, and D. Wang. Vibration control of plates using discretely distributed piezoelectric quasi-modal actuators/sensors. *AIAA Journal*, 39(9):1766–1772, September 2001.

[181] D. Sun and L. Tong. Modal control of smart shells by optimized discretely distributed piezoelectric transducers. *International Journal of Solids and Structures*, 38(18):3281–3299, May 2001.

[182] T.-W. Kim and J.-H. Kim. Optimal distribution of an active layer for transient vibration control of a flexible plate. *Smart Materials and Structures*, 14(5):904–916, October 2005.

[183] T.-W. Kim and J.-H. Kim. Eigensensitivity based optimal distribution of a viscoelastic damping layer for a flexible beam. *Journal of Sound and Vibration*, 273(1-2):201–218, May 2004.

[184] M. Rose. Modal based correction methods for the placement of piezoceramic modules. In *2005 ASME International Mechanical Engineering Congress and Exposition*, Orlando (FL), November 2005.

[185] D. Halim and S. O. R. Moheimani. An optimization approach to optimal placement of collocated piezoelectric actuators and sensors on a thin plate. *Mechatronics*, 13(1):27–47, February 2003.

[186] P. Hajela. Genetic search - an approach to the nonconvex optimization problem. *AIAA Journal*, 28(7):1205–1210, July 1990.

[187] S. S. Rao, T.-S. Pan, and V. B. Venkayya. Optimal placement of actuators in actively controlled structures using genetic algorithms. *AIAA Journal*, 29(6):942–943, June 1991.

[188] Y. J. Yan and L. H. Yam. Optimal design of number and locations of actuators in active vibration control of a space truss. *Smart Materials and Structures*, 11(4):496–503, August 2002.

[189] J. A. Bishop and A. G. Striz. On using genetic algorithms for optimum damper placement in space trusses. *Structural and Multidisciplinary Optimization*, 28(2-3):136–145, September 2004.

[190] A. Richardson and M. M. Abdullah. Sensor/actuators placement on civil structures using a real coded genetic algorithm. In S.-C. Liu and Pines D. J., editors, *SPIE Smart Structures and Materials - Smart Systems for Bridges, Structures, and Highways*, volume 4696, pages 244–255, San Diego (CA), March 2002.

[191] P. Gaudenzi, E. Fantini, V. K. Koumousis, and C. J. Gantes. Genetic algorithm optimization for the active control of a beam by means of PZT actuators. *Journal of Intelligent Material Systems and Structures*, 9(4):291–300, April 1998.

[192] H. Zhang, B. Lennox, P. R. Goulding, and A. Y. T. Leung. A float-encoded genetic algorithm technique for integrated optimization of piezoelectric actuator and sensor placement and feedback gains. *Smart Materials and Structures*, 9(4):552–557, August 2000.

[193] Y. Yang, Z. Jin, and C. K. Soh. Integrated optimal design of vibration control system for smart beams using genetic algorithms. *Journal of Sound and Vibration*, 282(3-5):1293–1307, April 2005.

[194] Y. Yang, Z. Jin, and C. K. Soh. Integrated optimization of control system for smart cylindrical shells using modified GA. *Journal of Aerospace Engineering*, 19(2):68–79, April 2006.

[195] J.-H. Han and I. Lee. Optimal placement of piezoelectric sensors and actuators for vibration control of a composite plate using genetic algorithms. *Smart Materials and Structures*, 8(2):257–267, April 1999.

[196] A. M. Sadri, J. R. Wright, and R. J. Wynne. Modelling and optimal placement of piezoelectric actuators in isotropic plates using genetic algorithms. *Smart Materials and Structures*, 8(4):490–498, August 1999.

[197] S. T. Quek, S. Y. Wang, and K. K. Ang. Vibration control of composite plates via optimal placement of piezoelectric patches. *Journal of Intelligent Material Systems and Structures*, 14(4-5):229–245, April/May 2003.

[198] F. Peng, A . Ng, and Y.-R. Hu. Actuator placement optimization and adaptive vibration control of plate smart structures. *Journal of Intelligent Material Systems and Structures*, 16(3):263–271, March 2005.

[199] S. Y. Wang, K. Tai, and S. T. Quek. Topology optimization of piezoelectric sensors/actuators for torsional vibration control of composite plates. *Smart Materials and Structures*, 15(2):253–269, April 2006.

[200] A. K. Jha and D. J. Inman. Optimal sizes and placements of piezoelectric actuators and sensors for an inflated torus. *Journal of Intelligent Material Systems and Structures*, 14(9):563–576, September 2003.

[201] S. Yan and M. N. Ghasemi-Nejhad. Modeling and genetic algorithms based piezoelectric actuator configuration optimization of an adaptive circular composite plate. In R. C. Smith, editor, *SPIE Smart Structures and Materials - Modeling, Signal Processing, and Control*, volume 5383, pages 255–264, San Diego, CA, March 2004.

[202] C. J. Damaren. Optimal location of collocated piezo-actuator/sensor combinations in spacecraft box structures. *Smart Structures and Materials*, 12(3):494–499, June 2003.

[203] A. Belloli, O. Thomaschewski, and P. Ermanni. Optimum placement of piezoelectric ceramic modules for vibration suppression of highly constrained structures. In K.-W. Wang and W. W. Clark, editors, *2005 ASME International Design Engineering Technical Conferences & Computers and Information in Engineering - 20th Biennial Conference on Mechanical Vibration and Noise*, Long Beach, CA, September 2005.

[204] D. Niederberger and M. Morari. An autonomous shunt circuit for vibration damping. *Smart Material ans Structures*, 15 (2006) 359–364(2):359–364, April 2006.

[205] J. L. Fanson and T. K. Caughey. Positive position feedback for large space structures. *AIAA Journal*, 28(4):717–724, April 1990.

[206] T. Lambrecht. Integration of piezoelectric ceramic elements and passive shunt networks for vibration suppression of lightweight structures. Master's thesis, ETH Zurich, August 2005.

[207] P. Wierach, H.-P. Monner, A. Schönecker, and J. K. Dürr. Application specific design of adaptive structures with piezoceramic patch actuators. In A.-M. McGowan, editor, *SPIE Smart Structures and Materials - Industrial and Commercial Applications of Smart Structures Technologies*, volume 4698, pages 333–341, San Diego, CA, March 2002. SPIE.

Own Publications

[1] M. M. Melnykowycz, A. Belloli, R. Paradies, and P. Ermanni. Integrity characterization of smart composite laminates with AFC inclusions. *Composites Science and Technology*, submitted, 2009.

[2] J. Heiber, A. Belloli, F. Clemens, and P. Ermanni. Ferroelectric characterization of single PZT fibers. *Journal of Intelligent Material Systems and Structures*, 20(4):379–386, March 2009.

[3] A. Belloli, J. Heiber, F. Clemens, and P. Ermanni. Novel characterization procedure for single piezoelectric fibers. *Journal of Intelligent Material Systems and Structures*, 20(3):355–363, February 2009.

[4] M. M. Melnykowycz, A. Belloli, R. Paradies, and P. Ermanni. Investigation of Smart Composite Laminates with Embedded PZT-Based Modules. *In SEICO 08 - SAMPE EUROPE International Conference and Forum*, pages 526–531, Paris, April 2008.

[5] A. Belloli, and P. Ermanni. Optimum Placement of Piezoelectric Ceramic Modules for Vibration Suppression of Highly Constrained Structures. *Smart Materials and Structures*, 16(5):1662–1671, October 2007

[6] A. Belloli, J. Heiber, F. Clemens, and P. Ermanni. Novel Characterization Procedure for Single Piezoelectric Fibers. 18th *International Conference on Adaptive Structures and Technologies*, Ottawa, October 2007.

[7] A. Belloli, D. Niederberger, S. Pietrzko, M. Morari, and P. Ermanni. Structural vibration control via *R-L* shunted active fiber composites. *Journal of Intelligent Material Systems and Structures*, 18(3):275–287, March 2007.

[8] S. Busato, A. Belloli, and P. Ermanni. Inkjet printing of palladium catalyst patterns on polyimide film for electroless copper plating. *Sensors and Actuators B*, 123(1):840–846, January 2007.

[9] A. Belloli, and P. Ermanni. Optimum Placement of Piezoelectric Ceramic Modules for Vibration Suppression of Highly Constrained Structures. 17th *International Conference on Adaptive Structures and Technologies*, Taipei, October 2006.

[10] N. Pini, A. Belloli, H. R. Schubach, E. Hack, M. Barbezat, and P. Ermanni. Characterisation of Active Fibre Composites with polypyrrole finger electrodes. 17th *International Conference on Adaptive Structures and Technologies*, Taipei, October 2006.

[11] M. M. Melnykowycz, A. Belloli, P. Ermanni, and M. Barbezat. Integration and Reliability of Active Fiber Composite (AFC) Sensors / Actuators in Carbon/Epoxy Laminates. In W. D. Armstrong, editor, *SPIE Smart Structures and Materials - Active Materials: Behavior and Mechanics*, volume 6170, San Diego, CA, March 2006.

[12] A. Belloli, O. Thomaschewski, and P. Ermanni. Optimum placement of piezoelectric ceramic modules for vibration suppression of highly constrained structures. In K.-W. Wang and W. W. Clark, editors, *2005 ASME International Design Engineering Technical Conferences & Computers and Information in Engineering - 20th Biennial Conference on Mechanical Vibration and Noise*, Long Beach, CA, September 2005.

[13] A. Belloli, D. Niederberger, S. Pietrzko, M. Morari, and P. Ermanni. Structural vibration control via *R-L* shunted active fiber composites. 15^{th} *International Conference on Adaptive Structures and Technologies*, Bar Harbor, October 2004.

[14] A. Belloli, B. Castelli, X. Kornmann, C. Huber, and P. Ermanni. Modeling and characterization of active fiber composites. In A. B. Flatau, editor, *SPIE Smart Structures and Materials - Smart Structures and Integrated Systems*, volume 5390, pages 78–88, San Diego, CA, March 2004.

[15] A. Belloli, D. Niederberger, X. Kornmann, P. Ermanni, M. Morari, and S. Pietrzko. Vibration control via shunted embedded piezoelectric fibers. In K. W. Wang, editor, *SPIE Smart Structures and Materials - Damping and Isolation*, volume 5386, pages 528–537, San Diego, CA, March 2004.

Curriculum Vitae

Name:	Alberto Belloli
Date of Birth:	November 29th, 1976
Nationality:	Swiss
Address:	CH - 6557 Cama
Email:	a.belloli@rowa-ag.ch

Education

Diploma HSG in "KMU Management":	09.2008
Continuing Education in "KMU Management":	04.2007 - 07.2008
University:	HSG St. Gallen, Switzerland
Visiting Scholar at DLR Braunschweig:	04.2004 - 10.2004
Research Center:	DLR Braunschweig, Germany
PhD Study:	04.2002 - 09.2006
University:	ETH Zurich, Switzerland

Diploma in Mechanical Engineering ETH:	11.2001
Diploma Thesis (CCM - University of Delaware):	04.2001 - 10.2001
Study in Mechanical Engineering:	10.1996 - 03.2001
University:	ETH Zurich, Switzerland
High School, Typ C - Scientific:	09.1992 - 06.1996
School:	Liceo Cantonale Bellinzona, Switzerland

Professional Experience

CEO:	since 07.2009
Project Leader:	since 09.2008
Company:	Rowa Tunnelling Logistics AG Wangen SZ, Switzerland
Head of F&E:	since 04.2008
Company:	Belloli SA Grono GR, Switzerland
Project Leader:	10.2006 - 03.2008
Research Institute:	Empa Duebendorf, Switzerland
Research assistant:	02.2002 - 09.2006
University:	ETH Zurich, Switzerland
Internship:	07.2000 - 10.2000
Companies:	Rieter Maschinenfabrik AG Winterthur ZH, Switzerland / Continental Eagle Co. Prattville AL, USA
Undergraduate assistant:	1999 - 2000
University:	ETH Zurich, Switzerland